

SPECTROSCOPY OF TYPE Ia SUPERNOVAE BY THE CARNEGIE SUPERNOVA PROJECT*

GASTÓN FOLATELLI¹, NIDIA MORRELL², MARK M. PHILLIPS², ERIC HSIAO², ABDO CAMPILLAY², CARLOS CONTRERAS², SERGIO CASTELLÓN², MARIO HAMUY³, WOJTEK KRZEMINSKI⁴, MIGUEL ROTH², MAXIMILIAN STRITZINGER⁵, CHRISTOPHER R. BURNS⁶, WENDY L. FREEDMAN⁶, BARRY F. MADORE^{6,7}, DAVID MURPHY⁶, S. E. PERSSON⁶, JOSÉ L. PRIETO⁸, NICHOLAS B. SUNTZEFF⁹, KEVIN KRISCIUNAS⁹, JOSEPH P. ANDERSON³, FRANCISCO FÖRSTER³, JOSÉ MAZA³, GIULIANO PIGNATA¹⁰, P. ANDREA ROJAS¹¹, LUIS BOLDT¹², FRANCISCO SALGADO¹³, PAMELA WYATT¹⁴, FELIPE OLIVARES E.¹⁵, AVISHAY GAL-YAM¹⁶, AND MASAO SAKO¹⁷

¹ Kavli Institute for the Physics and Mathematics of the Universe (Kavli IPMU, WPI), Todai Institutes for Advanced Study, the University of Tokyo, 277-8583 Kashiwa, Japan; gaston.folatelli@ipmu.jp

² Las Campanas Observatory, Carnegie Observatories, Casilla 601, La Serena, Chile

³ Departamento de Astronomía, Universidad de Chile, Casilla 36-D, Santiago, Chile

⁴ N. Copernicus Astronomical Center, ul. Bartycka 18, 00-716 Warszawa, Poland

⁵ Department of Physics and Astronomy, Aarhus University, Ny Munkegade 120, DK-8000 Aarhus C, Denmark

⁶ Observatories of the Carnegie Institution of Washington, 813 Santa Barbara Street, Pasadena, CA 91101, USA

⁷ Infrared Processing and Analysis Center, Caltech/Jet Propulsion Laboratory, Pasadena, CA 91125, USA

⁸ Department of Astrophysical Sciences, Princeton University, 4 Ivy Ln., Princeton, NJ 08544, USA

⁹ George P. and Cynthia Woods Mitchell Institute for Fundamental Physics and Astronomy, Department of Physics and Astronomy, Texas A&M University, College Station, TX 77843, USA

¹⁰ Departamento de Ciencias Físicas, Universidad Andres Bello, Avda. República 252, Santiago, Santiago RM, Chile

¹¹ Departamento de Física y Astronomía, Universidad de Valparaíso, Av. Gran Bretaña 1111, Valparaíso, Chile

¹² Argelander Institut für Astronomie, Universität Bonn, Auf dem Hügel 71, D-53111 Bonn, Germany

¹³ Leiden Observatory, Leiden University, P.O. Box 9513, NL-2300 RA Leiden, The Netherlands

¹⁴ National Snow and Ice Data Center, University of Colorado, Boulder, CO 80309, USA

¹⁵ Max-Planck-Institut für Extraterrestrische Physik, Giessenbachstraße 1, D-85748 Garching, Germany

¹⁶ Department of Particle Physics and Astrophysics, Weizmann Institute of Science, Israel

¹⁷ Department of Physics and Astronomy, University of Pennsylvania, Philadelphia, PA 19104, USA

Received 2012 December 3; accepted 2013 May 20; published 2013 July 25

ABSTRACT

This is the first release of optical spectroscopic data of low-redshift Type Ia supernovae (SNe Ia) by the *Carnegie Supernova Project* including 604 previously unpublished spectra of 93 SNe Ia. The observations cover a range of phases from 12 days before to over 150 days after the time of *B*-band maximum light. With the addition of 228 near-maximum spectra from the literature, we study the diversity among SNe Ia in a quantitative manner. For that purpose, spectroscopic parameters are employed such as expansion velocities from spectral line blueshifts and pseudo-equivalent widths (pW). The values of those parameters at maximum light are obtained for 78 objects, thus providing a characterization of SNe Ia that may help to improve our understanding of the properties of the exploding systems and the thermonuclear flame propagation. Two objects, namely, SNe 2005M and 2006is, stand out from the sample by showing peculiar Si II and S II velocities but otherwise standard velocities for the rest of the ions. We further study the correlations between spectroscopic and photometric parameters such as light-curve decline rate and color. In agreement with previous studies, we find that the pW of Si II absorption features are very good indicators of light-curve decline rate. Furthermore, we demonstrate that parameters such as $pW2$ (Si II 4130) and $pW6$ (Si II 5972) provide precise calibrations of the peak *B*-band luminosity with dispersions of ≈ 0.15 mag. In the search for a secondary parameter in the calibration of peak luminosity for SNe Ia, we find a $\approx 2\sigma$ – 3σ correlation between *B*-band Hubble residuals and the velocity at maximum light of S II and Si II lines.

Key words: galaxies: distances and redshifts – supernovae: general – techniques: spectroscopic

Online-only material: color figures, extended figure, machine-readable tables

1. INTRODUCTION

Type Ia supernovae (SNe Ia) are extremely important astrophysical objects due to their connection with stellar evolution in binary systems, and with the chemical enrichment and energy deposition of the interstellar medium. They are also very useful in the determination of extragalactic distances and thereby in the study of the cosmological expansion rate. Due to an empiri-

cal calibration of the luminosity of SNe Ia based on the decline rate of the light curve (Phillips 1993), it has been possible to measure precise relative distances out to very large look-back times. This led to the surprising discovery of the accelerated expansion of the universe and the introduction of dark energy as its currently dominant component (Riess et al. 1998; Perlmutter et al. 1999).

Present SN-Ia experiments employ a two-parameter luminosity calibration by adding a color term in the cosmological fits, as first introduced by Tripp (1998). Such an approach has allowed the equation-of-state parameter, w , of dark energy to be constrained to within 10% by comparing low- and high-redshift SN-Ia samples (see, e.g., Riess et al. 2007; Freedman et al. 2009; Hicken et al. 2009; Amanullah et al. 2010; Sullivan

* This paper includes data gathered with the 6.5 m Magellan Telescopes located at Las Campanas Observatory, Chile and the Gemini Observatory, Cerro Pachon, Chile (Gemini Program GS-2008B-Q-56). Based on observations collected at the European Organisation for Astronomical Research in the Southern Hemisphere, Chile (ESO Programs 076.A-0156, 078.D-0048, 080.A-0516, and 082.A-0526).

et al. 2011; Suzuki et al. 2012). This is due to a precision of about 0.1–0.15 mag in the peak luminosity after calibrating with respect to decline rate and color. Efforts aimed at further improving the calibration have searched for yet a third parameter¹⁸ which would correlate with luminosity independently of the other two parameters. As detailed at the end of this Introduction, many such attempts involve optical spectra, which provide more detailed information than broadband photometry. Moreover, spectra are a key to understanding the physical properties of the explosion and therefore are fundamental for providing theoretical support for the use of SNe Ia as distance indicators.

The existence of SN-Ia subtypes has been known for the last two decades. Not long after the definition of SNe Ia as a spectroscopic SN class, examples of diversity in spectral properties started to be found as more data were gathered. Branch (1987) showed the case of SN 1984A, an object whose spectrum displayed the same lines as the rest of SNe Ia and seemingly no difference in peak brightness, but whose expansion velocities were significantly higher. This was followed by the discovery of SN 1986G (Phillips et al. 1987), SN 1991T (Filippenko et al. 1992b; Phillips et al. 1992), and SN 1991bg (Filippenko et al. 1992a; Leibundgut et al. 1993), which gave evidence of a variety in line strengths, this time related with differences in peak luminosity and color.

With time it was observed that the spectroscopic diversity was not due to rare exceptions but that some SN-Ia subclasses could be identified (Li et al. 2001). SNe 1991T and 1991bg became prototypes of their own subgroups comprising significant fractions of the total SN-Ia population (e.g., Li et al. 2010 find fractions of >9% and 18%, respectively, for these subclasses). While 1991bg-like SNe are clearly identifiable through their photometric properties, the distinction of 1991T-like objects from normal SNe Ia relies on pre-maximum spectroscopy, which makes it more difficult to establish.

Nugent et al. (1995) first quantified the spectral diversity using flux and line strength ratios, and provided an explanation by means of a temperature sequence due, in turn, to different amounts of synthesized ^{56}Ni . Spectral line ratios such as $\mathcal{R}(\text{Si II})$, defined between the absorption depths of Si II $\lambda 5972$ and $\lambda 6355$ lines, were found to be correlated with the decline rate parameter, $\Delta m_{15}(B)$ (Phillips 1993), and thus with luminosity. The diversity in expansion velocity did not fit into this picture, however, and it was pointed out that Si II velocities do not correlate with $\mathcal{R}(\text{Si II})$ or $\Delta m_{15}(B)$ (Hatano et al. 2000). A one-parameter scenario regulated solely by ejecta temperature is further complicated by opacity and line-blanketing effects (Höflich & Khokhlov 1996; Pinto & Eastman 2000; Kasen & Woosley 2007).

Based on line ratios, expansion velocities, and light-curve decline rates, Benetti et al. (2005) provided a quantitative classification of SNe Ia into three subtypes. Their high- and low-velocity-gradient classes (HVG and LVG, respectively) are distinguished by the post-maximum rate of Si II $\lambda 6355$ velocity decline, named \dot{v} . The third subtype, FAINT, includes objects with large $\Delta m_{15}(B)$ which also show large \dot{v} values. An alternative classification scheme was introduced by Branch et al. (2006) based on absorption equivalent widths of the Si II $\lambda 5972$ and $\lambda 6355$ lines at maximum light. They distinguished between “core normal” (CN), “cool” (CL), “broad line” (BL), and “shallow silicon” (SS) SNe Ia. The prototypes of the BL

and CL classes are SN 1984A and SN 1991bg, respectively, while the SS class includes SN 1991T- and SN 2002cx-like objects. There is a rough correspondence between the BL and HVG groups, and also between the CL and FAINT groups. LVG SNe roughly include CN and SS classes. More recently, Wang et al. (2009) divided their sample into “normal,” “1991bg-like,” “1991T-like,” and “HV” (high-velocity) SNe. HV SNe are differentiated from normal events using the Si II $\lambda 6355$ velocity within one week from maximum light, with HV objects being somewhat arbitrarily defined as those SNe whose velocity lies 3σ above the average velocities of 10 fiducial objects in the normal group. Using this definition, the HV and HVG subclasses roughly coincide.

In spite of their spectroscopic differences, both LVG and HVG objects (or normal and HV objects) are usually employed for determining distances, as they seem to obey the same luminosity–decline rate calibration. However, Wang et al. (2009) showed that host-galaxy extinction of HV SNe Ia may obey a different wavelength dependence than that of normal SNe Ia. Such a difference would affect the color correction and the derived distances. More recently, Foley & Kasen (2011) reanalyzed the same data set and suggested a difference in intrinsic color between HV and normal SNe Ia, possibly as a consequence of increased line blanketing in HV SNe. They show that the scatter in the Hubble diagram is reduced when using only normal SNe Ia. Interestingly, Maeda et al. (2010a) proposed a unification scenario based on asymmetric explosion and line-of-sight effects to explain the observed velocity differences among LVG and HVG SNe. We note that signatures of unburned material in the ejecta of SNe Ia—namely, C II lines in pre-maximum light spectra—have been found with larger incidence in LVG SNe than in HVG objects (Parrent et al. 2011; Thomas et al. 2011a; Folatelli et al. 2012; Silverman & Filippenko 2012). This may indicate a different explosion mechanism for both groups.

Several attempts have been made to quantify the spectroscopic properties of SN-Ia subtypes and to look for an improved calibration of the peak luminosity adopting different approaches. Pseudo-equivalent widths (pW) of absorptions were introduced by Folatelli (2004) as a way to quantify the differences in line strengths. Hachinger et al. (2006) employed this type of measurements and expansion velocities to study correlations with $\Delta m_{15}(B)$ on a sample of nearby SNe Ia. Being less sensitive to noise and flux-calibration issues than flux ratios and line depths, pW measurements have been used to compare general properties of low- and high-redshift SNe (Garavini et al. 2007; Arsenijevic et al. 2008; Bronder et al. 2008; Walker et al. 2011). A similar analysis based on wavelet decomposition was presented by Wagers et al. (2010). Flux ratios at selected optical wavelengths have been studied as luminosity indicators by Bongard et al. (2006). More thorough analyses of flux ratios have been presented recently (Bailey et al. 2009; Blondin et al. 2011b) in search of a luminosity calibrator which would reduce the scatter in the SN-Ia Hubble diagram. Foley et al. (2011) used a large sample of SNe Ia to measure expansion velocities and pW and find correlations with intrinsic color. They find a larger scatter in intrinsic color for high-velocity SNe than for low-velocity ones and suggest that the latter are more precise distance indicators.

The issue of SN-Ia diversity has been quantitatively addressed by Blondin et al. (2012) in the analysis of a large sample of spectra obtained by the Centre for Astrophysics (CfA) Supernova Program. These authors presented a detailed examination of the spectroscopic properties and relations between

¹⁸ Usually referred to as “secondary parameter.”

spectroscopic and photometric parameters for different SN-Ia subtypes defined in terms of Branch et al. and Wang et al classification schemes. The Berkeley Supernova Ia Program (BSNIP) has also released a significant amount of spectra and provided their careful analysis in a series of papers (Silverman et al. 2012a, 2012b, 2012c; Silverman & Filippenko 2012). The second and third papers of this series deal with the quantitative characterization of SN-Ia spectra near maximum light and with the possible improvement of distance determinations based on spectroscopic parameters.

In this paper, we present optical spectra of low-redshift SNe Ia gathered by the Carnegie Supernova Project (CSP; Hamuy et al. 2006) between 2004 and 2009. Expansion velocities and pW measurements are used to revisit the definition of SN-Ia subtypes and to search for correlations with photometric properties.

In Section 2, we present the sample of SNe and the spectroscopic observations and data reduction performed by the CSP. In Section 3, we describe the methods utilized to obtain spectroscopic parameters such as expansion velocities and pseudo-equivalent widths. Section 4 is devoted to a quantitative analysis of the spectroscopic diversity among SNe Ia with special attention to the definition of subtypes and the correlations between different spectral parameters. Section 5 focuses on the connection between spectroscopic and photometric parameters with the aim of improving the precision in the luminosity calibration of SNe Ia. Finally, in Section 6 we discuss the results and provide some concluding remarks.

2. DATA

We present optical spectroscopic data for a sample of 93 SNe Ia observed by the CSP between 2004 and 2009. The data set amounts to 832 optical spectra, 569 of which were obtained by the CSP, 35 were provided by other observers, and 228 were taken from the literature. In the following, we describe the SNe included in this work, and the observing and reduction procedures applied to the CSP data.

2.1. Supernova Sample

The CSP carried out follow-up campaigns to obtain optical and near-infrared (NIR) light curves and optical spectroscopy of nearby ($z \lesssim 0.08$) SNe of all types. Between 2004 September and 2009 May over 250 objects were monitored, among which 129 were SNe Ia. High-quality optical and NIR light curves of 36 of these were published by Contreras et al. (2010), and their analysis was presented in the work of Folatelli et al. (2010). Light curves of additional 50 SNe Ia were made available by Stritzinger et al. (2011).

Along with well-sampled light curves, the CSP collected spectra for most of the SNe. However, due to the relative scarcity of spectroscopy time, the temporal sampling obtained was more sporadic than that of the photometry. In this work, we have collected the spectra of the SNe Ia with light curves published by Contreras et al. (2010) and Stritzinger et al. (2011) plus several SNe observed more recently for which clean photometry was obtained without performing subtraction of the host-galaxy light—i.e., because they were bright enough and isolated from their hosts. Note that we do not include SN 2005hk—a 2002cx-like object observed by the CSP (Phillips et al. 2007)—in the analysis due to the lack of CSP spectra near maximum light.

Table 1 lists the sample of SNe Ia selected for this work along with the amount and span of spectroscopy epochs, and spectral classification as defined in Section 4. Additional information

in Table 1 includes redshift and photometric parameters. The sample includes a large variety of SNe Ia, as can be inferred from the wide distribution of light-curve decline rates parameterized by $\Delta m_{15}(B)$ and shown in the top left panel of Figure 1.

For most of the objects in the sample, the heliocentric redshifts given in Table 1 were obtained from the NASA/IPAC Extragalactic Database (NED). Whenever possible, we have used CSP spectra to verify the quoted values by measuring host-galaxy lines. For 55 spectra of 34 SNe, we obtained a very good agreement with an average difference in z of 0.00009 and a dispersion of 0.00055 (165 km s $^{-1}$). For SNe 2005ag, 2006is, and 2006lu, no information on the host galaxies or their redshifts is available in NED, so we have adopted our measured values, as indicated in Table 1. These redshift values were used to put the spectra in the rest frame. As shown in Figure 1, the SN sample covers a range of redshifts up to $z = 0.083$, with $\approx 80\%$ of the objects closer than $z = 0.04$.

2.2. Observations and Reductions

The procedures followed by the CSP for spectroscopic observations and reductions were described by Hamuy et al. (2006). As mentioned there, most of the data were obtained with the 2.5 m du Pont Telescope at Las Campanas Observatory, using the Wide Field CCD Camera (WFCCD) in long-slit spectroscopy mode. Other instruments used to improve our spectroscopic time coverage were the Las Campanas Modular Spectrograph at the du Pont, the Low Dispersion Survey Spectrograph (LDSS2; Allington-Smith et al. 1994) on the Magellan Clay 6.5 m telescope, and the Ritchey-Chrétien spectrograph at the 1.5 m CTIO telescope, operated by the SMARTS consortium. In addition to these, more recently we have also employed, at Las Campanas: LDSS3 on the Magellan Clay telescope (an upgrade of LDSS2, with new grisms and different long slits); the Inamori Magellan Areal Camera and Spectrograph (IMACS; Dressler et al. 2011) on the Magellan Baade 6.5 m telescope, in its long ($f/4$) and short ($f/2$) camera modes, with different combinations of gratings/grisms and slits; the Boller and Chivens spectrograph at the du Pont telescope; and finally, a few spectra have been obtained using the Magellan Echelle (MagE; Marshall et al. 2008) spectrograph on the Magellan Clay telescope. We have also obtained single nights with the New Technology Telescope (NTT) and the 3.6 m Telescope at ESO-La Silla, using the ESO Multi-Mode Instrument (EMMI; Dekker et al. 1986) in medium resolution spectroscopy mode (at the NTT) and the ESO Faint Object Spectrograph and Camera (EFOSC; Buzzoni et al. 1984) at the 3.6 m and NTT telescopes. A few spectra have been obtained with the Gemini Multi-Object Spectrograph (GMOS; Hook et al. 2004) mounted on the Gemini South Telescope.

About 80% of our spectra were obtained with the WFCCD, with most of the remaining 20% secured with EMMI, LDSS2/3, and IMACS. In Table 2, we provide a complete journal of the spectroscopic observations considered in this work, giving for each spectrum the spectral coverage, FWHM resolution, exposure time, and airmass in the middle of the observation. UT and Julian dates are also provided along with the estimated rest-frame phase with respect to maximum light in the B band.¹⁹

In its spectroscopic monitoring, the CSP obtained at least one spectrum of the vast majority of the SNe which were selected

¹⁹ Hereafter the term “maximum light” refers to the time of B -band maximum, and all epochs will indicate the amount of rest-frame days with respect to that date.

Table 1
Summary of Observations, Classification, and Photometric Properties of the SN-Ia Sample

SN	N	Epoch Range	SNID	Wang Type	Branch Type	z_{Helio}	z_{CMB}	$T_B(\text{max})$	RJD	m_B (mag)	$\Delta m_{15}(B)$ (mag)	$E(B - V)$ Gal (mag)	$(B_{\text{max}} - V_{\text{max}})$ (mag)	Low Redd.	ΔM_B (mag)
(1)	(2)	(3)	(4)	(5)	(6)	(7)	(8)	(9)	(10)	(11)	(12)	(13)	(14)	(15)	
2004dt	5	+23.2 + 102.6	Normal	HV	BL	0.01973	0.01883	53239.1	15.000(035)	1.235(072)	0.023	-0.046(047)	...	-0.39(18)	
2004ef	8	-8.0 + 37.5	Normal	HV	BL	0.03099	0.02979	53264.0	16.828(019)	1.379(061)	0.056	0.102(027)	...	-0.09(12)	
2004eo	3	-10.5 + 24.9	Normal	N	CL	0.01570	0.01475	53278.2	15.067(011)	1.365(063)	0.108	0.055(020)	Y	-0.16(17)	
2004ey	4	-0.3 + 47.9	Normal	N	CN	0.01579	0.01464	53303.9	14.713(011)	0.930(013)	0.139	-0.063(022)	Y	0.15(16)	
2004gc	4	+10.8 + 33.1	Normal	0.03070	0.03074	53324.6	16.649(028)	1.088(055)	0.206	0.150(037)	...	-0.25(13)	
2004gs	2	-3.1 + 2.7	Normal	N	CL	0.02665	0.02752	53356.0	17.132(017)	1.613(082)	0.031	0.158(044)	...	0.07(16)	
2004gu	1	-4.3	Normal	91T	SS	0.04586	0.04693	53363.4	17.478(017)	0.888(299)	0.027	0.189(021)	...	-0.33(23)	
2005A	3	+4.1 + 32.6	Normal	HV	BL	0.01914	0.01835	53380.4	18.141(151)	1.222(183)	0.030	1.019(192)	...	-0.10(58)	
2005M	9	+0.3 + 68.5	91T	SS	0.02462	0.02560	53405.4	15.924(038)	0.844(066)	0.031	0.018(039)	Y	-0.03(15)		
2005W	1	-7.3	...	N	BL	0.00889	0.00796	53411.8	14.138(009)	1.225(071)	0.071	0.090(070)	
2005ag	4	-0.1 + 46.1	Normal	N	BL	0.0798 ^a	0.0804	53414.0	18.447(060)	0.920(169)	0.041	-0.003(125)	Y	-0.08(37)	
2005al	7	+14.7 + 49.3	Normal	0.01240	0.01329	53429.9	14.870(020)	1.166(031)	0.055	-0.034(022)	Y	0.27(18)	
2005am	7	+7.9 + 38.6	Normal	HV	BL	0.00790	0.00897	53436.6	13.639(009)	1.514(076)	0.054	0.045(015)	Y	...	
2005be	4	+7.0 + 18.6	Normal	0.03502	0.03562	53460.6	16.887(035)	1.472(077)	0.034	0.019(046)	...	-0.27(16)	
2005bg	3	+2.0 + 8.8	Normal	N	SS	0.02309	0.02417	53470.7	15.881(042)	1.021(079)	0.032	0.041(061)	...	-0.13(20)	
2005bl	2	-8.4 - 4.5	91bg	91bg	CL	0.02406	0.02513	53484.2	18.221(031)	1.802(038)	0.029	0.558(035)	...	0.12(14)	
2005bo	2	-1.0 - 0.0	Normal	N	CN	0.01390	0.01502	53479.8	15.662(009)	1.299(078)	0.046	0.290(017)	...	-0.19(16)	
2005el	4	-7.2 + 14.6	Normal	N	CN	0.01491	0.01490	53647.1	14.821(021)	1.348(040)	0.114	-0.014(022)	Y	-0.22(16)	
2005eq	2	-5.4 + 7.2	91T	SS	0.02898	0.02837	53654.4	16.306(026)	0.773(022)	0.077	0.099(042)	...	-0.05(14)		
2005hc	3	-5.1 + 0.7	Normal	N	CN	0.04594	0.04501	53667.1	17.305(033)	0.912(092)	0.029	0.004(036)	Y	0.08(13)	
2005iq	2	+10.5 + 37.6	Normal	0.03404	0.03295	53687.7	16.776(039)	1.250(109)	0.022	-0.020(042)	Y	0.06(16)	
2005kc	4	+0.9 + 28.4	Normal	N	CN	0.01512	0.01390	53697.7	15.510(011)	1.200(074)	0.132	0.179(028)	...	0.20(18)	
2005ke	12	-0.6 + 128.5	91bg	91bg	CL	0.00488	0.00449	53698.3	14.772(021)	1.762(048)	0.027	0.661(023)	Y	-0.28(11)	
2005ki	5	-7.6 + 142.3	Normal	N	CN	0.01921	0.02038	53705.6	15.543(031)	1.371(050)	0.032	-0.008(031)	Y	-0.22(15)	
2005ku	3	-1.7 + 28.8	Normal	HV	CN	0.04544	0.04421	53698.4	17.483(024)	1.019(057)	0.053	0.102(030)	...	-0.05(11)	
2005lu	6	+10.4 + 16.2	Normal	0.03201	0.03132	53711.9	17.279(018)	0.882(033)	0.025	0.195(022)	...	0.37(10)	
2005na	6	+11.7 + 75.8	Normal	N	CN	0.02632	0.02683	53739.7	15.981(055)	0.944(118)	0.078	-0.026(058)	...	-0.03(21)	
2006D	11	-5.4 + 92.7	Normal	N	CN	0.00853	0.00965	53757.3	14.136(006)	1.388(011)	0.046	0.094(013)	Y	...	
2006X	13	-5.9 + 93.3	Normal	HV	BL	0.00524	0.00633	53785.8	15.218(048)	1.115(029)	0.026	1.196(058)	...	0.11(22)	
2006ax	8	-10.2 + 19.2	Normal	N	CN	0.01674	0.01797	53827.1	15.002(028)	1.016(016)	0.050	-0.048(028)	Y	-0.11(15)	
2006bd	1	+12.9	91bg	91bg	CL	0.02572	0.02681	53811.5	17.650(103)	1.647(017)	0.028	0.249(123)	Y	0.37(36)	
2006bh	2	+8.3 + 16.3	Normal	0.01085	0.01050	53833.4	14.348(025)	1.428(049)	0.026	-0.032(025)	Y	0.06(22)	
2006br	1	+0.5	Normal	HV	BL	0.02459	0.02554	53851.2	18.969(039)	1.161(032)	0.025	0.884(046)	...	0.42(16)	
2006dd	6	-11.4 + 193.1	Normal	0.00587	0.00551	53919.4	12.241(009)	1.079(014)	0.021	-0.071(013)	Y	0.29(06)	
2006ef	4	+36.3 + 101.2	Normal	HV	BL	0.01788	0.01702	53969.7	15.411(020)	1.326(015)	0.024	0.027(024)	...	-0.02(15)	
2006ej	4	+28.4 + 55.0	Normal	HV	BL	0.02045	0.01935	53975.6	15.676(026)	1.297(055)	0.035	-0.011(037)	Y	0.08(16)	
2006eq	2	+25.2 + 26.1	Normal	N	CL	0.04950	0.04839	53977.1	18.402(023)	1.662(055)	0.048	0.223(026)	...	-0.14(10)	
2006et	5	+10.5 + 75.9	Normal	N	CN	0.02217	0.02119	53993.0	15.963(008)	0.847(063)	0.019	0.177(011)	...	-0.01(12)	
2006ev	4	+14.1 + 29.6	Normal	0.02873	0.02762	53989.1	16.658(016)	1.323(012)	0.091	0.048(019)	...	0.10(10)	
2006fw	4	-6.8 + 17.6	Normal	N	CN	0.08300	0.08204	54002.7	18.927(039)	1.078(109)	0.032	0.015(060)	...	0.19(19)	
2006gj	7	+4.1 + 25.5	Normal	N	CL	0.02835	0.02777	53999.6	17.272(009)	1.533(009)	0.083	0.222(012)	...	0.07(09)	
2006gt	5	+0.3 + 17.4	91bg	91bg	CL	0.04477	0.04367	54003.5	18.229(020)	1.851(288)	0.037	0.256(024)	Y	-0.31(23)	
2006hb	12	+7.9 + 74.0	86G	91bg	...	0.01534	0.01535	53998.7	15.296(029)	1.252(011)	0.027	0.092(037)	...	-0.03(18)	
2006hx	2	-8.1 - 3.2	Normal	N	SS	0.04549	0.04444	54022.1	17.390(031)	1.151(039)	0.030	-0.184(073)	...	0.53(21)	
2006is	15	+1.4 + 46.0	Normal	HV	CN	0.0314 ^a	0.0314	54008.4	16.072(017)	0.796(009)	0.034	0.047(023)	...	-0.38(10)	
2006kf	6	-5.4 + 28.9	Normal	N	CL	0.02130	0.02081	54041.3	15.817(005)	1.583(042)	0.247	-0.016(033)	Y	-0.13(14)	
2006lu	3	+8.3 + 20.7	Normal	0.0534 ^a	0.0544	54034.1	16.940(016)	0.908(009)	0.116	-0.153(020)	...	-0.28(07)	
2006mr	11	-1.5 + 63.1	91bg	91bg	CL	0.00587	0.00551	54050.1	15.345(011)	1.776(037)	0.021	0.708(121)	...	0.75(34)	
2006ob	1	+22.9	Normal	0.05924	0.05830	54063.4	18.242(039)	1.452(162)	0.033	0.047(104)	...	-0.08(31)	
2006os	2	-1.0 + 19.3	Normal	N	CL	0.03281	0.03210	54062.8	16.912(020)	1.440(070)	0.148	0.184(024)	...	-0.44(11)	
2006ot	2	+19.7 + 24.5	peculiar	HV	BL	0.05294	0.05219	54061.9	17.736(022)	0.844(005)	0.018	0.092(028)	...	-0.01(09)	
2006py	1	+15.1	Normal	0.05790	0.05668	54070.6	17.881(016)	1.018(030)	0.065	0.064(021)	...	-0.11(07)	
2007A	2	-6.2 + 0.7	Normal	N	CN	0.01765	0.01648	54112.8	15.695(012)	0.924(025)	0.074	0.222(033)	...	0.09(16)	
2007N	5	+6.0 + 83.9	91bg	91bg	CL	0.01288	0.01401	54123.8	18.085(049)	1.779(094)	0.041	0.948(053)	...	0.22(23)	
2007S	6	-12.6 + 33.5	91T	91T	SS	0.01388	0.01503	54144.6	15.789(013)	0.947(026)	0.028	0.371(031)	...	-0.03(17)	
2007af	8	-10.4 + 57.1	Normal	N	BL	0.00546	0.00629	54174.3	13.330(014)	1.203(034)	0.031	0.196(030)	
2007ai	5	-1.9 + 13.6	91T	91T	SS	0.03166	0.03201	54171.8	15.484(009)	0.740(012)	0.332	-0.173(011)	...	-0.36(08)	
2007al	4	+0.9 + 13.7	91bg	91bg	CL	0.01212	0.01327	0.042	
2007as	4	-2.7 + 38.6	Normal	HV	BL	0.01757	0.01791	54181.3	14.821(006)	1.217(010)	0.142	-0.073(008)	...	-0.37(13)	
2007ax	1	-2.0	91bg	91bg	CL	0.00686	0.00764	54187.6	16.201(029)	1.958(089)	0.054	0.684(031)	Y	...	
2007ba	2	+3.1 + 6.0	91bg	91bg	CL	0.03851	0.03908	54196.6	17.664(117)	1.851(065)	0.038	0.248(138)	...	-0.60(40)	
2007bc	3	-0.5 + 7.4	Normal	N	CL	0.02077	0.02077	54200.1	15.896(008)	1.207(011)	0.022	0.124(009)	...	-0.15(11)	
2007bd	4	-7.2 + 13.1	Normal	HV	BL	0.03102	0.03196	54207.1	16.551(022)	1.234(065)	0.034	0.029(024)	...	-0.21(11)	

Table 1
(Continued)

SN	N	Epoch Range	SNID Type	Wang Type	Branch Type	z_{Helio}	z_{CMB}	$T_B(\text{max})$	RJD	m_B (mag)	$\Delta m_{15}(B)$ (mag)	$E(B - V)$ Gal (mag)	$(B_{\text{max}} - V_{\text{max}})$ (mag)	Low Redd.	ΔM_B (mag)
(1)	(2)	(3)	(4)	(5)	(6)	(7)	(8)	(9)	(10)	(11)	(12)	(13)	(14)	(15)	
2007bm	2	+4.1 + 6.9	Normal	N	CN	0.00621	0.00621	54224.6	14.377(007)	1.194(013)	0.036	0.472(009)	
2007ca	2	+1.4 + 4.2	Normal	N	CN	0.01407	0.01508	54227.3	15.892(014)	0.904(032)	0.067	0.279(026)	...	0.35(16)	
2007hj	3	+6.3 + 26.9	Normal	HV	CL	0.01411	0.01289	54349.3	15.585(033)	1.758(081)	0.085	0.224(047)	Y	-0.10(22)	
2007jg	5	-1.2 + 40.1	Normal	HV	BL	0.03713	0.03660	54367.2	17.181(045)	1.311(077)	0.107	0.028(048)	Y	0.06(16)	
2007jh	1	+42.8	86G	91bg	...	0.04080	0.04029	54365.3	18.321(012)	1.720(008)	0.000	0.349(018)	...	-0.20(07)	
2007le	12	-9.0 + 44.6	Normal	HV	BL	0.00672	0.00553	54398.7	13.875(009)	0.971(072)	0.033	0.292(011)	
2007nq	8	+3.3 + 37.8	Normal	HV	BL	0.04503	0.04393	54398.2	17.246(009)	1.471(010)	0.035	0.004(011)	Y	-0.34(06)	
2007on	19	-3.9 + 284.3	Normal	N	CL	0.00649	0.00619	54419.7	13.023(008)	1.860(026)	0.012	0.088(011)	Y	...	
2007sr	14	+13.8 + 133.9	Normal	0.00548	0.00666	54448.0	12.706(021)	0.919(039)	0.047	0.047(030)	
2007ux	3	+2.3 + 53.7	Normal	N	CL	0.03091	0.03202	54466.4	17.353(044)	1.634(103)	0.045	0.181(062)	...	-0.12(20)	
2008C	5	+4.3 + 54.4	Normal	N	SS	0.01662	0.01708	54466.3	15.287(010)	1.113(015)	0.084	0.094(013)	...	-0.18(13)	
2008R	5	+2.2 + 26.9	91bg	91bg	CL	0.01350	0.01290	54494.3	15.224(039)	1.823(031)	0.072	0.085(044)	...	-0.13(21)	
2008ar	8	-8.1 + 47.2	Normal	N	CN	0.02615	0.02727	54534.2	16.259(038)	0.884(069)	0.038	0.100(054)	...	-0.08(18)	
2008bc	8	-9.0 + 36.3	Normal	N	CN	0.01509	0.01572	54548.7	14.624(007)	0.823(021)	0.263	-0.038(015)	...	-0.08(15)	
2008bf	10	-8.5 + 42.1	Normal	N	CN	0.02403	0.02510	54554.5	15.779(022)	0.872(040)	0.036	-0.066(031)	Y	0.08(13)	
2008bq	4	+0.6 + 33.4	Normal	N	CN	0.03400	0.03446	54562.9	16.303(006)	0.919(012)	0.090	-0.027(008)	...	-0.24(07)	
2008fp	15	-2.8 + 156.1	Normal	N	CN	0.00566	0.00629	54729.7	13.829(020)	0.838(047)	0.196	0.491(028)	
2008gl	5	-1.5 + 54.6	Normal	N	BL	0.03402	0.03297	54768.2	16.845(022)	1.289(045)	0.028	0.050(031)	Y	-0.09(12)	
2008gp	3	-5.7 + 42.6	Normal	0.03341	0.03285	54778.6	16.455(031)	0.973(113)	0.120	0.033(043)	Y	-0.19(16)	
2008hu	3	+3.9 + 20.1	Normal	HV	BL	0.04970	0.05056	54806.6	17.868(043)	1.487(095)	0.107	0.114(061)	Y	-0.34(19)	
2008hv	10	-6.0 + 71.0	Normal	N	CN	0.01255	0.01359	54816.8	14.672(006)	1.253(006)	0.032	0.039(009)	Y	-0.24(16)	
2008ia	8	-2.0 + 59.5	Normal	N	BL	0.02171	0.02233	54812.9	14.871(007)	1.323(012)	0.228	-0.169(011)	Y	-0.62(10)	
2009D	7	-3.9 + 76.9	Normal	N	CN	0.02501	0.02467	54840.7	15.789(016)	0.845(028)	0.053	0.018(023)	Y	-0.08(11)	
2009F	7	-5.0 + 45.3	91bg	91bg	CL	0.01296	0.01292	54841.8	16.929(025)	1.966(045)	0.104	0.635(036)	Y	-0.04(20)	
2009Y	13	-5.5 + 75.7	Normal	HV	BL	0.00935	0.01011	54876.4	14.042(032)	0.883(057)	0.102	0.114(045)	
2009aa	11	-7.8 + 39.9	Normal	N	CN	0.02731	0.02850	54878.7	16.355(023)	1.118(045)	0.034	0.030(033)	Y	-0.07(13)	
2009ab	5	-10.2 + 4.7	Normal	N	CN	0.01117	0.01087	54883.8	14.652(046)	1.207(092)	0.214	0.065(065)	...	0.19(28)	
2009ad	6	-8.3 + 32.5	Normal	N	SS	0.02840	0.02834	54886.1	16.074(096)	0.882(174)	0.111	-0.006(136)	...	-0.07(41)	
2009ag	6	-3.5 + 54.9	Normal	N	BL	0.00864	0.00925	54889.2	14.589(041)	0.967(076)	0.254	0.241(058)	

Notes. Column 1: SN name; Column 2: number of spectroscopic epochs; Column 3: epoch range of previously unpublished spectra relative to B -band maximum light; Column 4: spectral subtype based on SNID comparisons (Blondin & Tonry 2007); Column 5: spectral subtype based on the scheme of Wang et al. (2009): normal (N), SN 1991T-like (91T), SN 1991bg-like (91bg), high velocity (HV); Column 6: spectral subtype based on pW (Branch et al. 2006): core normal (CN), cool (CL), broad line (BL), shallow silicon (SS); Column 7: heliocentric redshift from the NASA/IPAC Extragalactic Database (NED), except when otherwise noted; Column 8: redshift in the 3K CMB frame converted from z_{Helio} using the application in NED; Column 9: reduced Julian date (JD – 2,400,000) of B -band maximum light; Column 10: K -corrected, apparent B -band peak magnitude, corrected for dust extinction in the Galaxy (uncertainties in thousandth of mag); Column 11: observed decline rate, $\Delta m_{15}(B)$ (uncertainties in thousandth of mag); Column 12: Galactic reddening (NED); Column 13: pseudo-color at maximum light (uncertainties in thousandth of mag); Column 14: “Y” indicates the SN is considered to have suffered negligible host-galaxy reddening; Column 15: B -band absolute peak magnitude residual (see Section 5; uncertainties in hundredth of mag).

^a Redshift computed from spectrum of the host galaxy obtained by the CSP.

for photometric follow-up. Among the 36 SNe Ia included in Contreras et al. (2010), only SN 2005ir at $z = 0.076$ was not observed spectroscopically by our program. Among the additional 50 objects published by Stritzinger et al. (2011), no spectra were obtained for only five SNe, namely 2005hj, 2005mc, 2006bt, 2007hx, and 2007mm. As can be seen in the bottom left panel of Figure 1 which shows the distribution of the number of spectroscopic epochs for all the SNe in the present sample, for most of the objects we obtained between 2 and 5 spectroscopic epochs. Moreover, several SNe were followed more intensively and for longer intervals, which allowed us to gather spectra at 10–15 different epochs.

We tried to concentrate our spectroscopic observations around the time of maximum light. For most SNe we obtained the first spectrum before or around maximum light. Specifically, for 72 out of the 93 SNe, the first spectrum was obtained earlier than 5 days after B -band maximum light (see Figure 1). In many cases the monitoring was extended up to ∼50 days after the time of B -band maximum. For the brightest objects we were able to obtain spectra to approximately +150 days.

Although most of the observations were performed without order-sorting filters, the effect of second-order contamination is negligible in most cases because SNe Ia in general do not show extremely blue colors. The flux calibration was generally performed using several spectrophotometric standards to reduce the risk of introducing second-order contamination in the calibration of the red part of the spectrum. We have evaluated the effect of second-order contamination by comparing spectra obtained with and without order-sorting filter using the Boller and Chivens spectrograph at the du Pont telescope. We have done this with several SNe observed between 2007 and 2009. In all cases, the results are in agreement within a few percent between the two instrumental setups. Unfortunately, the WFCCD spectrograph does not allow observations to be made with order-sorting filters. However, the results of the Boller and Chivens spectrograph—which has significantly greater sensitivity in the blue—indicate that the effect is negligible also in the case of the WFCCD.

Telluric features were removed from almost all the spectra using appropriate standards observed each night with the same

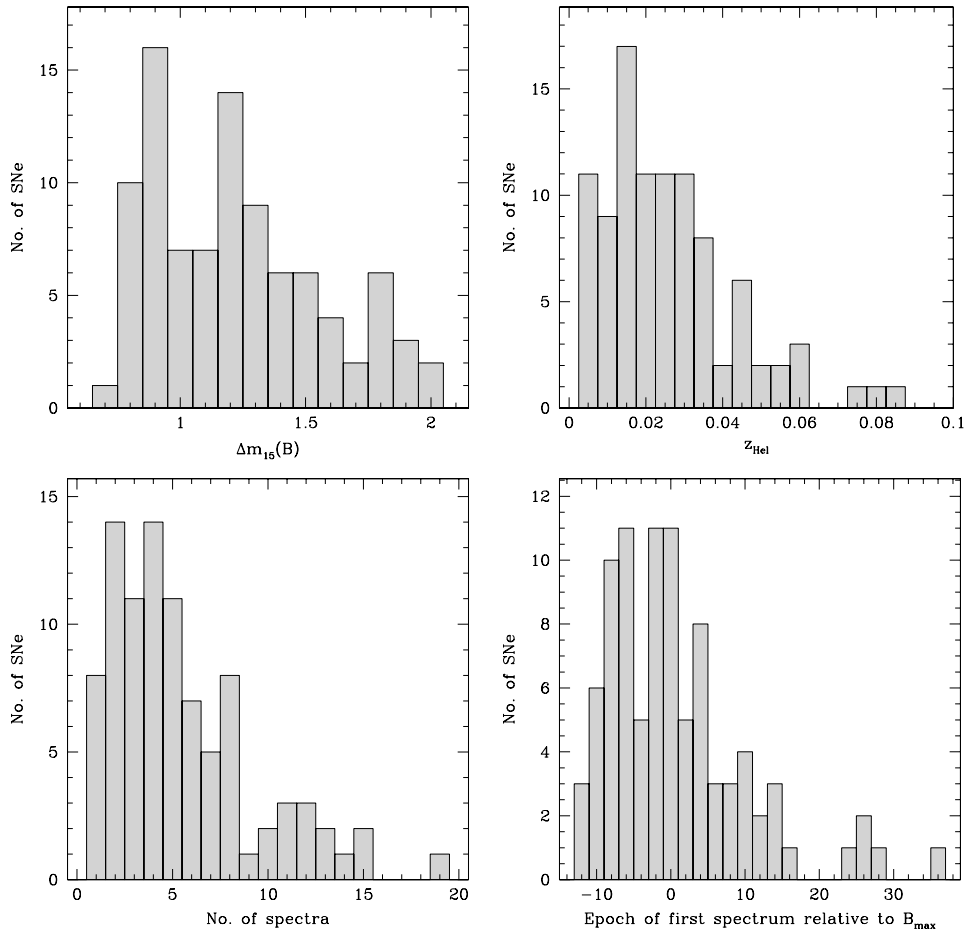


Figure 1. Top left: distribution of decline rates parameterized as $\Delta m_{15}(B)$ for the present SN sample. A wide range is covered between 0.6 and 2.0 mag. Top right: distribution of heliocentric redshifts of the present SN sample. Bottom left: distribution of the number of spectroscopy epochs per SN. Most SNe were observed between 2 and 5 times. A few were observed on more than 10 epochs. Bottom right: distribution of the epoch when the first spectrum was obtained for each SN. About 77% of the SNe were first observed spectroscopically before five days past maximum light.

slit used for the SN observations. Note that this procedure often left residuals from the strongest telluric bands which were not further corrected, as explained in detail in Hamuy et al. (2006). Only 22 of the total of 604 CSP spectra were not telluric-corrected because the necessary standards were not obtained.

To avoid light loss due to differential refraction, we carried out the vast majority of the observations by aligning the slit at the parallactic angle, especially when observing at low elevation. Also, special care was taken to fit and subtract the underlying emission from the host galaxy in order to obtain a clean SN spectrum. In order to assess the quality of the spectrophotometry, we compared synthetic photometry computed through different bandpasses with the corresponding broadband photometry. For most of the spectra the wavelength range covered allows comparison with several bandpasses. In general we find an agreement within a few percent between synthetic and observed fluxes after removal of a constant flux term. In the last column of Table 2, we provide the rms of the differences in magnitudes between the bandpasses. In some cases we were not able to perform the comparison, either because the spectrum had a wavelength coverage that was too restricted, or because the photometric data did not cover the epoch of the spectrum. When the rms was larger than ≈ 0.15 mag among at least three bandpasses we used a low-order polynomial function to correct the overall shape of the spectrum. As a further consistency check, we compared synthetic colors obtained from the spectra

with corresponding colors measured from the photometry and interpolated to the same epochs of the spectra. The comparison is shown in Figure 2. The figure shows that the majority of the spectra show color deviations within ± 0.15 mag. Most of the spectra that show larger deviations in any given color are the ones that were corrected by the procedure described above. A few spectra with a large deviation in one color index were not corrected because their wavelength span did not cover other bandpasses.

Figure 3 shows examples of spectral time-series for some of the SNe in the current sample. The complete set of plots are provided as online-only material and will be made available together with the spectroscopic data in the CSP Web site (<http://csp.obs.carnegiescience.edu>).

A number of non-CSP spectra have been included in this paper. Some of them are unpublished, including: a total of 30 spectra of SNe 2006dd, 2006ef, 2006ej, 2006et, 2006gj, 2006hb, 2006is, 2006kf, 2006lu, and 2006mr obtained with the Boller & Chivens CCD spectrograph at the Hiltner 2.4 m Telescope of the MDM Observatory; 4 spectra of SNe 2005hc, 2005ku, and 2006fw obtained during the SDSS-II Supernova Survey (Frieman et al. 2008) with the Boller & Chivens CCD spectrograph mounted on the McGraw-Hill 1.3 m Telescope of the MDM Observatory, and EMMI at the NTT telescope of ESO-La Silla; and 1 spectrum of SN 2005A obtained with the Double Spectrograph (DBSP; Oke & Gunn 1982) mounted

Table 2
Previously Unpublished Spectroscopic Observations

UT Date (1)	Reduced JD (2)	Phase (3)	Tel. (4)	Inst. (5)	Wavelength Range (Å) (6)	Resol. (Å) (7)	Exp. (s) (8)	Air- mass (9)	Phot. rms (mag) (10)
SN 2004dt									
2004-09-14.210 ^a	53262.710	23.2	DUP	WF	3800–9235	8.0	1800	1.35	0.063
2004-09-19.334 ^a	53267.834	28.2	DUP	WF	4530–9618	8.0	1800	1.20	0.109
2004-09-20.216 ^a	53268.716	29.1	DUP	WF	3800–9235	8.0	2400	1.25	0.059
2004-10-24.269	53302.769	62.5	CLA	LD	3600–9000	14.0	900	1.30	0.062
2004-12-04.153 ^b	53343.653	102.6	DUP	WF	3800–9235	8.0	1800	1.28	0.216
SN 2004ef									
2004-09-07.162 ^b	53255.662	-8.0	DUP	MS	3780–7323	2.5	4500	1.54	0.288
2004-09-08.182	53256.682	-7.1	CLA	BC	4000–7183	1.6	600	1.52	0.045
2004-09-09.267 ^b	53257.767	-6.0	CLA	LD	3650–6850	4.2	200	1.92	0.299
2004-09-10.179	53258.679	-5.1	CLA	BC	4000–7114	1.6	900	1.52	0.035

Notes. Column 1: UT date of the observation; Column 2: reduced Julian date of the observation ($JD - 2,400,000$); Column 3: phase in rest-frame days since B -band maximum light; Column 4: telescope code—3P6: ESO 3.6 m Telescope; BAA: Las Campanas Magellan I 6.5 m Baade Telescope; CLA: Las Campanas Magellan II 6.5 m Clay Telescope; DUP: Las Campanas 2.5 m du Pont Telescope; GEM: Gemini-S 8.1 m Telescope; HIL: Hiltner 2.4 m Telescope; MGH: McGraw-Hill 1.3 m Telescope; NTT: New Technology Telescope; P20: Palomar 200 inch Hale Telescope; T60: CTIO 1.5 m Telescope; Column 5: instrument code—BC: Boller & Chivens spectrograph; CS: Ritchey-Chretien spectrograph; DB: Double Spectrograph; EF: ESO Faint Object Spectrograph and Camera (EFOSC-2); EM: ESO Multi-Mode Instrument (EMMI); GM: Gemini Multi-Object Spectrographs (GMOS); IM: Inamori Magellan Areal Camera and Spectrograph (IMACS); LD: Low Dispersion Survey Spectrograph (LDSS); MA: Magellan Echelle spectrograph (MagE); MS: Las Campanas Modular Spectrograph; WF: Wide Field Reimaging CCD Camera (WFCCD); Column 6: wavelength range covered; Column 7: spectral resolution in Å as estimated from arc-lamp lines; Column 8: total exposure time; Column 9: Airmass at the middle of the observation; Column 10: rms of the differences between synthetic and observed broadband magnitudes.

^a Spectrum uncorrected for telluric absorption (see Section 2.2).

^b Spectrum corrected to match photometry (see Section 2.2).

(This table is available in its entirety in a machine-readable form in the online journal. A portion is shown here for guidance regarding its form and content.)

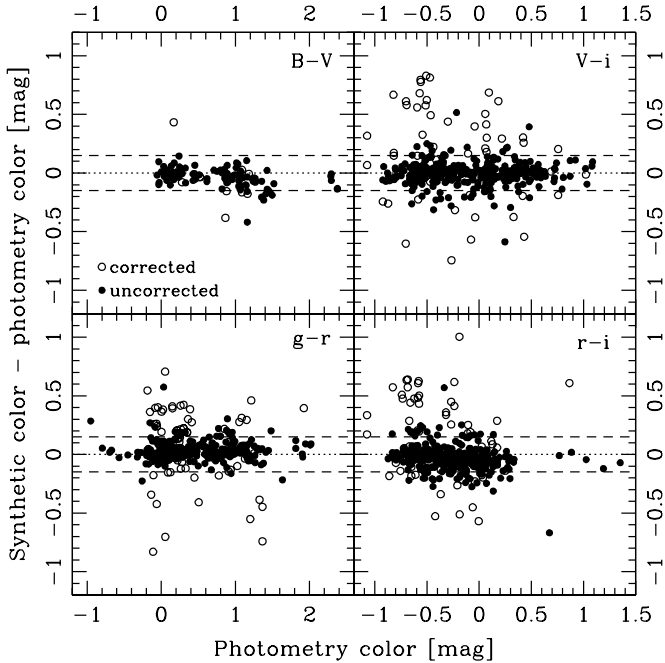


Figure 2. Comparison of synthetic and photometry colors for the CSP spectroscopic sample. Clockwise from the top-left panel, colors shown are $(B - V)$, $(V - i)$, $(g - r)$, and $(r - i)$. Open symbols indicate spectra that were subsequently corrected to match the photometry as described in Section 2.2. Filled symbols correspond to spectra that required no correction or that did not cover the minimum of three bandpasses to allow the correction. The dotted lines indicate zero deviation, and the dashed lines indicate ± 0.15 mag deviation.

on the Hale 200 inch Telescope at Palomar Observatory. In addition to this, 84 spectra of SN 2004dt (Altavilla et al. 2007), SN 2004eo (Pastorello et al. 2007), SN 2005bl (Taubenberger et al. 2008), SN 2005hj (Quimby et al. 2007), and SN 2006X (Wang et al. 2008; Yamanaka et al. 2009) were retrieved from The Online Supernova Spectrum Archive (SUSPECT, <http://suspect.nhn.ou.edu/~suspect/>). Near-maximum spectra of the SNe included in this work were added from the CfA Supernova Program and the BSNIP. This comprises 106 spectra from the CfA sample (Blondin et al. 2012), and 38 from the BSNIP sample (Silverman et al. 2012a). The SUSPECT, CfA, and BSNIP spectra are not listed in Table 2.

3. SPECTRAL MEASUREMENTS

Around maximum light, optical SN-Ia spectra present a strong continuum marked by P-Cygni lines characteristic of dense expanding material located around an emitting body. The most common ions producing such features are Fe II, Ca II, S II, Si II, Na I, Mg II, and O I. The distribution of the lines and the large Doppler broadening causes significant blending, particularly at blue wavelengths. For this reason, the actual continuum flux and the individual line profiles are difficult to determine.

In order to quantify the spectroscopic properties of SNe Ia, we have performed measurements on different spectral features that are identifiable during the evolution of the object around maximum light. These measurements are (1) line expansion velocities obtained from Doppler shifts of the absorption minima of several lines and (2) pseudo-equivalent widths of “absorptions” surrounded by local flux maxima.

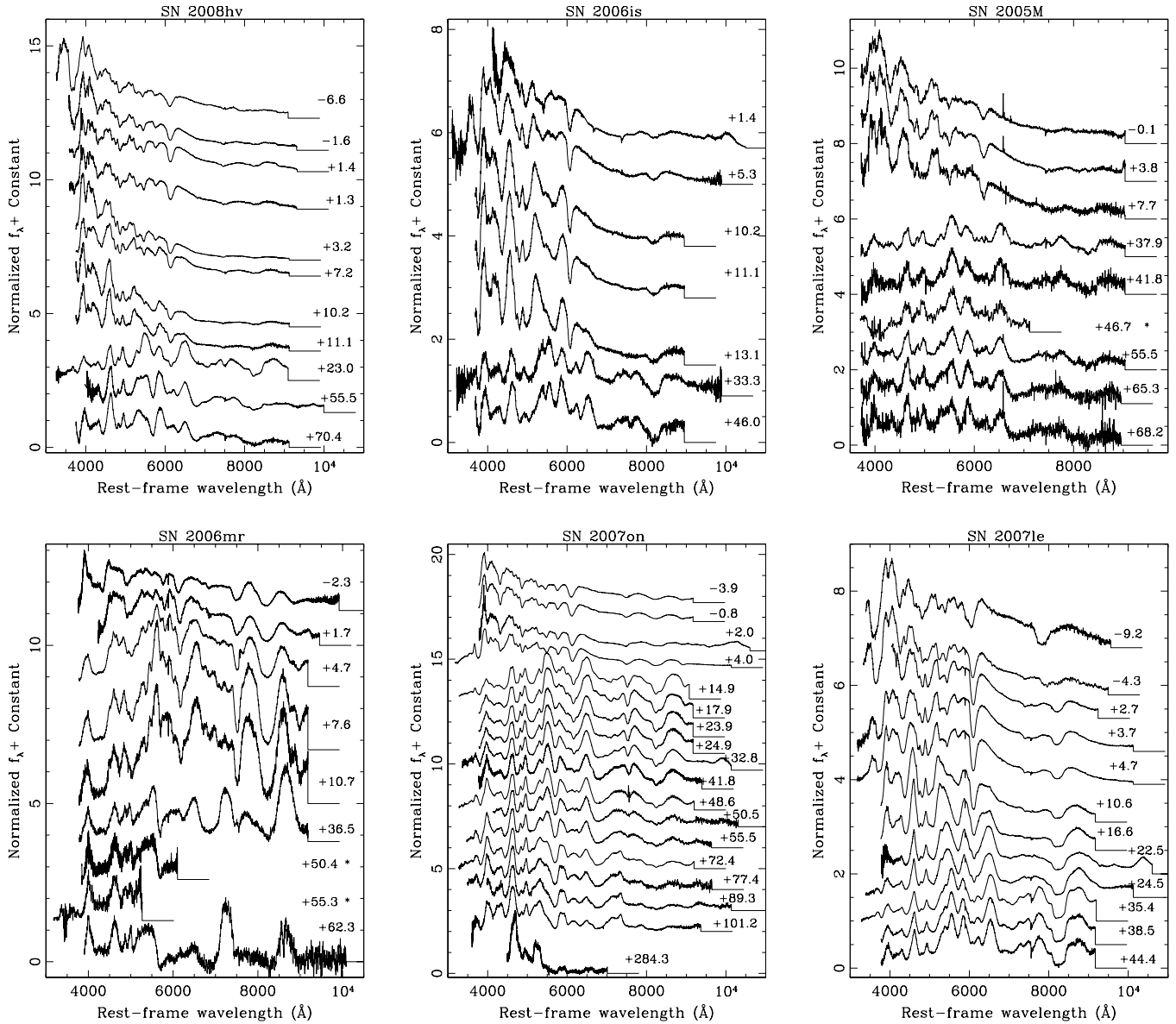


Figure 3. Examples of spectral time series obtained by the CSP. The spectra are shown in units of f_λ and have been normalized by the average of the flux in a common wavelength range. An arbitrary additive constant was applied to each spectrum for clarity. The zero flux level is shown by a horizontal line to the right of each spectrum. The labels on the right-hand side show the epoch of each spectrum in days with respect to B -band maximum light. Asterisks indicate spectra that were smoothed. Examples shown in this figure represent the different Branch subtypes (see Section 4): SNe 2008hv and 2006is are CN, SN 2005M is SS, SNe 2006mr and 2007on are CL (the former is eCL), and SN 2007le is BL. Similar plots for the complete sample of SNe presented in this paper will be made available along with the data on the CSP Web site.

(An extended version of this figure is available in the online journal.)

3.1. Line Expansion Velocities

The shift of the absorption minimum of a line with respect to the rest wavelength of the corresponding transition provides an estimate of the average expansion velocity of the material producing the absorption. Wavelength shifts can be converted to velocities via the Doppler formula. We adopted the relativistic Doppler formula (see Equation (6) of Blondin et al. 2006). Accurately measuring the absorption minimum is not always easy in the case of SNe because the large speed of the material broadens the lines and often makes them blend together. We have selected a number of multiplets which are the most easily identifiable and isolated in the spectra of SNe Ia around maximum light. For these, effective rest-frame wavelengths were computed based on air wavelengths and oscillator strengths given by the NIST Atomic Spectra Database (ver. 3.1.5; available

from <http://physics.nist.gov/asd3>). These ions and resulting effective wavelengths are as follows: Ca II H&K $\lambda 3945.02$ and the IR triplet $\lambda 8578.79$; Si II $\lambda 4129.78$ (4130), $\lambda 5971.89$ (5972), and $\lambda 6356.08$ (commonly referred to as 6355); S II $\lambda 5449.20$ (5449) and $\lambda 5622.46$ (5622), where numbers between parentheses will be used as line identifications in what follows. The O I $\lambda\lambda 7772, 7775$ doublet is commonly found in SN-Ia spectra. We have, however, not included it in this analysis because its absorption can be affected by residuals of the telluric A-band.

The observed line positions were derived via Gaussian fitting of the absorption minimum performed with the IRAF routine `splot`²⁰ after removing the redshift introduced by the

²⁰ IRAF is distributed by the National Optical Astronomy Observatory, which is operated by the Association of Universities for Research in Astronomy, Inc., under cooperative agreement with the National Science Foundation.

Table 3
Values of Velocity (km s^{-1}) at *B*-band Maximum Light, and $\text{Si II } \lambda 6355$ Velocity Decline (km s^{-1})

SN	$v(\text{Ca II H\&K})$	$v(\text{Si II } \lambda 4130)$	$v(\text{S II } \lambda 5449)$	$v(\text{S II } \lambda 5622)$	$v(\text{Si II } \lambda 5972)$	$v(\text{Si II } \lambda 6355)$	$v(\text{Ca II IR})$	$\Delta v_{20}(\text{Si})$
CN								
2004ey	16203 ± 1307	9640 ± 381	9327 ± 279	9238 ± 191	9942 ± 200	11204 ± 333
2005bo	11928 ± 788	9527 ± 153	8291 ± 336	8527 ± 118	10065 ± 202	10857 ± 291
2005el	12407 ± 41	9668 ± 46	8703 ± 43	8966 ± 29	10329 ± 182	11003 ± 51	...	1328 ± 294
2005hc	...	10292 ± 336	9071 ± 587	9835 ± 259	11038 ± 489	11163 ± 219
2005kc	...	10089 ± 352	8960 ± 429	8916 ± 93	9962 ± 217	10554 ± 239	...	707 ± 270
2005ki	...	10522 ± 738	10268 ± 0	9811 ± 92
2005ku	...	11334 ± 313	9793 ± 842	9972 ± 297	11783 ± 1592	12215 ± 697
2005na	...	9852 ± 114	10903 ± 525	10763 ± 62	...	608 ± 66
2006D	...	9684 ± 42	9026 ± 948	9216 ± 196	10389 ± 38	10867 ± 27	12467 ± 14	911 ± 154
2006ax	...	8726 ± 100	8360 ± 272	8375 ± 72	8897 ± 207	10170 ± 78	...	1190 ± 250

(This table is available in its entirety in a machine-readable form in the online journal. A portion is shown here for guidance regarding its form and content.)

host-galaxy recession velocity. Since the Gaussian function is generally not a good approximation of the complete absorption profile, the fits were restricted to the core of the lines. This way we were able to obtain the location of the absorption minimum in a reproducible way. In cases when the minimum presented a flat shape the Gaussian provided an approximation of the central position. Whenever there was a double profile, we found the location of both minima using two local Gaussians. In the following analysis we consider the velocity of the redder component (with lower velocity) whenever the line had a double minimum.

Measurement uncertainties, which are very much dependent on the width of the line, its signal-to-noise ratio (S/N), and spectral resolution, were estimated by performing repeated Gaussian fits around the originally measured value. The limits of the fitting regions on each side of the measured minimum were allowed to vary between 40 and 70 Å for the weakest lines ($\text{Si II } \lambda 4130$, $\text{S II } \lambda 5449$, and $\lambda 5622$), and between 40 and 100 Å for the rest of the lines. The limiting points of the fitting range were varied by three pixels between repetitions, which implies that the number of Gaussian fits was determined by the spectral sampling. The median absolute deviation (MAD) of all Gaussian minima was adopted as an estimate of the measurement uncertainty. In a conservative approach, we also compared the median central wavelength of all the Gaussian fits with the originally measured position derived from *splot*. In cases where these values differed by more than the computed MAD, we adopted the absolute value of the difference as the uncertainty.

In the following sections we will use values of expansion velocities at the time of *B*-band maximum light, as listed in Table 3. Since the observations very rarely coincided with that exact phase, we have derived such values using data obtained near maximum. In cases when there were several observations within one week before and after maximum, we performed low-order (first or second) polynomial fits. When only two observations encompassing maximum light were available, we interpolated to the time of maximum. If the observations did not encompass the time of maximum light, we allowed for an extrapolation if there was at least one measurement obtained in the range of $[-1, 1]$ day. Otherwise, we extrapolated any measurement obtained within four days from maximum using average slopes for the velocity evolution obtained for well-sampled SNe. These slopes are summarized in Table 4. If more than one such extrapolation was done for a given SN, then the results were combined using a weighted average.

We tested the robustness of the fits and interpolations to maximum light by repeating the calculations described above after removing data points from the best-observed SNe. Such tests confirmed that the derived velocities at maximum light are stable and that median deviations from the originally fit values are smaller than $\approx 300 \text{ km s}^{-1}$ for any number of data points down to two. In the end, we were able to obtain expansion velocities at maximum light for 78 of the SNe in our sample.

3.1.1. Velocity Decline Rate

Based on the work of Benetti et al. (2005), we have parameterized the rate of change of the $\text{Si II } \lambda 6355$ velocity after maximum light. Because of the relatively small number of velocity measurements obtained, to quantify this property we simply define $\Delta v_{20}(\text{Si})$ as the difference between the velocity at maximum light and that 20 days after (see a discussion on the difficulty of measuring velocity gradients in Blondin et al. 2012). In order to obtain the velocity at the latter epoch for a large sample of SNe, all available measurements obtained after seven days post-maximum were employed. Similarly to the method applied at maximum light, low-order polynomial (mostly linear) fits were used to derive the value at +20 days. When the data were too sparse to perform the fits but one observation was available between +17 and +23 days, an average slope of $-76 \pm 16 \text{ km s}^{-1} \text{ day}^{-1}$ obtained from 21 SNe with good coverage was employed to correct the measured velocity to the epoch of +20 days. $\Delta v_{20}(\text{Si})$ values are given in the last column of Table 3.

3.2. Pseudo-equivalent Widths

A convenient way of quantifying spectral properties of SNe Ia is to use *pseudo-equivalent widths* (pW) of apparent absorption features. The prefix “pseudo” is used to indicate that the reference “continuum” level adopted is generally not the actual continuum emission. We have measured pW for eight spectral features defined by Folatelli (2004) following the prescriptions given by Garavini et al. (2007). Examples of the pW features are shown in Figure 4. Feature definitions are summarized in Table 5. The first column gives the names that will be used throughout the text. The second column provides the main lines that are associated with each absorption feature near the time of maximum light. Although these line identifications are generally not unique and they vary with SN phase, we adopt them for the feature names to help the reader follow our analysis. Nevertheless, the association of features 1 and 8 with Ca II lines is persistent with phase, although near maximum light feature 1 may include a significant contribution of $\text{Si II } \lambda 3858$ (see

Table 4
Slopes of Expansion Velocity Evolution in Units of (km s^{-1} day $^{-1}$)

SNe Ia Subtype	Ca II H&K	n^a	Si II $\lambda 4130$	n^a	S II $\lambda 5449$	n^a	S II $\lambda 5622$	n^a	Si II $\lambda 5972$	n^a	Si II $\lambda 6355$	n^a	Ca II IR	n^a	Si II $\lambda 6355 (+20)^b$	n^a
Normal	-170 ± 111	6	-85 ± 16	12	-168 ± 10	12	-176 ± 11	12	-43 ± 26	12	-86 ± 14	13	-144 ± 141	2
BL	-255 ± 132	2	-254 ± 13^c	3	-218 ± 99	2	-250 ± 36^c	3	-416 ± 89^c	2
CL	-65 ± 91	2	-192 ± 96	3	-234 ± 264	3	-227 ± 15	3	-187 ± 59	6	-177 ± 20	6	24 ± 72	3
SS	-211 ± 110	2	-59 ± 17	4	-108 ± 28	6	-122 ± 16	6	10 ± 39	4	-42 ± 16	6
Normal+CL+SS	-151 ± 17^d	21	-169 ± 11^d	21	-67 ± 27^d	22	-96 ± 14^d	25	-14 ± 53^d	7
All	-156 ± 65^e	11	-96 ± 18^e	20	-155 ± 18	23	-177 ± 11	24	-77 ± 26	24	-112 ± 17	28	-21 ± 61	8	-77 ± 16^e	21

Notes.^a Number of SNe used in the average.^b Value of the slope between +7 and +25 days.^c Value applied to BL SNe Ia.^d Value applied to normal, BL, and SS SNe Ia.^e Value applied to all SNe Ia.

Table 5
Pseudo-equivalent Width Feature Definitions

Feature Name	Feature ID ^a	Blueward Limit Range (Å)	Redward Limit Range (Å)
<i>pW1</i> (Ca II H&K)	Ca II H&K	3500–3800	3900–4100
<i>pW2</i> (Si II 4130)	Si II $\lambda 4130$	3900–4000	4000–4150
<i>pW3</i> (Mg II)	Mg II, Fe II ^b	3900–4150	4450–4700
<i>pW4</i> (Fe II)	Fe II, Si II	4500–4700	5050–5550
<i>pW5</i> (S II W)	S II $\lambda\lambda 5449, 5622$	5150–5300	5500–5700
<i>pW6</i> (Si II 5972)	Si II $\lambda 5972$	5550–5700	5800–6000
<i>pW7</i> (Si II 6355)	Si II $\lambda 6355$	5800–6000	6200–6600
<i>pW8</i> (Ca II IR)	Ca II IR triplet	7500–8000	8200–8900

Notes.^a Spectral lines that contribute most to the observed absorption near maximum light.^b For CL SNe Ia, *pW3* (Mg II) is dominated by Ti II lines.

(Blondin et al. 2012). Features 3 and 4 are blends of lines due to Fe and intermediate-mass elements; for convenience, we call these “*pW3* (Mg II)” and “*pW4* (Fe II)” in reference to the ions that produce the strongest absorptions at maximum light. Feature 5 corresponds to the W-shaped absorption due to S II that is observed until about 10 days after maximum light. Finally, features 2, 6, and 7 are associated with Si II $\lambda 4130$, $\lambda 5972$, and $\lambda 6355$, respectively, although other ions also contribute. The former two features are weak and can only be identified until about ten days after maximum. Feature 7 is measured until approximately two months post-maximum, although its identification with Si II $\lambda 6355$ is only valid until day $\approx +10$. We have left aside the absorption around 7500 Å that is mostly due to the O I $\lambda\lambda 7772, 7775$ doublet because it lies near the telluric A-band absorption. Even though most of the spectra were corrected for telluric absorption, the residuals of such correction can be large enough to affect the measurement of the O I doublet.

Each *pW* measurement is obtained by defining a straight “continuum” level between two flux peaks and computing the integral of the spectrum flux relative to the continuum (with positive sign for simplicity). The flux peaks that define each feature are selected within a fixed spectral range so that the maximum allowed spectral range is spanned. Columns 3 and 4 of Table 5 provide the wavelength ranges allowed for the location of the flux peaks on each side of the eight features (see Garavini et al. 2007). Note that the definition of *pW3* (Mg II) permits it to cover the wavelength range of *pW2* (Si II 4130).

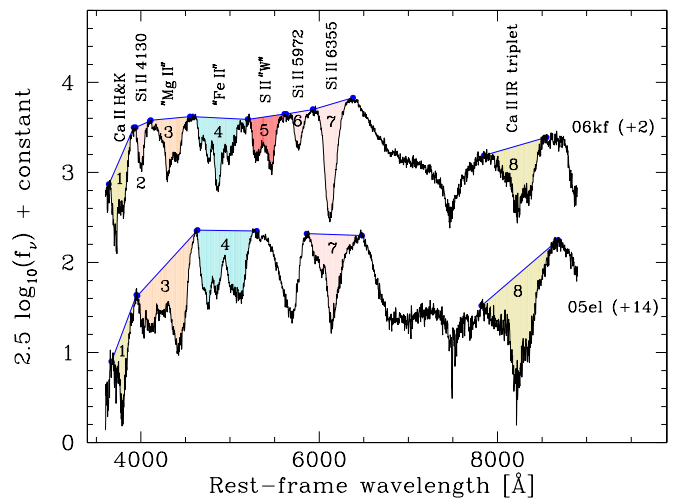


Figure 4. Examples of the definition of pseudo-equivalent features used in this paper (see also Garavini et al. 2007). Spectra of SN 2006kf at +2 days and SN 2005el at +14 days are shown with black lines. The data are shown as $\log(f_\nu)$ for clarity, and pseudo-continuum fits are shown as straight lines in the graph, although they are defined as such in f_λ space. The labels indicate feature numbers and adopted names (see Table 5). Eight features are defined until about ten days after maximum light (see top spectrum). At later times, fewer features are considered (see bottom spectrum). Note that feature 3 by definition can include the wavelength region of feature 2.

(A color version of this figure is available in the online journal.)

This generally happens at times after maximum light or for the subtype of CL SNe Ia (see Section 4), and in those cases feature 2 is not measured.

Because *pW* measurements involve an integration over a relatively wide wavelength region of ~ 100 Å, statistical uncertainties, in relative terms, are usually several times to one order of magnitude smaller than the uncertainties in the flux in a wavelength resolution bin. A significant contribution to the measurement uncertainty arises from systematic errors in the definition of the continuum points, variations in the flux peak levels due to an imprecise flux calibration, to contamination by host-galaxy light or even to noise. Most of our spectra have high signal-to-noise ratios ($S/N \gtrsim 30$ per 10 Å bins for over 90% of the spectra), so we have focused on other possible sources of systematic error. In our measurement procedure we have included a contribution to the uncertainty estimated by randomly varying the regions used for the continuum fit and for the integration (see Garavini et al. 2007).

Table 6
Values of pW (Å) at B -band Maximum Light

SN	$pW1$ (Ca II H&K)	$pW2$ (Si II 4130)	$pW3$ (Mg II)	$pW4$ (Fe II)	$pW5$ (S II W)	$pW6$ (Si II 5972)	$pW7$ (Si II 6355)	$pW8$ (Ca II IR)
CN								
2004ey	107.2 ± 5.3	13.6 ± 1.5	96.8 ± 1.5	129.9 ± 3.2	91.1 ± 3.3	14.2 ± 1.1	99.7 ± 3.5	65.0 ± 16.5
2005bo	...	16.8 ± 1.6	85.2 ± 3.9	134.1 ± 5.3	80.5 ± 2.8	23.2 ± 1.9	99.2 ± 1.8	158.8 ± 5.9
2005el	110.7 ± 1.8	20.6 ± 0.5	82.4 ± 5.8	112.9 ± 3.9	82.1 ± 1.2	20.5 ± 1.5	93.8 ± 1.7	130.1 ± 5.2
2005hc	...	10.3 ± 5.2	102.0 ± 5.2	125.1 ± 1.1	89.3 ± 3.8	18.3 ± 1.5	84.3 ± 1.6	...
2005kc	75.7 ± 2.4	130.7 ± 5.2	75.4 ± 1.3	25.8 ± 1.0	91.2 ± 1.1	...
2005ki	116.1 ± 1.6	20.9 ± 1.4	86.7 ± 1.4	110.8 ± 1.1	81.4 ± 0.6	22.3 ± 2.0	104.3 ± 0.5	86.0 ± 1.1
2005ku	...	11.5 ± 1.7	79.7 ± 8.1	91.0 ± 3.7	54.6 ± 1.4	12.1 ± 1.3	83.0 ± 3.0	...
2005na	87.7 ± 6.2	11.0 ± 0.5	116.7 ± 4.8	117.1 ± 15.4	89.6 ± 2.4	16.3 ± 2.0	78.7 ± 3.8	91.4 ± 22.5
2006D	96.8 ± 1.2	20.9 ± 0.2	182.9 ± 0.5	136.1 ± 5.3	87.3 ± 3.0	27.2 ± 2.3	98.5 ± 0.7	188.0 ± 9.7
2006ax	117.0 ± 1.0	13.4 ± 0.6	98.3 ± 1.8	118.9 ± 2.8	84.8 ± 2.5	12.1 ± 0.7	93.5 ± 2.0	131.6 ± 12.8

(This table is available in its entirety in a machine-readable form in the online journal. A portion is shown here for guidance regarding its form and content.)

Table 7
Slopes of pW Evolution around Maximum Light in Units of [Å day $^{-1}$]

SNe Ia Subtype	$pW1$ (Ca II H&K)	n^a	$pW2$ (Si II 4130)	n^a	$pW3$ (Mg II)	n^a	$pW4$ (Fe II)	n^a	$pW5$ (S II W)	n^a	$pW6$ (Si II 5972)	n^a	$pW7$ (Si II 6355)	n^a	$pW8$ (Ca II IR)	n^a
Normal	-5.4 ± 1.7	4	0.7 ± 0.1	11	2.5 ± 1.8	12	4.5 ± 0.6	13	0.9 ± 0.4	13	0.4 ± 0.1	13	1.5 ± 0.6	13	6.0 ± 1.1	11
BL	0.6 ± 2.3	3	6.1 ± 2.1	3	1.3 ± 1.7	3	0.0 ± 0.6	3	-0.2 ± 1.1	3	8.2 ± 3.8	2
CL	-0.6 ± 0.3	2	9.9 ± 0.5^b	5	8.0 ± 4.0	5	0.0 ± 1.4	4	1.1 ± 0.6	5	2.3 ± 1.4	5	3.6 ± 4.1	4
SS	0.3 ± 0.3	5	0.1 ± 0.5	7	3.7 ± 0.4	7	2.0 ± 0.6	7	0.9 ± 0.2	7	2.2 ± 0.2	6	8.2 ± 3.1	7
Normal+BL+SS	1.8 ± 1.1^c	22
All ^d	-3.6 ± 1.7	7	0.3 ± 0.2	19	3.4 ± 1.3	27	5.1 ± 0.6	28	1.1 ± 0.3	27	0.6 ± 0.1	28	1.4 ± 0.4	27	6.6 ± 1.0	24

Notes.

^a Number of SNe used in the average.

^b Value applied to CL SNe Ia.

^c Value applied to normal, BL, and SS SNe Ia.

^d Values applied to all SNe, except in the case of $pW3$ as indicated below.

The effect of reddening is to smoothly modify the shape of the continuum and thus its slope around the absorption features. Nordin et al. (2011a) find that this effect reduces the pW of some features, with a magnitude of $<5\%$, for $E(B - V) < 0.3$ mag, and assuming the reddening law of Cardelli et al. (1989) with $R_V = 1.7$. Garavini et al. (2007) find similar results adopting a law with $R_V = 3.1$. To avoid this possible systematic error, we corrected the spectra of SNe with $E(B - V) > 0.3$ mag using the same reddening law and $R_V = 1.7$ (this choice of R_V is supported by the results of Section 5.3 and those of, e.g., Folatelli et al. 2010; Foley & Kasen 2011; Mandel et al. 2011).

Contamination by the host galaxy adds flux to the continuum and therefore produces systematically lower pW . Host-galaxy contamination is not important in our sample because most of the SNe are nearby and isolated from the bright regions of their hosts. As explained in Section 2.2, special care was taken to subtract the underlying emission from the host galaxies, and synthetic photometry from the resulting spectra was compared with broadband photometry in order to check the quality of the subtraction. For most of the spectra, the rms of the differences between synthetic and observed photometry was <0.1 mag (see Table 2), which indicates low degrees of contamination. Garavini et al. (2007) estimated roughly 10% decrease in pW for every 10% of contamination from host-galaxy light in the observed flux. Based on this, the effect of contamination is negligible for most of the spectra in the present sample.

In a similar way as was done for the line expansion velocities (Section 3.1), we derived pW values at B -band maximum light. Table 6 lists these values for 78 SNe. When several

measurements were available within one week before and after the time of maximum, a smooth polynomial fit was used. If only two data points were obtained encompassing maximum light within -4 and $+4$ days, then an interpolation was performed. In a few cases, only data before or after maximum were available within $[-7, +7]$ days. In those cases, an extrapolation was allowed if the closest point to maximum light was not farther than one day. For SNe which only had one measurement in the range $[-4, +4]$ days or when measurements in that range did not encompass maximum light, average slopes determined from the best observed SNe were used for correcting the pW value to the time of maximum light. Table 7 provides the average pW slopes used for this purpose (see Section 4 for a detailed definition of SN-Ia subtypes). Similarly to the velocity fits, we performed tests by removing data points from the best-observed SNe and found that the resulting values at maximum light are robust. Median deviations were estimated to be within 5 Å for all pW parameters.

3.3. Comparison with CfA and BSNIP Data

Blondin et al. (2012) published spectroscopic measurements of line velocities and pseudo-equivalent widths for an expanded sample of SNe Ia collected by the Centre for Astrophysics (CfA) Supernova Program (see their Table 4). We compared the measurements for 37 objects in common with our sample. Figure 5 shows the comparison of $pW6$ (Si II 5972), $pW7$ (Si II 6355), and v (Si II 6355), all evaluated at maximum light. We can see that in general there is a good agreement in the

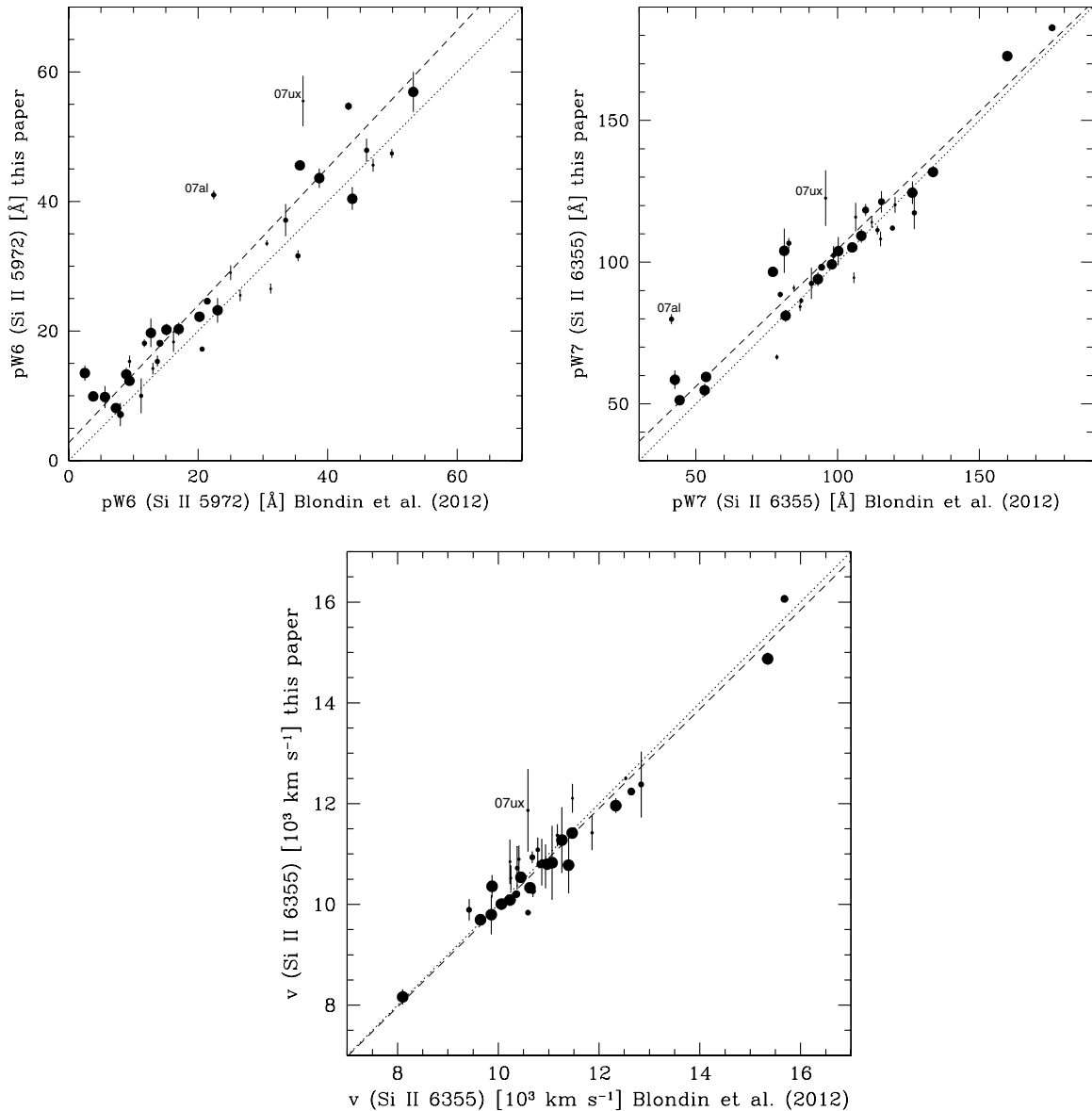


Figure 5. Comparison of $pW6$ ($\text{Si II } 5972\text{\AA}$) (top left), $pW7$ ($\text{Si II } 6355\text{\AA}$) (top right), and v ($\text{Si II } 6355$) (bottom) for the same SNe observed by the CSP and the CfA Supernova Program (Blondin et al. 2012). Symbol sizes are inversely proportional to the time interval of the CfA spectra relative to B -band maximum light. The dotted lines indicate the one-to-one relation. The dashed lines show fits to the data points.

pW values. A systematic shift of $\approx 3 \pm 2 \text{\AA}$ is observed which indicates that the measurements of Blondin et al. (2012) are slightly smaller than our own. Straight-line fits to the pW measurements yield $pW6(\text{Si II } 5972)_{\text{CSP}} = 2.73(\pm 0.53) + 1.06(\pm 0.02) \times pW6(\text{Si II } 5972)_{\text{CfA}}$ and $pW7(\text{Si II } 6355)_{\text{CSP}} = 7.8(\pm 1.4) + 0.97(\pm 0.01) \times pW7(\text{Si II } 6355)_{\text{CfA}}$. The differences may be due to a larger incidence of host-galaxy contamination in the CfA spectra, or by a systematically different measurement procedure. The largest discrepancies are found for SNe 2007al and 2007ux. The CfA spectra of these objects show systematically redder continua as compared with the CSP spectra at similar epochs. This may be due to host-galaxy contamination which produces a systematic decrease in the pW of both Si II lines.

In the case of Si II velocities, the agreement is very good. A weighted average of the differences yields $\Delta v \equiv v_{\text{CfA}} - v_{\text{CSP}} = 78 \pm 63 \text{ km s}^{-1}$. A fit to the velocity measurements, considering uncertainties in both axes, yields $v_{\text{CSP}} = 90(\pm 260) +$

$0.99(\pm 0.02) \times v_{\text{CfA}} \text{ km s}^{-1}$. The absolute values of the differences are $< 600 \text{ km s}^{-1}$ for all SNe except for SNe 2005bl and 2007ux, for which we get velocities at maximum that are $\approx 750 \text{ km s}^{-1}$ lower and $\approx 1300 \text{ km s}^{-1}$ higher than those measured by the CfA team, respectively. These differences can be explained by the fact that the CfA spectra were obtained at -2.9 days and 5.8 days relative to maximum light for each SN, respectively. In fact, when we compare measurements from spectra at similar epochs for these SNe, in all cases the velocities agree within the uncertainties with those of the CfA.

BSNIP recently published a series of papers with their SN-Ia spectroscopic sample. Silverman et al. (2012c) presented spectroscopic measurements of 432 near-maximum spectra of 261 SNe Ia. Among those SNe, 52 objects are in common with our sample. We used the data in their Tables B1–B9 to compare velocity and pW measurements. We compared each of their measurements with an average of all available measurements of the same SN from spectra obtained by the CSP within four days

of the BSNIP spectrum. This was done for all eight of our pW features and for the velocities of Si II, Ca II, and v (S II 5622) (the latter corresponds to their S II “W” velocity.) The agreement for the velocities is good, with no significant deviations between the two samples. However, the weighted rms scatter of the differences was $\approx 500 \text{ km s}^{-1}$ for the Si II and S II lines, and $\approx 1000 \text{ km s}^{-1}$ for the Ca II lines. These dispersions indicate that assuming flat uncertainties of 100 km s^{-1} for individual measurements may be an underestimation.

For the pW measurements, the agreement is again good within the quoted uncertainties for $pW1$ (Ca II H&K), $pW2$ (Si II 4130), $pW5$ (S II W), $pW6$ (Si II 5972), and $pW8$ (Ca II IR). The weighted dispersion of the differences is 2–3 Å for the weak Si II features, and 15 Å and 33 Å for $pW1$ (Ca II H&K) and $pW8$ (Ca II IR), respectively. These values provide an indication of the actual measurement uncertainties. The relative dispersion of $pW5$ (S II W) values is large (about 15 Å) and may be due to differences in the continuum-fitting regions that define the pW measurements (compare Table 5 in this paper with Table 1 of Silverman et al. 2012c). Non-negligible systematic differences of 3σ – 4σ appear in the cases of $pW3$ (Mg II), $pW4$ (Fe II), and $pW7$ (Si II 6355). Our pW are larger on average than those of Silverman et al. (2012c) by $18.5 \pm 4.7 \text{ Å}$ for $pW3$ (Mg II), $15.5 \pm 4.3 \text{ Å}$ for $pW4$ (Fe II), and $7.0 \pm 2.4 \text{ Å}$ for $pW7$ (Si II 6355), based on 28, 37, and 52 measurements, respectively. In the first two cases, we suspect that the discrepancy arises from differences in the regions of continuum fitting (our regions are wider and may thus lead to larger pW values). Although the discrepancy in $pW7$ (Si II 6355) is smaller, we could not find a clear explanation for it. Since this parameter measured at maximum light is useful for characterizing SNe Ia as will be shown in the following sections, we performed the comparison with measurements obtained only within one week of maximum and found a still-significant, although smaller, discrepancy of $5.6 \pm 2.1 \text{ Å}$ among 30 measurements.

4. SPECTROSCOPIC DIVERSITY

In spite of the relative spectroscopic homogeneity among SNe Ia as compared with other SN types, some variations exist that are most notable in spectra obtained before or around the time of maximum light. These variations are quantified here in terms of the spectroscopic measurements described in the previous section. This study serves to distinguish different subtypes of SNe Ia and to detect peculiar cases. In Figure 6, we present the $pW6$ (Si II 5972)– $pW7$ (Si II 6355) diagram, which was introduced by Branch et al. (2006) to identify the subtypes of CN, BL, SS, and CL SNe Ia. Recent versions of this diagram have been presented by Blondin et al. (2012) for the CfA sample, and by Silverman et al. (2012c) for the BSNIP sample. In a way this scheme is a summary of the spectroscopic diversity discovered thus far: a decreasing temperature sequence from 1991T-like to normal and 1991bg-like SNe (SS–CN–CL), plus the high-velocity SNe (BL). We note that the SS group includes 2002cx-like and 1991T-like SNe which have been suggested to be physically distinct types of objects, with the spectroscopic differences being most evident in the expansion velocities (Li et al. 2003; Branch et al. 2004; Phillips et al. 2007).

Blondin et al. (2012) presented the classification of several hundred SNe observed by the CfA Supernova Program in the scheme of Branch et al. (2006). To facilitate comparison with this work, we adopt the following criteria to define the different

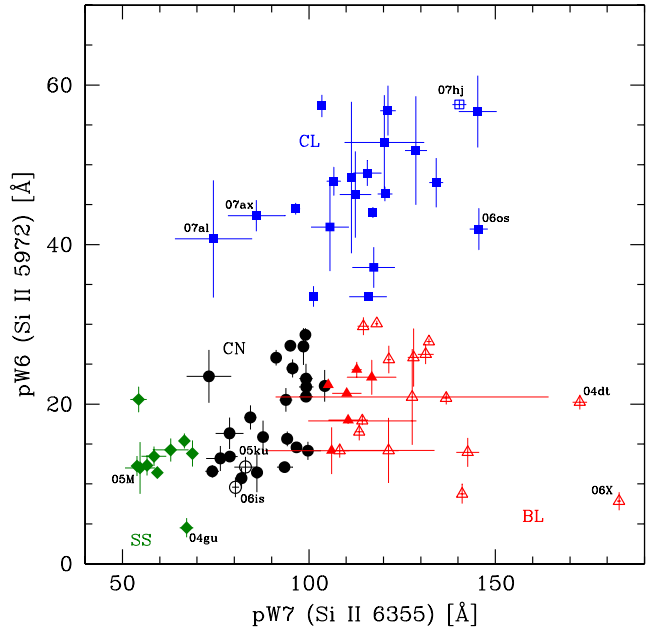


Figure 6. Subtypes of SNe Ia as defined by Branch et al. (2006; see also Section 4) can be identified in the diagram of $pW6$ (Si II 5972) vs. $pW7$ (Si II 6355). Core normal (CN, black circles); shallow silicon (SS, green diamonds); broad line (BL, red triangles); and cool (CL, blue squares) subtypes are distinguished based on a larger sample presented by Blondin et al. (2012). Open symbols indicate SNe with v (Si II 6355) $> 12,000 \text{ km s}^{-1}$ at maximum light, that is HV objects (Wang et al. 2009).

(A color version of this figure is available in the online journal.)

subclasses, which are very similar to those used by Blondin et al. (2012):

1. CL SNe: $pW6$ (Si II 5972) $> 30 \text{ Å}$,
2. BL SNe: $pW7$ (Si II 6355) $> 105 \text{ Å}$ and $pW6$ (Si II 5972) $< 30 \text{ Å}$,
3. SS SNe: $pW7$ (Si II 6355) $< 70 \text{ Å}$,
4. CN SNe: $70 \leq pW7$ (Si II 6355) $\leq 105 \text{ Å}$ and $pW6$ (Si II 5972) $\leq 30 \text{ Å}$.

As this scheme is based on $pW6$ (Si II 5972) and $pW7$ (Si II 6355) at maximum light, we were able to classify 78 of the SNe Ia in our sample in the following groups: 25 CN, 21 CL, 22 BL, and 10 SS objects. The classification of each SN is given, when available, in Table 1.

The divisions given above are somewhat arbitrary and, as noted by Branch et al. (2009), there is no evident discontinuity in the overall spectroscopic properties as we move along the $pW6$ (Si II 5972)– $pW7$ (Si II 6355) diagram. If we compare the fraction of objects within each subtype with the sample of Blondin et al. (2012; see their Table 4 which includes the CfA sample and ten previously published SNe Ia), we obtain similar distributions. There are 32% (38%) CN, 28% (30%) BL, 27% (18%) CL, and 13% (14%) SS SNe in the CSP (CfA) sample. All these fractions are within the statistical uncertainties of the limited samples. If anything, the CSP sample contains relatively fewer CN and BL SNe and more CL objects. Comparing our classification with that of Silverman et al. (2012c) for 12 SNe in common, we find agreement except for SN 2006D, which they classify as BL and we include in the CN group. This is explained by a slightly different boundary between the CN and BL subclasses in $pW7$ (Si II 6355) as adopted by Silverman et al. (2012c).

Figure 7 shows composite spectra at maximum light for each Branch subtype (cf. Figure 11 of Blondin et al. 2012). The

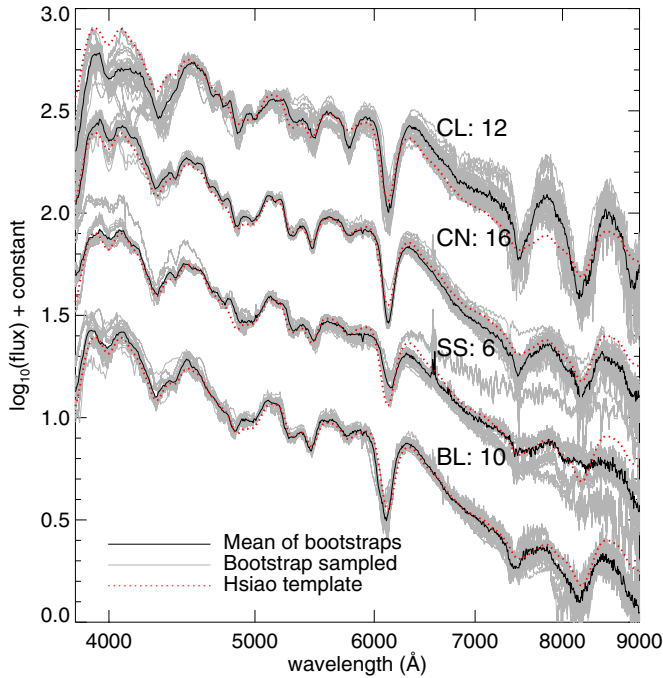


Figure 7. Composite spectra at maximum light for different Branch subtypes. The labels above each spectrum indicate the subtype and the number of SNe involved in the calculation for that subtype. Each bootstrap combination is shown with a gray line. The black lines show the mean of all bootstrap combinations. The red dotted lines show the template spectrum of normal SNe Ia at maximum light as computed by Hsiao et al. (2007).

(A color version of this figure is available in the online journal.)

composite spectra were constructed using CSP observations obtained in the range of $[-4, +4]$ days with respect to maximum light. We ensured that a SN only contributed one spectrum in a given bin, such that the composite spectra are not dominated by a few SNe with many time-series observations. The calculations involved 16 CN, 12 CL, 6 SS, and 10 BL SNe. The spectra were all converted to the rest frame and corrected by extinction in the Milky Way and the host galaxy. Extinction corrections were done using the law of Cardelli et al. (1989) and assuming $R_V = 3.1$ for the Milky Way component and the host galaxy component when $E(B - V)_{\text{Host}} < 0.3$ mag, and $R_V = 1.7$ for the host galaxy component when $E(B - V)_{\text{Host}} > 0.3$ mag (see Folatelli et al. 2010; Foley & Kasen 2011; Mandel et al. 2011). The composite spectra were computed using a bootstrapping algorithm. For each Branch subtype we constructed repeated realizations of the average spectrum by randomly selecting spectra from the available sample. In each realization the resampling was performed with replacement, so a single spectrum could enter more than once on average. The bootstrap procedure was repeated 100 times for each Branch subtype. Each bootstrap mean is plotted in the figure as a gray line. The mean of all individual realizations is plotted as a black line. As opposed to Blondin et al. (2012), we have not normalized the spectra by a pseudo-continuum function, and thus we can see the *actual* differences in color.

As pointed out by Blondin et al. (2012), the CN group shows the highest degree of homogeneity. In general, the largest dispersion is seen blueward of 4500 \AA . This is most notable in the BL, SS, and CL SNe. Some of this scatter is probably due to sampling issues or inaccurate corrections for host-galaxy extinction that, as we show in Section 5, affects more the BL and SS groups. The dispersion in the SS subtype can in part be due to

the small number of spectra used in the combination. However, part of the differences in the blue range of the spectrum are likely due to intrinsic differences in line strengths. This is most likely the case for the CL SNe whose spectra at these wavelengths are sensitive to small differences in effective temperature (Nugent et al. 1995). As we explain in Section 5.4, most of the CL SNe can be considered to have suffered little reddening by dust. This suggests that the differences in the blue part of the spectrum among CL SNe are mostly of intrinsic origin.

It is interesting to note that the composite spectra of CN, SS, and BL subtypes show a double-component Ca II IR triplet absorption. For CL SNe instead, the strong absorption appears to arise from a single component. In the cases of CN and BL SNe, the profile is dominated by a component at $11,000\text{--}12,000\text{ km s}^{-1}$. A shoulder on the blue wing of the absorption profile is seen at $18,000\text{--}20,000\text{ km s}^{-1}$ that can be associated with a high-velocity feature (HVF). The same velocity components are seen in SS SNe, although the absorption is weaker than in the previous cases. Such HVFs of Ca II are commonly detected in pre-maximum spectra of SNe Ia. There have been claims that HVFs are ubiquitous to this type of SNe (Mazzali et al. 2005). The composite spectra presented here agree with such a picture. Unfortunately, the wavelength coverage in the blue part of the spectrum is not long enough to allow a study of the Ca II H&K absorption profiles. The Ca II IR triplet is well covered by a large fraction of our spectra and, as opposed to Ca II H&K, it is conveniently isolated from other strong lines.²¹ However, on this part of the spectrum the continuum flux is low and the spectrum is affected by sky emission and instrumental fringing, which complicates a detailed analysis of the line profile. In Section 5.1, we will further study the variation of strength and shape of the Ca II IR triplet feature.

It can also be noted from Figure 7 that SS objects most clearly show the Na I D absorption at the redshift of the host galaxies. This absorption is also evident for CN SNe, but much less so for BL objects and almost negligible in the case of CL SNe. This again would indicate that SS objects suffered from larger extinction by dust associated with the gas that produced the Na I D absorptions. It is also worth pointing out the strong incidence of narrow emission lines of H α and [N II] among SS SNe. This suggests a closer relation of this subtype of SNe Ia with star forming, and therefore dusty, regions of their hosts. As seen in Section 5, SS SNe show the slowest decline rates and are more luminous than the average of SNe Ia. Therefore, the association of SS SNe with star-forming galaxies agrees with the findings of Hamuy et al. (1996), Howell (2001), Gallagher et al. (2008), Hicken et al. (2009), Sullivan et al. (2010), and Brandt et al. (2011), among others.

The left panel of Figure 8 shows near-maximum-light spectra of objects in the CL group sorted by decreasing $pW3(\text{Mg II})$. At the top of the figure some spectra show the strongest absorptions around 4300 \AA mostly due to the presence of strong Ti II lines. We call these “extreme cool” (eCL) SNe Ia. They are similar to the prototypically faint SN 1991bg. It is the eCL spectra that cause the large dispersion in the composite spectrum of the CL subtype as shown in Figure 7. We define eCL SNe by having $pW3(\text{Mg II}) > 220\text{ \AA}$, which in our sample includes SNe 2005bl, 2005ke, 2006bd, 2006mr, 2007ax, and 2009F. The absorption around 8300 \AA , due to the Ca II IR triplet, and the one near 7500 \AA , due to the O I $\lambda\lambda 7772, 7775$ doublet, are also stronger in CL objects than in CN ones. These Ca II IR

²¹ Although O I $\lambda 8446$ may appear in that part of the spectrum.

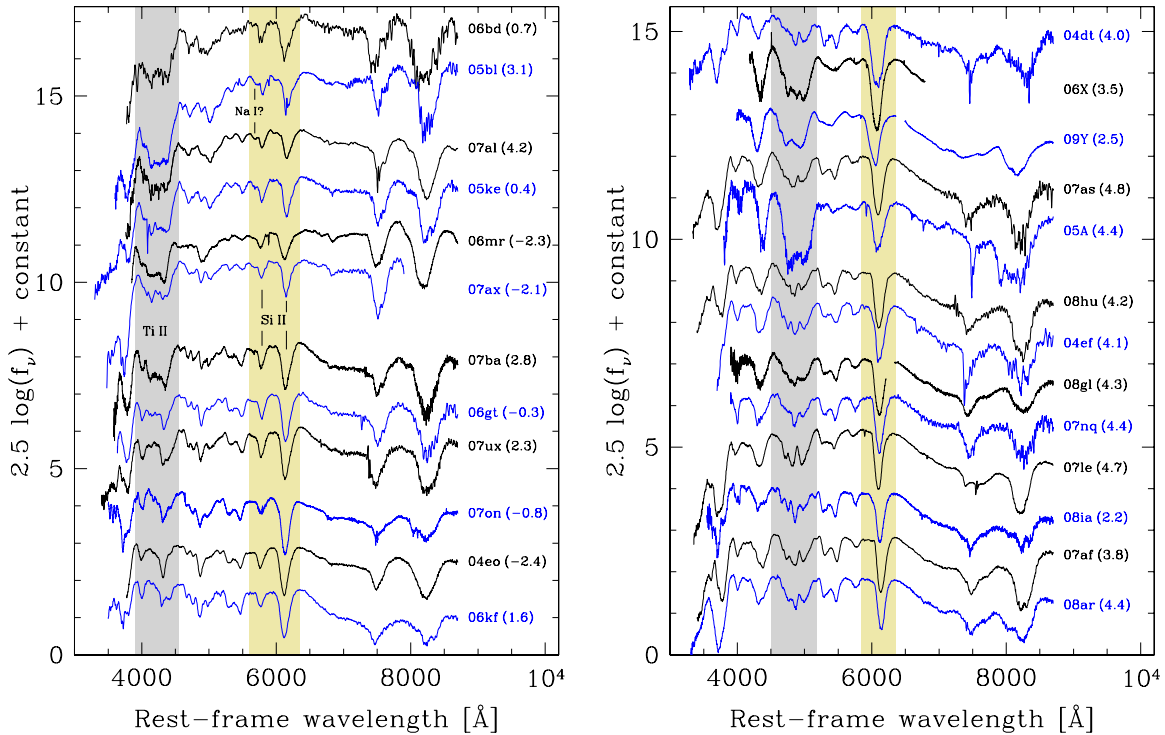


Figure 8. Left panel: spectra of CL and CN SNe Ia obtained near maximum light. The spectra are sorted in decreasing order of $pW3$ (Mg II). The labels on the right-hand side of each spectrum indicate the SN name and the epoch of the observation in rest-frame days relative to maximum light. The shaded areas mark the regions of $pW3$ (Mg II) (to the blue), and of $pW6$ (Si II 5972) and $pW7$ (Si II 6355) (near the center). The subgroup of extreme CL (eCL) SNe Ia (top six spectra) is distinguished by a strong trough around 4300 Å, which produces large values of $pW3$ (Mg II) > 220 Å. Right panel: spectra of BL SNe Ia and one CN object (SN 2008ar) obtained a few days after maximum light. The spectra are sorted in decreasing order of $pW7$ (Si II 6355). The shaded areas mark the regions of features 4 (to the blue) and 7 (near the center).

(A color version of this figure is available in the online journal.)

and O I absorptions roughly follow the decrease in strength between eCL and CL groups as observed for the ≈ 4300 Å absorption. The weighted average $pW8$ (Ca II IR) decreases from 325 ± 39 Å for the eCL SNe to 238 ± 26 Å for the rest of the CL objects. Interestingly, this behavior is not seen in the strength of the Si II $\lambda 5972$ line; the weighted average pW of this line is 48.6 ± 2.3 Å for eCL SNe and 45.9 ± 2.4 Å for the rest of the subclass. We note a difference between the eCL objects and the rest of the CL class in the profile of the absorption near 5800 Å associated in general with Si II $\lambda 5972$. For eCL objects this absorption has a double structure with a weak component on the blue side of the main absorption. This component tends to disappear as we move to CL SNe with smaller $pW3$ (Mg II). The weaker absorption can be attributed to the Na I D doublet that grows stronger at lower temperature.

The right panel of Figure 8 shows spectra of BL SNe Ia obtained a few days after maximum light, sorted by decreasing $pW7$ (Si II 6355). Some BL SNe show large absorption troughs centered at ≈ 4800 Å that are quantified by $pW4$ (Fe II), and a blended absorption due to Si II at around 5300 Å instead of the usual W-shaped feature. Based on these characteristics, SNe 2005A, 2006X, and 2009Y seem to form a separate group, even though SN 2009Y shows a shallower Si II velocity evolution as compared with SN 2006X [$\Delta v_{20}(\text{Si}) = 1710 \pm 260$ km s⁻¹ for SN 2009Y versus $\Delta v_{20}(\text{Si}) = 3660 \pm 110$ km s⁻¹ for SN 2006X]. We note that none of these three SNe are included in the composite BL spectrum shown in Figure 7. SN 2005A appears to be an extreme case, with very large absorption troughs. It shows by far the largest $pW4$ (Fe II) in our sample (306 ± 11 Å versus 241 ± 1 Å for the next highest,

SN 2006X), and the third largest $pW8$ (Ca II IR) = 401 ± 19 Å. Both SN 2005A and SN 2006X share photometric properties that, as presented by Folatelli et al. (2010), indicate the presence of a peculiar reddening law. At lower $pW7$ (Si II 6355) values, BL SNe continuously resemble CN objects, represented by the spectrum of SN 2008ar in the bottom of the figure. BL SNe with the largest Si II $\lambda 6355$ absorption strengths tend to show low $pW6$ (Si II 5972) (see Figure 6).

In terms of the classification introduced by Benetti et al. (2005; see also Hachinger et al. 2006), we see that their LVG group roughly includes the CN and SS subtypes, while their HVG and FAINT groups approximately correspond to the BL and CL types, respectively. Wang et al. (2009) set the division between HV and normal SNe Ia based on the velocity of Si II $\lambda 6355$ between -7 and $+7$ days relative to maximum light and comparing with the average of ten well observed “normal” SNe Ia. They considered any SN with silicon velocity above 3σ from the average in that epoch range to be HV. At the time of maximum light, we obtain an average of $\langle v(\text{Si II } 6355) \rangle = 10,800 \pm 400$ km s⁻¹, which closely matches the value of $10,700 \pm 400$ km s⁻¹ obtained by Wang et al. (2009). Wang et al. defined SNe with $v(\text{Si II } 6355) \gtrsim 11,800$ km s⁻¹ to be of type HV. With a larger sample, Blondin et al. (2012) place the division at $\approx 12,200$ km s⁻¹. Our average would set the limit at $\approx 12,000$ km s⁻¹. In the following we will consider HV SNe as those that have $v(\text{Si II } 6355) > 12,000$ km s⁻¹ at maximum light. Table 1 provides, when available, the classification of each SN according to the scheme of Wang et al. (2009). Nineteen of the SNe in our sample belong to the HV subclass. This number would change to 21 and 16 if we adopted the limits

of Wang et al. (2009) and Blondin et al. (2012), respectively. Most of the HV SNe in our sample (16 out of 19) belong to the BL subtype. Two of the other three (SNe 2005ku and 2006is) fall in the CN subtype, and one belongs to the CL group (SN 2007hj). Several objects appear near the velocity boundary and have measurement uncertainties that make the classification marginal. The objects that are within 1σ of the division are SNe 2006eq, 2006os, and 2008gl in the normal group, and SNe 2004ef, 2005ku, 2006ef, 2006ej, 2007nq, and 2008hu in the HV group. Because the distribution of velocities between normal and HV groups is continuous, small differences in the definition of the limit and small measurement uncertainties can lead to differences in the classification of some objects.

The fraction of 24% HV SNe in our sample is similar to that of 21% found by Blondin et al. (2012). In order to compare with the fraction of HV SNe in the sample of Wang et al. (2009), we consider only “normal” SNe Ia, i.e., we exclude from our sample 11 1991bg-like objects in the CL group, and 6 1991T-like objects in the SS group (see Table 1). We thus obtain a fraction of 31% HV SNe among 63 “normal” SNe Ia, which is similar to that of 35% (55 out of 158 SNe) found by Wang et al. (2009). If we adopt the limit of $11,800 \text{ km s}^{-1}$ to define the HV class, our fraction is 33% and the agreement is improved. The sample of Wang et al. (2009) has 33 SNe in common with ours. Among these, we have velocity measurements within one week from maximum light for 30 objects. Our classification agrees for all but two SNe, namely, SNe 2005am and 2006os. The only significantly discrepant classification is that of SN 2005am for which we measure $v(\text{Si II } 6355) = 12,160 \pm 70 \text{ km s}^{-1}$.

Comparing 28 SNe in common with the sample of Silverman et al. (2012c), our classifications in the scheme of Wang et al. agree for 23 objects. Two of the discrepant objects are so in terms of their silicon velocities at maximum: SNe 2005am and 2007bd, which are classified as HV in this work and as normal by Silverman et al. Other three objects, namely, SNe 2005M, 2005hj, and 2007S, are classified as normal by Silverman et al., while we place them in the 1991T-like category. For the latter two objects the difference may arise from the availability, in our case, of earlier spectra. The spectroscopic distinction between 1991T-like and normal SNe Ia tends to disappear after maximum light.

In Table 1, we also provide the classification that is derived from the SuperNova IDentification code (snid; Blondin & Tonry 2007). We used the spectra closest to maximum light in order to fit the best-match subtype. We employed version 5.0 of snid that does not distinguish between “1991T-like” and “1999aa-like.”

Based on the classifications above, in the following subsections we further study the spectral properties of the different subtypes of SNe Ia using the measurements described in Section 3.

4.1. Velocity and Pseudo-equivalent Width Evolution

Figure 9 shows the Si II $\lambda 6355$ line expansion velocity as a function of phase relative to B -band maximum light. Similar plots can be found in Figure 1 of Foley et al. (2011), Figure 15 of Blondin et al. (2012), and Figure 5 of Silverman et al. (2012c). We have shaded the 1σ region about the average of normal SNe Ia in the classification system of Wang et al. and overplotted the data of individual objects of different Branch subtypes. For normal SNe Ia, an almost constant decrease is seen between -10 and $+30$ days, going from about $12,000$ to $10,000 \text{ km s}^{-1}$. While for the non-HV CN SNe the dispersion at any given epoch is about 1000 km s^{-1} , for the complete

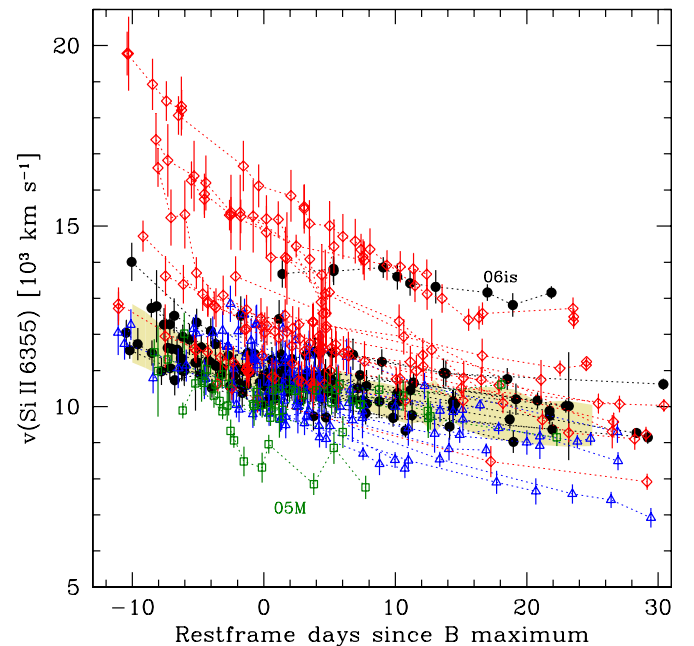


Figure 9. Expansion velocity as measured from the Si II $\lambda 6355$ absorption as a function of epoch with respect to B -band maximum light. The shaded band shows the average and 1σ dispersion of normal SNe Ia (see the text). Data of individual SNe are connected by dotted lines. Colors and symbols indicate different subtypes (see Section 4): CN, black circles; BL, red triangles; SS, green diamonds; and CL, blue squares.

(A color version of this figure is available in the online journal.)

sample this increases to over 5000 km s^{-1} . BL SNe show the largest velocities and span a range of 5000 – 7000 km s^{-1} depending on the epoch. They also show the largest velocity decline rates. CL SNe show similar velocities and dispersions than CN objects, and somewhat larger velocity gradients after maximum light. The evolution of SS SN velocities is rather flat. Among these, SN 2005M shows the lowest velocity in the whole sample, with $v(\text{Si II } 6355) \approx 8000 \text{ km s}^{-1}$ at maximum light, which is about 1500 km s^{-1} below the minimum value of the rest of the sample. The CN SN 2006is stands out by showing substantially higher Si II velocity at maximum light than the rest of the subtype, and shallower evolution than that of BL SNe with similar $v(\text{Si II } 6355)$. SNe 2005M and 2006is will be analyzed separately in Section 4.3.

Figure 10 shows the time evolution of the expansion velocities for the other two Si II lines, plus the S II and Ca II lines near maximum light (cf. Figure 4 of Silverman et al. 2012c). For the weak Si II and S II lines, the range of epochs shown is the interval when these features are clearly distinguishable in the spectra. A continuously declining behavior is observed for all SNe Ia, with the exception of $v(\text{Si II } 5972)$ after maximum light when the absorption may become contaminated by Na I D lines. The smallest velocities correspond to the weakest of these lines, namely Si II $\lambda 4130$, and the two S II absorptions. The relative behavior of different subtypes is similar to that of $v(\text{Si II } 6355)$ shown in Figure 9. Ca II velocities show the largest dispersions. Part of this may be due to the difficulty of measuring a velocity based on the absorption minimum of these very broad lines that, as pointed out by Foley et al. (2011) and Blondin et al. (2012), commonly present composite profiles. As will be shown in Section 4.2, the dispersion of Ca II velocities is not correlated with variations in the velocity of other species.

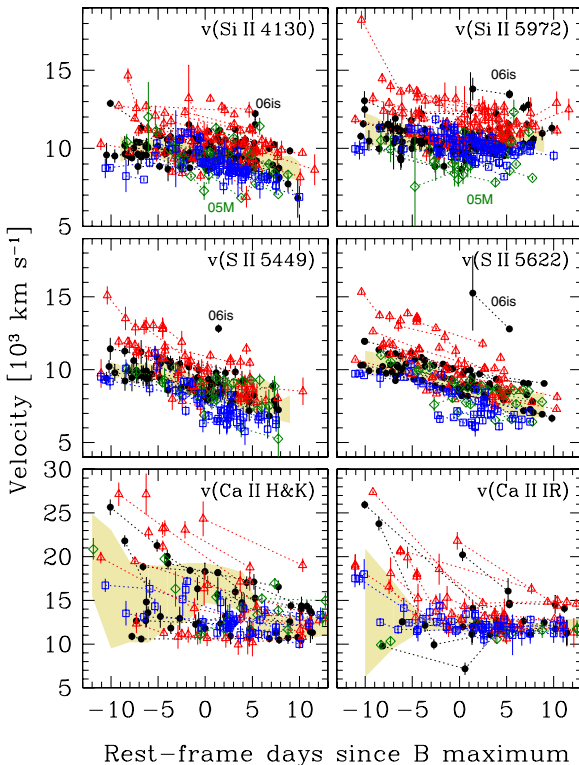


Figure 10. Expansion velocity evolution as measured from lines of Si II (top panels), S II (middle panels), and Ca II (bottom panels). The shaded bands show the average and 1σ dispersion of normal SNe Ia. Data of individual SNe are connected by dotted lines. The symbols are the same as in Figure 9.

(A color version of this figure is available in the online journal.)

Figure 11 shows the evolution of the eight pW parameters in the range of epochs where they can be measured (cf. Figures 7 and 8 of Silverman et al. 2012c). This extends to about +10 days for the weakest features, namely $pW2$ (Si II 4130), $pW5$ (S II W), and $pW6$ (Si II 5972). The rest of the features are defined until about two months after maximum light, although their association with specific species is no longer valid—with the possible exception of the Ca II absorptions. The evolution of $pW3$ (Mg II), $pW4$ (Fe II), $pW7$ (Si II 6355), and $pW8$ (Ca II IR) is roughly similar, i.e., a phase of nearly constant or slightly decreasing pW before maximum light, followed by an increase, and a subsequent flattening. The increase is the fastest for $pW3$ (Mg II), lasting for about 15 days, while it lasts for about 25 days for $pW4$ (Fe II), $pW7$ (Si II 6355), and $pW8$ (Ca II IR). $pW1$ (Ca II H&K), as opposed to all the other features, decreases almost continuously with time. For $pW5$ (S II W), there is a steep decrease that occurs after about day +5.

CL SNe are clearly distinguished by their higher than normal $pW6$ (Si II 5972) values. They also show large $pW2$ (Si II 4130), $pW3$ (Mg II), and $pW8$ (Ca II IR), and small $pW5$ (S II W) values. For eCL SNe, the increase of $pW3$ (Mg II) occurs earlier than for normal SNe Ia, even as early as −10 days. The subgroup of SS SNe shows relatively low values of pW for all features. The rise of $pW3$ (Mg II) for SS objects occurs at later times as compared with the rest of the subgroups.

4.2. Quantified Spectroscopic Properties

We now analyze the general spectroscopic properties of SNe Ia of different subtypes in a quantitative manner, concentrating on the interrelationships between velocity and pW mea-

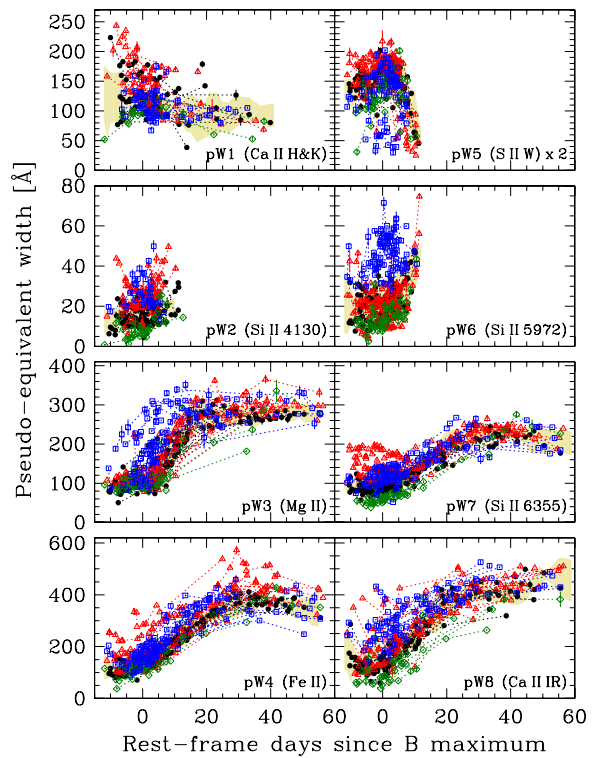


Figure 11. Pseudo-equivalent width evolution of the eight absorption features defined in this work (see Section 3.2 and Table 5). The shaded band shows the average and 1σ dispersion of normal SNe Ia. Data of individual SNe are connected by dotted lines. The symbols are the same as in Figure 9.

(A color version of this figure is available in the online journal.)

surements. Figure 12 shows the Pearson correlation coefficients, ρ , between all pairs of pW (left panel) and velocity (right panel) measurements at maximum light. In each panel, the upper left triangle corresponds to the complete sample of SNe with available measurements. The lower right triangles show the coefficients for objects with low silicon velocities [v (Si II 6355) < 12,000 km s^{−1}] and light-curve decline rates [$\Delta m_{15}(B)$ < 1.7 mag]. When all SNe Ia are considered, no strong correlations between pW parameters are found ($|\rho| < 0.75$). Some strong correlations stand out if we exclude HV and fast-declining SNe. Figure 13 shows the strongest of such correlations involving Si II features, and $pW8$ (Ca II IR) with $pW4$ (Fe II) and $pW7$ (Si II 6355). In general, the correlation coefficients between pW parameters for this restricted sample are positive. That is, the change in spectral line strengths from object to object tends to be in the same direction for all features. The exception to this is $pW1$ (Ca II H&K), which shows low and sometimes negative correlation coefficients with other pW parameters.

The right panel of Figure 12 shows that expansion velocities in general correlate positively with each other. The exceptions again involve Ca II lines whose velocities do not correlate with those of other features. This is likely due in part to difficulty of measuring a velocity from the absorption minimum of Ca II lines, as pointed out before and also stressed by Foley et al. (2011) and Blondin et al. (2012). Si II and S II line velocities correlate strongly, with coefficients near $\rho = 0.9$.

4.3. SNe 2005M and 2006is

In Section 4.1, we pointed out the existence of two objects whose expansion velocities, as measured with the Si II $\lambda 6355$ line, were atypical. These objects are SNe 2005M and 2006is.

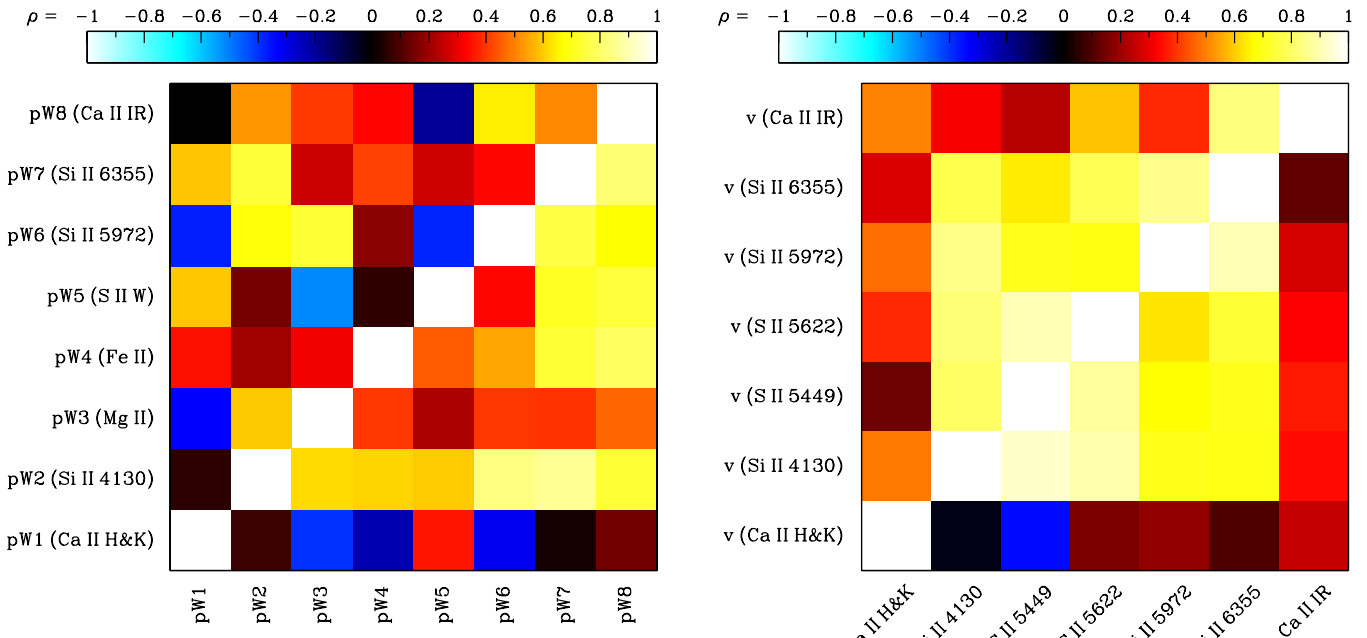


Figure 12. Correlation between pairs of pW parameters (left) and of expansion velocities (right) at maximum light. Colors indicate the Pearson correlation coefficient ρ . Lighter colors indicate larger degrees of correlation (or anti-correlation). In the upper left off-diagonal triangle all SNe are included. In the bottom right off-diagonal triangle, only objects with low expansion velocities [$v(\text{Si II } 6355) < 12,000 \text{ km s}^{-1}$] and light-curve decline rates [$\Delta m_{15}(B) < 1.7 \text{ mag}$] are considered. (A color version of this figure is available in the online journal.)

Their spectral time-series are shown in Figure 3. As can be seen in Figure 9, the former SN shows a lower Si II $\lambda 6355$ velocity than any other object in the sample, while SN 2006is shows a large velocity, compared with the rest of the CN sample, but shallower velocity evolution than typical HV SNe. The behavior of SN 2006is is similar to the one observed for SN 2009ig after maximum light (Foley et al. 2012).

The velocity shifts in the spectra of SNe 2005M and 2006is of the other Si II lines as well as S II $\lambda\lambda 5449, 5622$ with respect to the measurements for the rest of the sample are notable, though less pronounced (see Figure 10). However, the shape of the spectrum outside the Si II $\lambda 6355$ line is similar to that of other SNe of the corresponding subtype (SS for SN 2005M and CN for SN 2006is). We thus studied the distribution of different species in the ejecta in order to confirm the peculiar behavior of Si II and S II.

For this purpose, we fit the maximum-light spectra of SNe 2005M, 2006is, and 2009ig with the automated spectrum synthesis code SYNAPPS (Thomas et al. 2011b), derived from SNOW (Fisher 2000). SYNAPPS uses a highly parameterized, but fast spectrum synthesis technique, useful for identifying the ions that form the observed features. The best-fit synthetic spectra are compared with the observed spectra in Figure 14. The best-fit Si II and S II velocities for SN 2005M are 8100 km s^{-1} and 9400 km s^{-1} , respectively. These are substantially lower than the best-fit median velocity of $10,900 \text{ km s}^{-1}$ for the rest of the ion species, notably Mg II, Ca II and Fe III.

The best-fit Si II velocity for SN 2006is is $14,400 \text{ km s}^{-1}$. O I and S II also show high velocities at $13,300 \text{ km s}^{-1}$ and $12,300 \text{ km s}^{-1}$, respectively. The remainder of the ion species has a median velocity of $11,300 \text{ km s}^{-1}$. SN 2009ig has very similar spectral features as SN 2006is, and the best-fit velocities are also very similar. The best-fit Si II and S II velocities are $14,800 \text{ km s}^{-1}$ and $12,300 \text{ km s}^{-1}$, respectively, while the remainder of the ions has a median velocity of $11,500 \text{ km s}^{-1}$. Note that for SN 2006is and SN 2009ig, constraining the

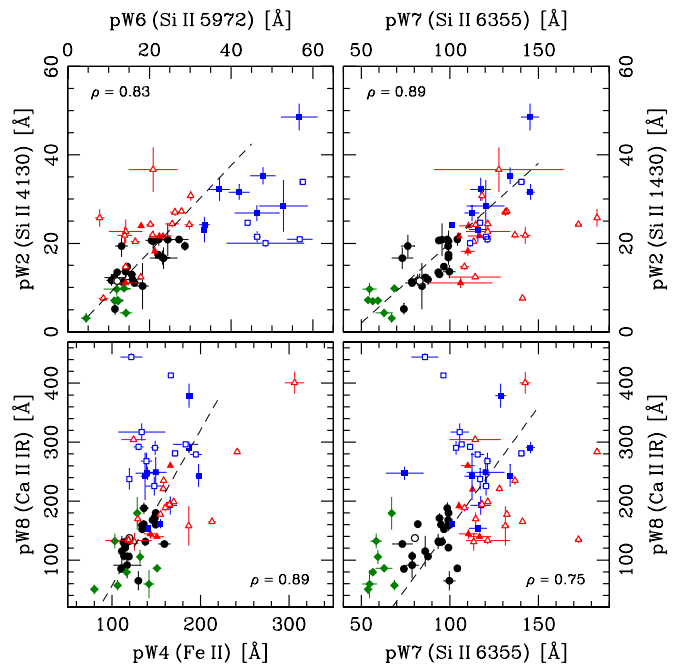


Figure 13. Examples of strong correlations between pW parameters. Different Branch subtypes are represented by black circles (CN), blue squares (CL), red triangles (BL), and green diamonds (SS). Filled symbols indicate SNe with low expansion velocities [$v(\text{Si II } 6355) < 12,000 \text{ km s}^{-1}$] and $\Delta m_{15}(B) < 1.7 \text{ mag}$, while the rest of the objects are shown with open symbols. The dashed lines show straight-line fits to the filled data points. Pearson correlation coefficients ρ are indicated in each panel.

(A color version of this figure is available in the online journal.)

velocities of all the ions to have the same value produces poor fits, especially for the Si II $\lambda 6355$ feature. Although for SN 2006is we adopted the redshift measured from our own deep spectrum of the host galaxy (see Section 2.1), the behavior

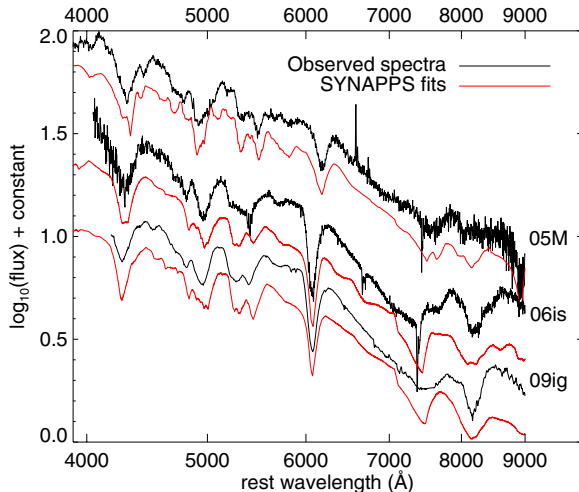


Figure 14. Spectra of SNe 2005M, 2006is, and 2009ig near maximum light (black lines) and corresponding SYNAPPS fits (red lines). See details in Section 4.3.

(A color version of this figure is available in the online journal.)

of line velocities cannot be attributed to an error in the redshift as it would equally affect all lines. Moreover, the close similarity with SN 2009ig provides further confidence that the measured redshift is accurate.

The light curves of SNe 2006is and 2009ig were both more slowly declining than average, with $\Delta m_{15}(B) = 0.80$ mag (Stritzinger et al. 2011) and 0.89 mag (Foley et al. 2012), respectively. Interestingly, SN 2005M was also a slow decliner with $\Delta m_{15}(B) = 0.82$ mag (Contreras et al. 2010). We performed SNooPy (Burns et al. 2011) fits to the *uBgVriYJH*²² light curves of SN 2006is and found that its V–NIR colors at maximum light are bluer by about 0.2–0.3 mag than those of unreddened SNe Ia of similar decline rate. On the other hand, optical colors of this SN are normal. The NIR light curves of SN 2006is show the double-peaked shape that is typical of SNe Ia, but their brightness relative to the optical bands appears to be low as compared with template SN Ia of similar $\Delta m_{15}(B)$. SNooPy fits to the *uBgVriYJH* light curves of SN 2005M do not reveal any obvious photometric peculiarities.

The existence of rare events like SNe 2005M and 2006is whose departure from the norm is mostly indicated by the peculiar velocities of certain intermediate-mass elements (IMEs) seems to indicate a new form of spectroscopic diversity, related to peculiar distribution of elements—notably Si II and S II which are the products of explosive oxygen burning—in the ejecta. An asymmetric explosion may have to be invoked in the case of SN 2005M to explain the presence of IMEs at lower velocity than that of Fe II. The cases of SNe 2006is and 2009ig may indicate the existence of an outer silicon-rich shell. Since these objects depart from the Si II $\lambda 6355$ velocity versus velocity gradient relation at maximum light (Foley et al. 2011), they do not seem to comply with the same geometrical picture of Maeda et al. (2010a) involving asymmetric explosions.

5. SPECTROSCOPIC AND PHOTOMETRIC PROPERTIES

Peak luminosities of SNe Ia, after correcting for host-galaxy extinction, can be calibrated based on a single parameter which measures the initial decline or “width” of the light

²² These are the bandpasses in the *natural* photometric system of the CSP (see Contreras et al. 2010).

curve (Phillips 1993; Phillips et al. 1999). Such calibration has been successfully employed to determine extragalactic distances and thereby cosmological parameters. From the viewpoint of spectroscopy, it has been observed that the strength of Si II features near maximum light follows this luminosity–decline rate correlation (Nugent et al. 1995; Hachinger et al. 2006; Silverman et al. 2012b). More recently, Bailey et al. (2009) and Blondin et al. (2011b) showed that some flux ratios can reduce the scatter in the luminosity calibration. However, other spectroscopic properties show a diversity which does not comply with this one-parameter description. Expansion velocities, for instance, show large variations which do not correlate with light-curve decline rate (Hatano et al. 2000; Benetti et al. 2005).

In this section, we present a quantitative comparison of spectroscopic and photometric properties of SNe Ia. Based on light-curve fits performed with the SNooPy code of Burns et al. (2011), we obtained *K*- and Galactic-extinction-corrected peak magnitudes in *B* and *V* bands (B_{\max} and V_{\max} , respectively), as well as decline rates, $\Delta m_{15}(B)$.²³ From the peak magnitudes, we computed *B–V pseudo*-colors at maximum light, ($B_{\max} - V_{\max}$). Adopting the calibrations of intrinsic color given in Equation (3) of Folatelli et al. (2010), we derived host-galaxy color excesses, $E(B - V)_{\text{Host}}$, as

$$\begin{aligned} E(B - V)_{\text{Host}} &= (B_{\max} - V_{\max}) + 0.016 \\ &\quad - 0.12 [\Delta m_{15}(B) - 1.1]. \end{aligned} \quad (1)$$

Note that the formula above is valid for SNe with $\Delta m_{15}(B) < 1.7$ mag. That is why we provide $E(B - V)_{\text{Host}}$ for only a small fraction of the CL objects.

Based on the color excesses, reddening-free *B*-band absolute peak magnitudes, M_B^0 , were obtained as

$$M_B^0 = B_{\max} - \mu - R_B \cdot E(B - V)_{\text{Host}}, \quad (2)$$

where μ is the distance modulus, and $R_B = 3.98$ is converted from a standard value of $R_V = 3.1$, as explained in Appendix B of Folatelli et al. (2010). This conversion assumes the dust extinction law introduced by Cardelli et al. (1989) and modified by O’Donnell (1994; hereafter, the CCM+O law), and a template SN-Ia spectrum at maximum light. To avoid errors in M_B^0 larger than ≈ 0.5 mag due to uncertainties in the value of R_B (which typical has been found in the literature to have values in the range of 3–4), we did not compute M_B^0 for SNe with $E(B - V)_{\text{Host}} > 0.5$ mag. Values of μ were derived from the redshift of the host galaxies using the second-order Hubble law given in Equation (5) of Folatelli et al. (2010), with $H_0 = 72 \text{ km s}^{-1} \text{ Mpc}^{-1}$, $\Omega_M = 0.28$, and $\Omega_\Lambda = 0.72$ (Spergel et al. 2007). To avoid large uncertainties in μ due to peculiar velocities, this was done only for SNe with $z_{\text{CMB}} > 0.01$.

We now study the properties of the photometric parameters involved in Equations (1) and (2) for the different spectroscopic subtypes. Figure 15 shows the distribution of $\Delta m_{15}(B)$ (left column), $E(B - V)_{\text{Host}}$ (middle column), and M_B^0 (right column) for the complete sample and the different subtypes of SNe Ia. Weighted averages of these quantities for each subtype are listed in Table 8. The $\Delta m_{15}(B)$ distribution of the complete sample has an average of $\langle \Delta m_{15}(B) \rangle = 1.16$ mag. SS and CL SNe clearly occupy the extremes of the $\Delta m_{15}(B)$ distribution, the former

²³ When the *B*-band light curve did not span a suitable range of time to directly measure $\Delta m_{15}(B)$ from the data points, we adopted the Δm_{15} fitting parameter of SNooPy (Burns et al. 2011). According to Burns et al., the actual $\Delta m_{15}(B)$ may be slightly different from Δm_{15} (see their Figure 6).

Table 8
Mean Photometric Properties for Different SNe Ia Subtypes

Sample	$\langle \Delta m_{15}(B) \rangle$ (mag)	N	$\langle (B_{\max} - V_{\max}) \rangle$ (mag)	N	$\langle E(B-V)_{\text{Host}} \rangle$ (mag)	N	$\langle M_B^0 \rangle$ (mag)	N	$\langle \Delta M_B \rangle$ (mag)	N
(1)	(2)	(3)	(4)	(5)	(6)	(7)	(8)	(9)	(10)	(11)
Complete	1.157 ± 0.072	93	0.141 ± 0.031	93	0.135 ± 0.024	77	-19.308 ± 0.049	68	0.005 ± 0.029	82
CN	1.092 ± 0.094	25	0.148 ± 0.060	25	0.133 ± 0.033	25	-19.379 ± 0.056	22	-0.028 ± 0.043	22
BL	1.070 ± 0.168	22	0.099 ± 0.060	22	0.153 ± 0.064	22	-19.250 ± 0.101	17	-0.062 ± 0.046	17
SS	0.888 ± 0.108	10	0.147 ± 0.046	10	0.168 ± 0.047	10	-19.564 ± 0.139	10	0.027 ± 0.098	10
CL	1.513 ± 0.123	20	0.224 ± 0.080	20	0.144 ± 0.063	5	-19.048 ± 0.136	5	0.008 ± 0.060	18
N	1.222 ± 0.076	37	0.145 ± 0.042	37	0.134 ± 0.027	34	-19.248 ± 0.049	29	0.007 ± 0.032	31
HV	1.005 ± 0.161	19	0.109 ± 0.068	19	0.163 ± 0.073	18	-19.339 ± 0.115	16	-0.079 ± 0.057	17

Notes. Weighted averages and standard deviations. Column 1: subsample used to average according to the classification schemes of Branch et al. and Wang et al. (see definitions in Section 4); Columns 2 and 3: light-curve decline rate and number of SNe used in calculation; Columns 4 and 5: pseudo-color at maximum light and number of SNe used in calculation; Columns 6 and 7: host-galaxy color excess and number of SNe used in calculation; Columns 8 and 9: reddening-free B -band absolute peak magnitude and number of SNe used in calculation; Columns 10 and 11: B -band Hubble residuals and number of SNe used in calculation.

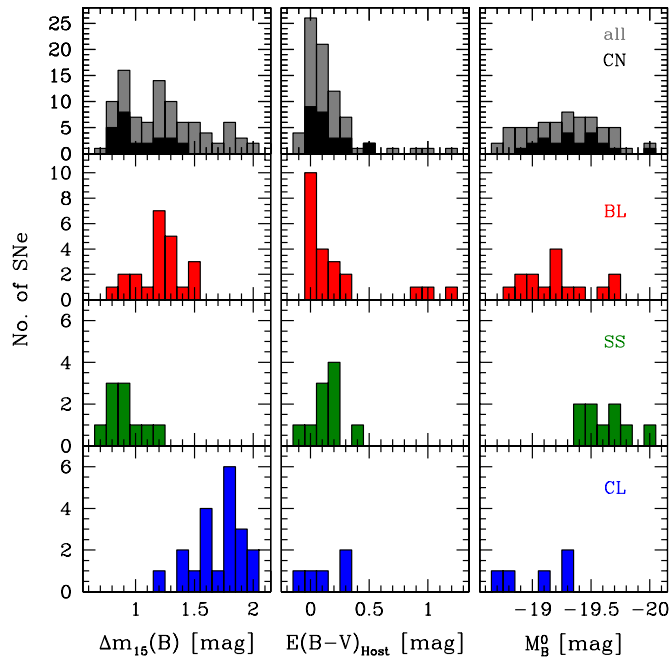


Figure 15. Distribution of light-curve decline rate $\Delta m_{15}(B)$ (left column), host-galaxy color excess $E(B-V)_{\text{Host}}$ (middle column), and reddening-free B -band absolute peak magnitudes M_B^0 for the complete sample (gray histograms) and for different SNe Ia subtypes (black, red, green, and blue histograms).

(A color version of this figure is available in the online journal.)

being slow decliners [$\langle \Delta m_{15}(B) \rangle_{\text{SS}} = 0.89 \pm 0.11$ mag] and the latter showing the fastest decline rates [$\langle \Delta m_{15}(B) \rangle_{\text{CL}} = 1.51 \pm 0.12$ mag]. CN and BL objects show similar averages, with a distribution that is slightly more skewed toward larger $\Delta m_{15}(B)$ in the case of BL SNe. From the middle column of the figure it is seen that SS SNe tend to have larger color excesses [$\langle E(B-V)_{\text{Host}} \rangle_{\text{SS}} = 0.17 \pm 0.05$ mag] than CN objects [$\langle E(B-V)_{\text{Host}} \rangle_{\text{CN}} = 0.13 \pm 0.03$ mag] and the bulk of BL SNe [$\langle E(B-V)_{\text{Host}} \rangle_{\text{BL}} = 0.15 \pm 0.06$ mag, but this value is reduced to 0.08 ± 0.02 mag when excluding three extremely reddened BL events: SNe 2005A, 2006X, and 2006br]. If confirmed with larger samples, this result points in the same direction as the evidence presented in Figure 7 of Section 4 for a closer association of SS SNe with gas-rich, dusty star-forming regions.

In terms of reddening-free B -band absolute peak magnitudes, again the extremes of the distribution are occupied by SS and

CL SNe (considering the few CL objects for which M_B^0 can be obtained). The same trend is seen as the one found by Blondin et al. (2012) of increasing M_B^0 (decreasing luminosity) as we move from SS to CN, BL, and finally to CL SNe. This reflects the sequence of $\Delta m_{15}(B)$ distributions. The weighted averages go from $\langle M_B^0 \rangle_{\text{SS}} = -19.56 \pm 0.14$ mag to $\langle M_B^0 \rangle_{\text{CN}} = -19.38 \pm 0.06$ mag, $\langle M_B^0 \rangle_{\text{BL}} = -19.25 \pm 0.10$ mag, and $\langle M_B^0 \rangle_{\text{CL}} = -19.05 \pm 0.14$ mag (the latter includes only five SNe).

5.1. Pseudo-EW and Light-curve Decline Rate

Figure 16 shows the degrees of correlation between pW parameters and light-curve decline rates, $\Delta m_{15}(B)$, considering both the pW measurements themselves and their ratios. The strongest correlation with $\Delta m_{15}(B)$ among single pW parameters is that of $pW6$ (Si II 5972), with a Pearson coefficient of $\rho = 0.86$ (both for the complete sample and when HV SNe are excluded). This relation was previously noted by Hachinger et al. (2006), and more recently by Silverman et al. (2012b). The resulting dispersion of $\Delta m_{15}(B)$ about the straight-line fit is of 0.14 mag. $pW2$ (Si II 4130) also depends strongly on $\Delta m_{15}(B)$. Its correlation coefficient of $\rho = 0.77$ for the complete sample increases to $\rho = 0.84$ if we restrict the sample to SNe with $\Delta m_{15}(B) < 1.7$ mag. Both cases of $pW2$ (Si II 4130) and $pW6$ (Si II 5972) are shown in Figure 17. In general, the correlations become stronger when we discard HV SNe Ia, as can be seen in the right panel of Figure 16.

Interestingly, $pW8$ (Ca II IR) also shows an increasing trend with $\Delta m_{15}(B)$ ($\rho = 0.6-0.7$). However, for a fixed $\Delta m_{15}(B)$ there is a wide range of $pW8$ (Ca II IR) values, with some SNe showing two or three times larger pW than their counterparts. On the contrary, the other Ca II feature, $pW1$ (Ca II H&K), shows no correlation with $\Delta m_{15}(B)$, with ρ in the range between -0.1 and -0.3 . Figure 18 shows example sequences of pre-maximum spectra with different $pW8$ (Ca II IR) values at fixed $\Delta m_{15}(B)$. Among SNe with similar $\Delta m_{15}(B)$, the spectra show quite homogeneous characteristics, except at the location of the Ca II IR triplet. The largest $pW8$ (Ca II IR) values are found when a strong high-velocity component is present.

The strongest correlations between pW ratios and $\Delta m_{15}(B)$ are shown in Figure 19 (cf. Figures 13–19 of Hachinger et al. 2006). Most of these involve Si II features and ratios with $pW4$ (Fe II) and $pW5$ (S II W) (see also Silverman et al. 2012b). One of the ratios that correlates with $\Delta m_{15}(B)$ is [$pW6$ (Si II 5972)/ $pW7$ (Si II 6355)], which is similar to the

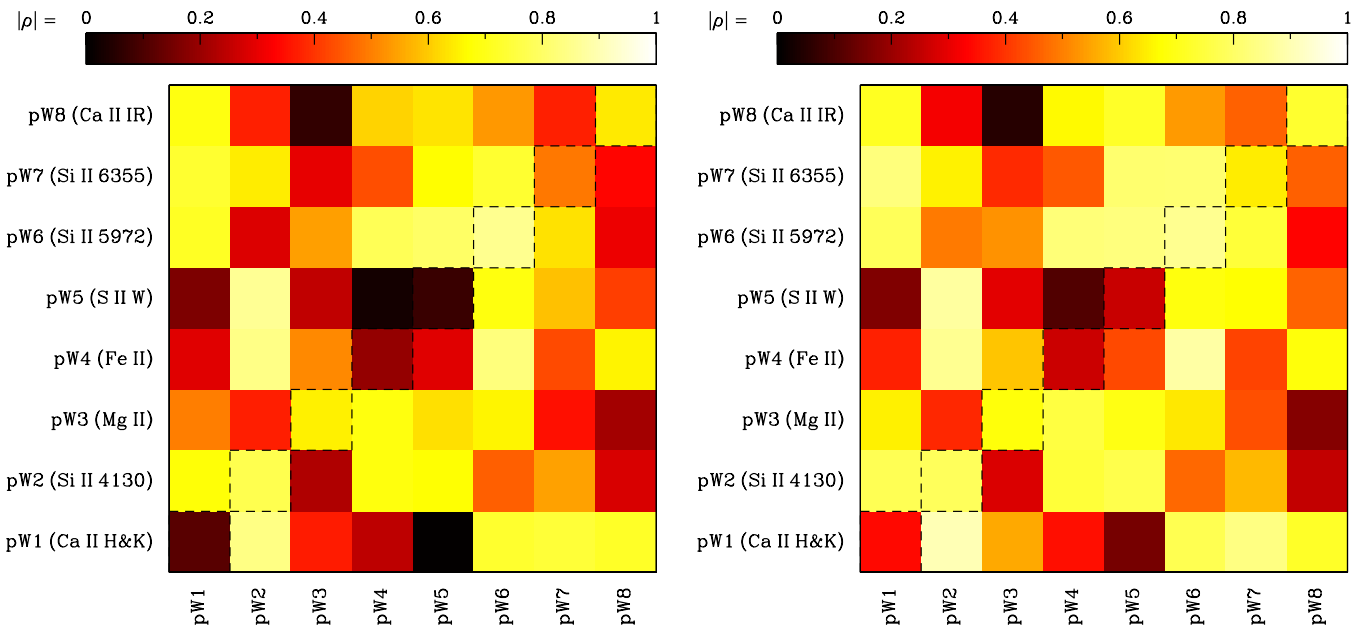


Figure 16. Correlation between pW parameters at maximum light and light-curve decline rate $\Delta m_{15}(B)$. Boxes on the diagonal show the correlation between pW and $\Delta m_{15}(B)$. Off-diagonal boxes indicate the correlation of pW ratios with $\Delta m_{15}(B)$, with the ratios computed as pW_y/pW_x . Colors indicate the absolute Pearson correlation coefficient ρ . Left panel: all SNe are included. Right panel: only objects with low expansion velocities [$v(\text{Si II } 6355) < 12,000 \text{ km s}^{-1}$] are considered. (A color version of this figure is available in the online journal.)

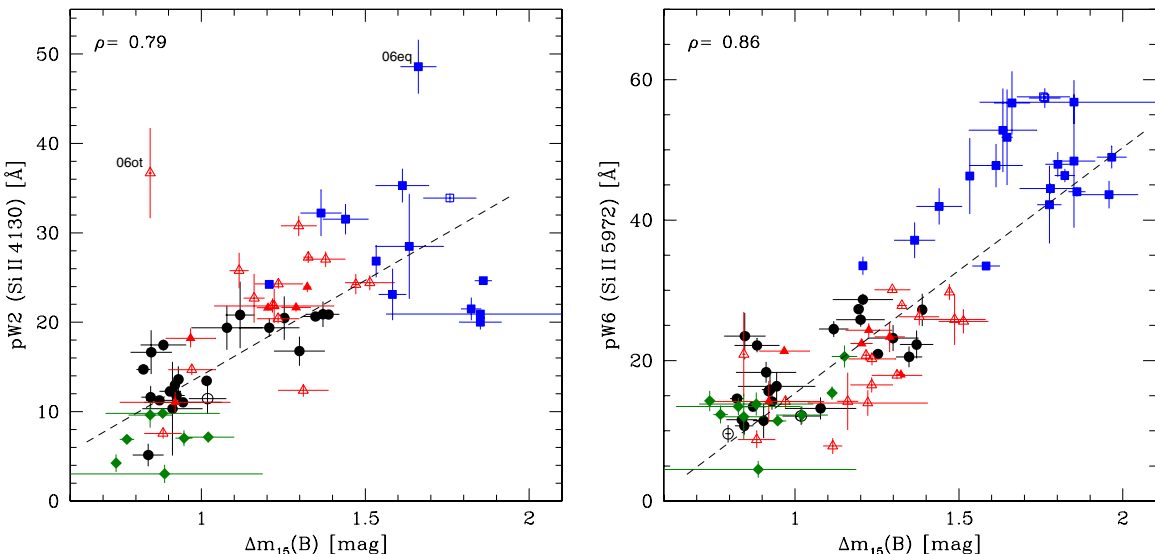


Figure 17. Pseudo-equivalent at maximum light width vs. decline rate for $pW2$ (Si II 4130) (left) and $pW6$ (Si II 5972) (right). These features show the largest correlation with $\Delta m_{15}(B)$. Symbols are the same as in Figure 6. The dashed lines indicate straight-line fits to the filled data points, i.e., SNe with low expansion velocities [$v(\text{Si II } 6355) < 12,000 \text{ km s}^{-1}$]. Pearson correlation coefficients ρ are indicated in each panel.

(A color version of this figure is available in the online journal.)

line intensity ratio introduced by Nugent et al. (1995), $\mathcal{R}(\text{Si II})$. This relationship is governed by the stronger dependence of $pW6$ (Si II 5972) than of $pW7$ (Si II 6355) on the decline rate (Hachinger et al. 2008). The dispersion is somewhat larger than that of $pW6$ (Si II 5972) versus $\Delta m_{15}(B)$, mostly due to BL SNe that have relatively large $pW7$ (Si II 6355) and fall below the rest of the sample.

We note that, although with fewer data points, $pW1$ (Ca II H&K) is involved in some of these correlations. Interestingly, as shown in the top right panel, the relative strength of $pW8$ (Ca II IR) with respect to $pW1$ (Ca II H&K) increases with $\Delta m_{15}(B)$. This is a consequence of the behavior noted above for $pW8$ (Ca II IR) and $pW1$ (Ca II H&K) versus $\Delta m_{15}(B)$.

A temperature effect related with $\Delta m_{15}(B)$ may cause the anti-correlation of $[pW1(\text{Ca II H\&K})/pW8(\text{Ca II IR})]$ with $\Delta m_{15}(B)$. The effect is presumably equivalent to the one described by Hachinger et al. (2008) to explain the behavior of $\mathcal{R}(\text{Si II})$ with $\Delta m_{15}(B)$. The most abundant ionization state of calcium in SNe Ia near maximum light is Ca III (Tanaka et al. 2008). As temperature decreases with increasing $\Delta m_{15}(B)$, the abundance of Ca II increases. If both calcium lines are not saturated, this effect should equally increase their intensities. The observed behavior with $\Delta m_{15}(B)$, however, indicates that Ca II H&K may be saturated and so it does not react to abundance changes, while the contrary happens with the Ca II IR triplet.

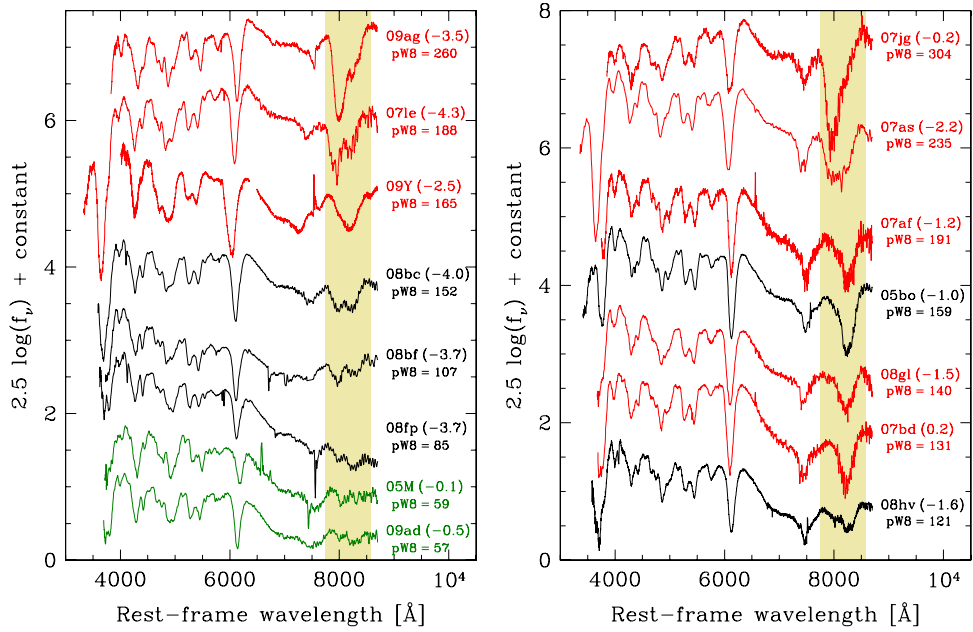


Figure 18. Spectral sequences of decreasing $pW8$ (Ca II IR) for $\Delta m_{15}(B) \approx 0.9$ mag (left) and $\Delta m_{15}(B) \approx 1.3$ mag (right). The Branch subtype of each SN is indicated by the color of the line following the same symbol scheme as symbol colors in Figure 6. The labels on the right-hand side indicate the SN name, the epoch of the spectrum between parentheses, and the value of $pW8$ (Ca II IR) in Å (derived at maximum light) for each SN. The spectra were obtained between four days before and the time of maximum light. The shaded region marks the range of expansion velocities up to about $30,000$ km s^{-1} . Large variations in the Ca II IR triplet are seen in otherwise homogeneous spectra among normal SNe Ia.

(A color version of this figure is available in the online journal.)

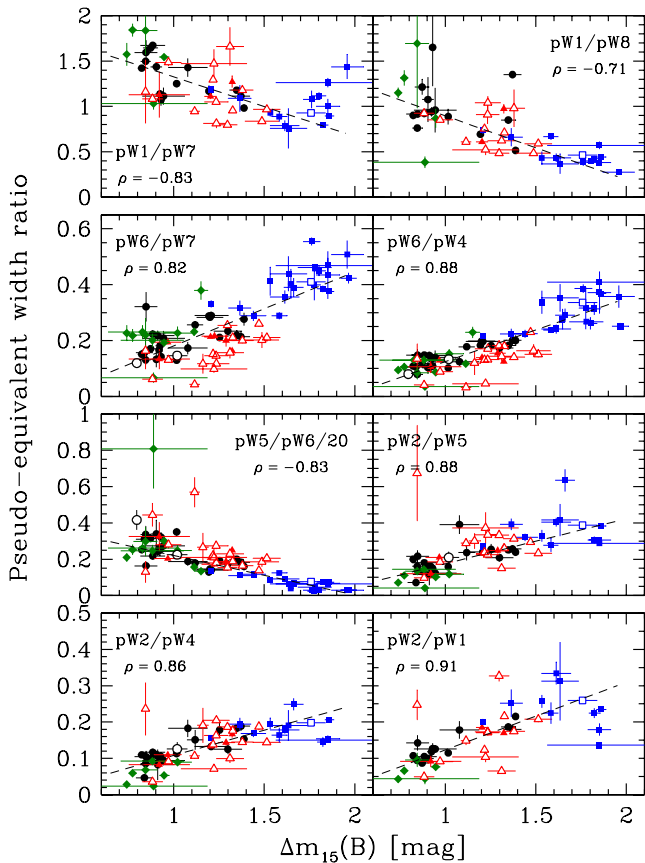


Figure 19. pW ratios that correlate with $\Delta m_{15}(B)$. Symbols are the same as in Figure 6. The dashed lines indicate straight-line fits to the data of low-velocity SNe [v (Si II 6355) < $12,000$ km s^{-1} ; filled symbols]. Pearson correlation coefficients ρ for those data points are indicated in each panel.

(A color version of this figure is available in the online journal.)

5.2. Expansion Velocity and Light-curve Decline Rate

As mentioned in Section 4, SNe Ia show a wide variety of line expansion velocities. Here we study the behavior of expansion velocities of different lines at maximum light with respect to light-curve decline rate. Figure 20 shows the degree of correlation between velocity measurements at maximum light (on the diagonal) or ratios of these (off the diagonal), and $\Delta m_{15}(B)$. We can see that none of the line velocities presented here correlate strongly with decline rate. The ratios of v (S II 5449)/ v (Si II 6355), v (S II 5622)/ v (Si II 6355), and v (S II 5449)/ v (Si II 4130) show the largest degrees of anti-correlation with $\Delta m_{15}(B)$ ($\rho < -0.80$).

The lack of dependence of line velocities on $\Delta m_{15}(B)$ is accompanied by a more or less clearly defined minimum expansion velocity for all decline rates. This velocity floor is about $10,000$ km s^{-1} for the strongest absorptions (Ca II H&K and IR triplet, and Si II $\lambda 6355$), and between 6000 and 8000 km s^{-1} for the weaker lines. In the case of v (Si II 5972), the minimum velocity appears to be about 1000 km s^{-1} higher for fast-declining SNe Ia [with $\Delta m_{15}(B) \gtrsim 1.5$ mag] than for the rest. The opposite occurs with v (S II 5449) and v (S II 5622) where SNe with $\Delta m_{15}(B) > 1.5$ mag present on average lower velocities by about 1500 km s^{-1} (cf. Hachinger et al. 2006; Blondin et al. 2006). The SS SN 2005M stands out in our sample by having the lowest expansion velocities, by up to 2000 km s^{-1} for some features (see Section 4.3).

Figure 21 shows the velocity decline rates for the Si II $\lambda 6355$ line, $\Delta v_{20}(\text{Si})$, versus $\Delta m_{15}(B)$. A similar relationship was presented in the left panel of Figure 17 of Blondin et al. (2012) by adopting the velocity decline during 10 days after maximum light. The velocity gradient \dot{v} as defined by Benetti et al. (2005) shows a larger dispersion in its relation with $\Delta m_{15}(B)$ (see their Figure 3(b)) than the one of $\Delta v_{20}(\text{Si})$ presented here. The same happens with the instantaneous velocity decline rate defined in

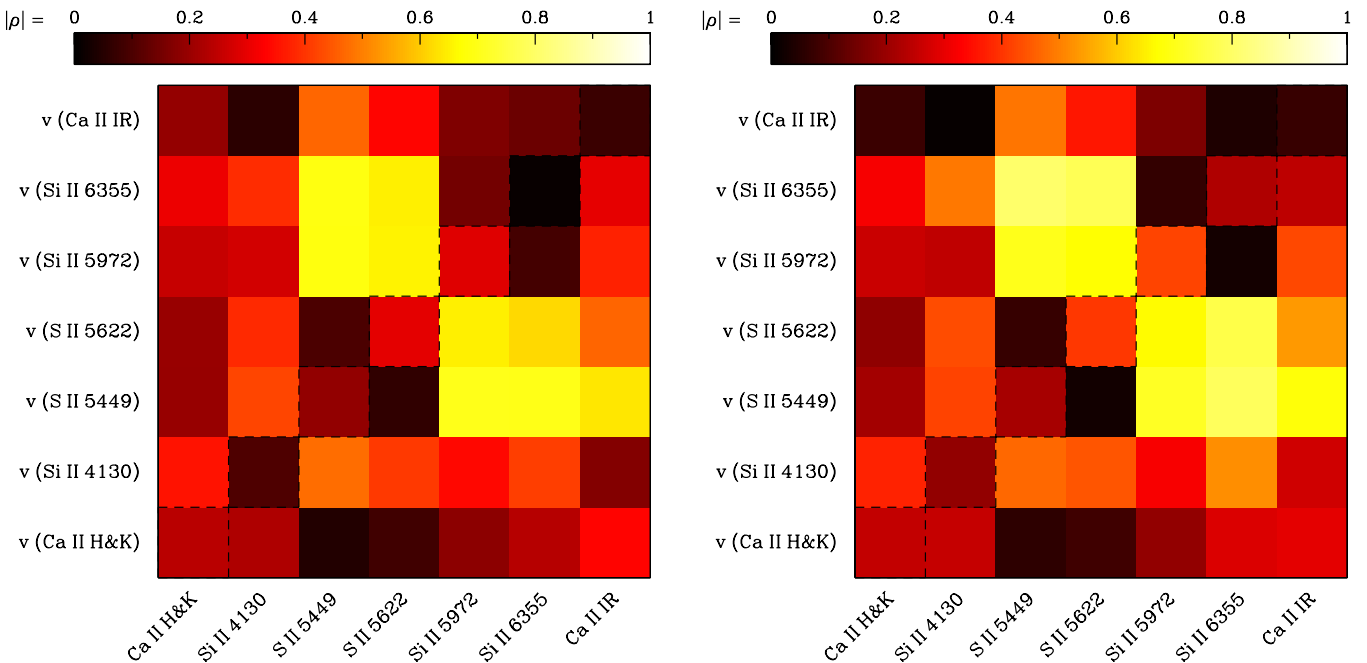


Figure 20. Correlation between expansion velocities at maximum light (on the diagonal) and their ratios (off-diagonal), and light-curve decline rate $\Delta m_{15}(B)$. Ratios for the off-diagonal boxes are computed as v_y/v_x . Colors indicate the absolute Pearson correlation coefficient ρ . Left panel: all SNe are included. Right panel: only objects with low expansion velocities [$v(\text{Si II } 6355) < 12,000 \text{ km s}^{-1}$] are considered.

(A color version of this figure is available in the online journal.)

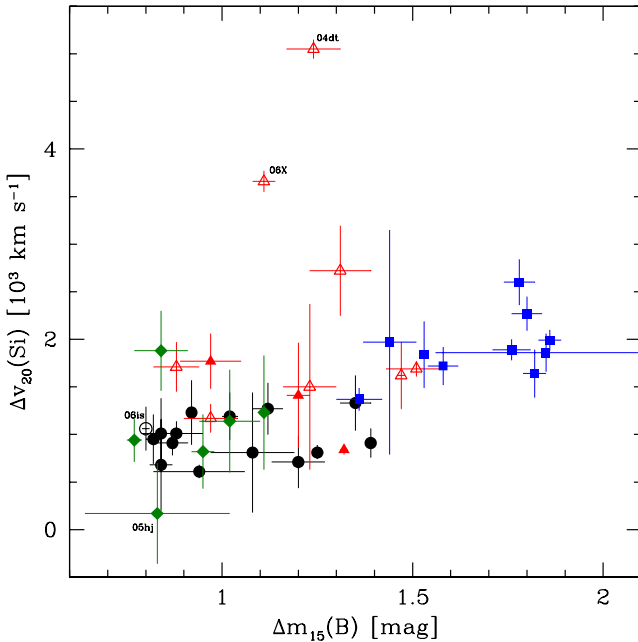


Figure 21. $\text{Si II } \lambda 6355$ velocity decline rates as a function of $\Delta m_{15}(B)$. Symbol coding is the same as in Figure 6.

(A color version of this figure is available in the online journal.)

the right panel of Figure 17 of Blondin et al. (2012). In the case of $\Delta v_{20}(\text{Si})$, there seems to be a continuous link between CN, SS, and CL SNe Ia. Excluding BL SNe, which show the largest $\Delta v_{20}(\text{Si})$ values, a correlation coefficient as large as $\rho = 0.86$ is found between $\Delta v_{20}(\text{Si})$ and $\Delta m_{15}(B)$.

5.3. Luminosity Calibration

SN-Ia peak absolute magnitudes can be calibrated against decline rate and color (Tripp 1998) with a precision between

0.1 and 0.2 mag (Hicken et al. 2009; Folatelli et al. 2010). Given the correlation of $pW2$ ($\text{Si II } 4130$) and $pW6$ ($\text{Si II } 5972$) with $\Delta m_{15}(B)$ shown in Figure 17 (Section 5.1), we tested the calibration of B -band peak absolute magnitudes versus $(B_{\max} - V_{\max})$ pseudo-color and these pW parameters (similar analysis can be found in Blondin et al. 2011b; Silverman et al. 2012b). For this purpose, we replaced $\Delta m_{15}(B)$ by $pW2$ ($\text{Si II } 4130$) and $pW6$ ($\text{Si II } 5972$) in Equation (6) of Folatelli et al. (2010) for the B band. We obtained

$$\mu = B_{\max} - M_B(0) - a_B(pW - pW_0) - \beta_B^{BV} (B_{\max} - V_{\max}), \quad (3)$$

where pW corresponds to $pW2$ ($\text{Si II } 4130$) and $pW6$ ($\text{Si II } 5972$), and $pW_0 = 15 \text{ \AA}$ and 20 \AA , respectively. The redshift-based distances used for Equation (2) were supplemented with distance to the host galaxies of SNe 2005ke, 2006X, and 2006mr available in the literature. These objects were excluded from Equation (2) because they either had too large $E(B - V)_{\text{Host}}$ or $\Delta m_{15}(B)$, but they can be included in the luminosity calibration. For SNe 2005ke and 2006X, we adopted $\mu = 31.84 \pm 0.08$ mag and $\mu = 30.91 \pm 0.14$ mag, respectively, as given in Table 7 of Folatelli et al. (2010). For SN 2006mr, we used the latest distance modulus to its host, NGC 1316, of $\mu = 31.25 \pm 0.05$ mag provided by Stritzinger et al. (2010).

We fitted for $M_B(0)$, a_B , and β_B^{BV} employing the same χ^2 minimization method as described in the Appendix A of Folatelli et al. (2010). Table 9 provides the results of the fits for different subsamples of SNe Ia. The table lists the fitted parameters, the estimated intrinsic dispersion σ_{SN} (see Appendix A of Folatelli et al. 2010), the number of SNe used, and the sample selected for each fit. The weighted rms about the fit is also listed, defined as

$$\text{WRMS} = \frac{\sum_i^{N_{\text{SN}}} [\mu_i - \bar{\mu}_i]^2 / (\sigma_i^2 + \sigma_{\text{SN}}^2)}{\sum_i^{N_{\text{SN}}} 1 / (\sigma_i^2 + \sigma_{\text{SN}}^2)}, \quad (4)$$

Table 9
Fits of Peak Magnitudes versus pW and $(B - V)$ Pseudo-color

Fit No. (1)	$M_B(0)$ (2)	a_B (3)	β_B^{BV} (4)	R_V (CCM+O) (5)	σ_{SN} (mag) (6)	WRMS (mag) (7)	N_{SNe} (8)	Sample (9)
$pW2$ (Si II 4130) [$pW_0 = 15 \text{ \AA}$]								
1	-19.07 ± 0.05	0.0135 ± 0.0028	3.18 ± 0.14	1.85 ± 0.13	0.10	0.17	55	Complete
2	-19.07 ± 0.05	0.0149 ± 0.0030	3.33 ± 0.26	1.98 ± 0.24	0.09	0.17	40	Non-HV
3	-19.09 ± 0.17	0.0137 ± 0.0118	3.36 ± 0.33	2.01 ± 0.30	0.00	0.13	20	CN
4	-19.07 ± 0.07	0.0154 ± 0.0035	3.30 ± 0.40	1.96 ± 0.36	0.08	0.16	42	$(B - V) < 0.2$
5	-19.07 ± 0.05	0.0148 ± 0.0029	3.24 ± 0.27	1.90 ± 0.24	0.09	0.16	37	$\Delta m_{15}(B) < 1.7$
$pW6$ (Si II 5972) [$pW_0 = 20 \text{ \AA}$]								
6	-19.08 ± 0.04	0.0112 ± 0.0018	3.19 ± 0.12	1.86 ± 0.11	0.12	0.19	67	Complete
7	-19.09 ± 0.04	0.0108 ± 0.0021	3.18 ± 0.17	1.84 ± 0.15	0.09	0.17	49	Non-HV
8	-19.05 ± 0.15	0.0141 ± 0.0091	3.42 ± 0.42	2.07 ± 0.39	0.12	0.18	22	CN
9	-18.99 ± 0.06	0.0173 ± 0.0027	3.00 ± 0.37	1.69 ± 0.33	0.08	0.16	48	$(B - V) < 0.2$
10	-19.04 ± 0.04	0.0137 ± 0.0021	2.94 ± 0.25	1.64 ± 0.22	0.05	0.14	41	$\Delta m_{15}(B) < 1.7$

Notes. Fits of the type: $\mu = B_{\max} - M_B(0) - a_B [pW - pW_0] - \beta_B^{BV} (B - V)$. Column 1: fit identifier; Column 2: peak absolute magnitude for $pW = pW_0$ and zero $(B - V)$ pseudo-color; Column 3: luminosity- pW slope; Column 4: luminosity-color slope; Column 5: corresponding parameter R_V of the CCM+O reddening law; Column 6: resulting intrinsic dispersion of SN data; Column 7: weighted rms of fit in magnitudes (see the text); Column 8: number of SNe used in fit; Column 9: sample of SNe used in fit (see the text).

where $\bar{\mu}_i$ is the distance modulus as derived from the best fit of Equation (3), σ_i is the measurement uncertainty in the distance modulus (see Appendix A of Folatelli et al. 2010), and i runs along the sample of N_{SN} SNe.

The weighted rms scatter for the complete sample are 0.17 mag and 0.19 mag (fits 1 and 6 for $pW2$ (Si II 4130) and $pW6$ (Si II 5972), respectively). Similar results for $pW2$ (Si II 4130) were found by Blondin et al. (2011b) and Silverman et al. (2012b). The fit and scatter remain nearly unchanged when HV SNe are removed (fits 2 and 7). When we consider only CN SNe Ia, the scatter is reduced to 0.13 mag for the case of $pW2$ (Si II 4130) (fit 3). If we cut the sample of SNe Ia to exclude objects redder than $(B_{\max} - V_{\max}) = 0.2$ mag—which excludes reddened objects but also most CL SNe—the scatter is reduced to 0.16 mag (fits 4 and 9).

For comparison, the fits with exactly the same samples of SNe as in Table 9, but now with $\Delta m_{15}(B)$ instead of pW , yield very similar values of WRMS. For the complete sample and $(B_{\max} - V_{\max}) < 0.2$ mag cuts, the resulting WRMS values are 0.20 mag and 0.18 mag, respectively (see also Table 8 of Folatelli et al. 2010).

The intrinsic dispersions σ_{SN} of the luminosity- pW fits are $\lesssim 0.1$ mag in all cases. Assuming the measurement uncertainties are well constrained, this indicates that the actual dispersion not accounted for in the fits is not large. The slopes, a_B , of the relation between peak absolute magnitudes and pW for all fits are compatible within uncertainties, except for a slightly larger slope when using $pW6$ (Si II 5972) and SNe with $(B_{\max} - V_{\max}) < 0.2$ mag.

The slopes, β_B^{BV} , of peak luminosity versus color are also compatible within uncertainties for all fits shown in Table 9. Such color dependence of luminosity can be interpreted as the effect of dust extinction. Nevertheless, the dependence of luminosity on color for eCL SNe—which are intrinsically red—seems to agree with that of SNe reddened by dust. This is indicated by the lack of change in β_B^{BV} when we exclude SNe with $\Delta m_{15}(B) > 1.7$ mag—that is, basically excluding the eCL group—as shown in fits 5 and 10. Assuming the CCM+O reddening law, the color slope can be converted to the total-to-selective absorption coefficient R_V . The conversion is detailed

in Appendix B of Folatelli et al. (2010). The resulting R_V values are in the range of 1.6–2.1, depending on the sample employed. This is slightly larger than the range of $1.0 < R_V < 1.5$ found by Folatelli et al. (2010) when fitting versus $\Delta m_{15}(B)$ on a subsample of the SNe Ia presented here. Still, the R_V values found here are smaller than the Galactic average of $R_V = 3.1$, with a significance of at least 3σ .

In an attempt to refine the precision of SNe Ia as distance indicators, we searched for possible correlations between spectral parameters and residuals of the luminosity calibration. B -band peak absolute magnitude residuals, ΔM_B , were calculated based on the best fit of luminosity versus $\Delta m_{15}(B)$ and $(B_{\max} - V_{\max})$ pseudo-color at maximum light as in Equation (6) of Folatelli et al. (2010),

$$\mu = B_{\max} - M_B(0) - b_B [\Delta m_{15}(B) - 1.1] - \beta_B^{BV} (B_{\max} - V_{\max}). \quad (5)$$

The fit included 82 SNe Ia with available distances and photometric parameters, and yielded $M_B(0) = -19.16 \pm 0.01$ mag, $b_B = 0.55 \pm 0.08$, and $\beta_B^{BV} = 3.05 \pm 0.10$ (cf. fit 1 of Table 8 in Folatelli et al. 2010). The peak absolute magnitude residuals were thus computed as

$$\Delta M_B = B_{\max} - \mu + 19.16 - 3.05 (B_{\max} - V_{\max}) - 0.55 [\Delta m_{15}(B) - 1.1]. \quad (6)$$

where ΔM_B values are given in the last column of Table 1.

We investigated possible correlations between ΔM_B and spectral parameters. In general agreement with Blondin et al. (2011b) and Silverman et al. (2012b), no significant dependence was found with any of the pW parameters. On the other hand, we found that the residuals depend slightly on Si II and Si III velocities, in particular when considering SNe Ia with $\Delta m_{15}(B) < 1.7$ mag. Figure 22 shows the strongest of such correlations. Table 10 summarizes the results of the fits. The slopes of ΔM_B versus v (Si II 5972), v (Si II 6355), v (Si II 5449), and v (Si II 5622) are different from zero at the $\approx 2\sigma$ – 3σ level. Given the lack of correlations found for other SN-Ia samples by Blondin et al. (2011b) and Silverman et al. (2012b), the results presented here deserve further study using large, homogeneous samples.

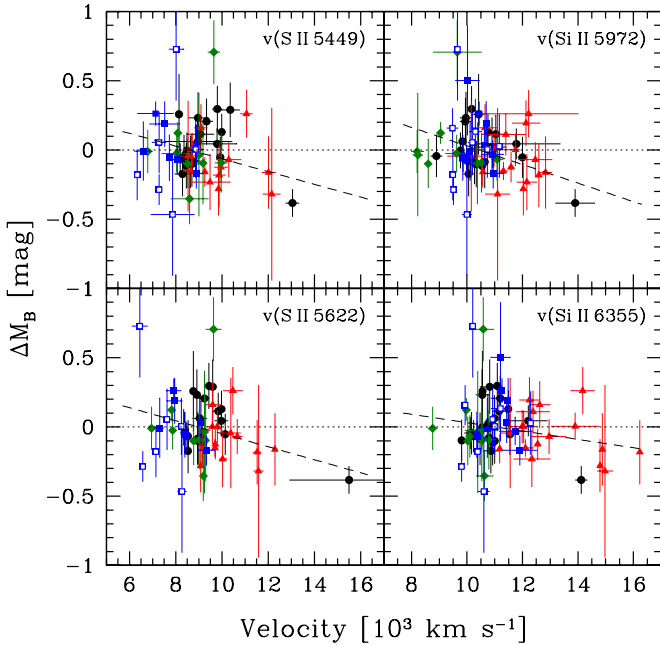


Figure 22. Peak absolute B -band magnitude residuals vs. S II and Si II expansion velocities. Different Branch subtypes are represented by black circles (CN), blue squares (CL), red triangles (BL), and green diamonds (SS). Filled symbols indicate SNe with $\Delta m_{15}(B) < 1.7$ mag while the rest of the objects are shown with open symbols. The dashed lines show straight-line fits to the filled data points.

(A color version of this figure is available in the online journal.)

Table 10
Straight-line Fits to ΔM_B versus Expansion Velocity at Maximum Light for SNe Ia with $\Delta m_{15}(B) < 1.7$ mag

Velocity Feature	a (mag)	b (mag/ 10^3 km s^{-1})	σ_{SN} (mag)	WRMS (mag)	No. of SNe
$v(\text{Ca II H&K})$	0.057(170)	-0.005(011)	0.106	0.178	35
$v(\text{Si II 4130})$	0.041(206)	-0.004(020)	0.052	0.147	53
$v(\text{S II 5449})$	0.396(189)	-0.046(021)	0.083	0.167	49
$v(\text{S II 5622})$	0.421(161)	-0.047(017)	0.067	0.157	49
$v(\text{Si II 5972})$	0.699(211)	-0.067(020)	0.046	0.150	55
$v(\text{Si II 6355})$	0.333(202)	-0.030(017)	0.074	0.161	58
$v(\text{Ca II IR})$	-0.048(162)	-0.000(012)	0.094	0.162	27

Note. Fits of the type: $\Delta M_B = a + b \times v$, with v expressed in 10^3 km s^{-1} .

A Kolmogorov–Smirnov (K-S) test on the distribution of Hubble residuals for SNe Ia separated into the HV and normal classes of Wang et al. (2009) gives a p -value of 0.07 (for 17 HV and 31 normal SNe). There is a non-negligible probability that both distributions are consistent. However, the difference in average Hubble residuals is noticeable between HV and normal SNe Ia (or between BL and the complete sample), as shown in the last column of Table 8. In case the differences are confirmed, they may be related to the finding that the scatter in the Hubble diagram is reduced when using only normal SNe Ia, as shown by Foley & Kasen (2011). Part of the difference in Hubble residuals may be explained by differences in intrinsic colors between normal and HV SNe. If, as suggested by Foley & Kasen (2011), HV objects show redder intrinsic colors than normal SNe Ia, then they could be “overcorrected” by reddening. However, when we compared the distributions of $(B_{\max} - V_{\max})$ for both subclasses using a K-S test, the resulting p -value was of 0.85, indicating that both color distributions are consistent (cf. Foley et al. 2011).

Table 11
Straight-line Fits to $(B_{\max} - V_{\max})_0$ versus pW for SNe Ia with $\Delta m_{15}(B) < 1.7$ mag

pW Feature	pW_0 (\AA)	a (mag)	b (mag \AA^{-1})	σ_{SN} (mag)	WRMS (mag)	No. of SNe
$pW1(\text{Ca II H&K})$	120	0.008(083)	0.0000(0007)	0.044	0.049	16
$pW2(\text{Si II 4130})$	15	0.002(033)	0.0034(0016)	0.033	0.039	20
$pW3(\text{Mg II})$	120	0.034(036)	0.0010(0003)	0.032	0.041	21
$pW4(\text{Fe II})$	130	0.012(078)	0.0012(0006)	0.037	0.044	22
$pW5(\text{S II W})$	90	0.018(124)	-0.0009(0014)	0.043	0.050	22
$pW6(\text{Si II 5972})$	20	0.013(030)	0.0035(0013)	0.033	0.041	22
$pW7(\text{Si II 6355})$	100	0.023(069)	0.0012(0007)	0.038	0.046	22
$pW8(\text{Ca II IR})$	140	0.020(030)	0.0006(0002)	0.033	0.040	20

Note. Fits of the type: $(B_{\max} - V_{\max})_0 = a + b \times [pW - pW_0]$.

5.4. Color

SN colors play a key role in the determination of extinction and in the calibration of luminosity. Investigating the relation between colors and spectroscopic parameters may serve to distinguish reddening sources of intrinsic and extrinsic nature, and to understand the origin of color variations. Here we study the relationship between $(B_{\max} - V_{\max})$ and pW for different spectral features. In order to search for possible dependence of intrinsic colors $(B_{\max} - V_{\max})_0$ on pW , a subset of “low-reddening” SNe was identified. This was done following two requirements: (1) objects with E/S0 host galaxies or isolated from nuclei and arms, and (2) no evidence of Na I D lines from the host galaxy in the spectra. To this sample, we added some objects whose late-time $(B - V)$ colors were compatible with the intrinsic-color law given in Equation (2) of Folatelli et al. (2010). These SNe are indicated with a “Y” in Column 8 of Table 1.

It has been shown that intrinsic $B - V$ colors of SNe Ia at maximum light depend on decline rate (Phillips et al. 1999; Altavilla et al. 2004; Folatelli et al. 2010). The dependence is slight for SNe with $\Delta m_{15}(B) < 1.7$ mag. For the fastest declining objects, however, colors are significantly redder than for the rest of SNe Ia. We thus performed straight-line fits to the intrinsic color– pW relations using low-reddening SNe with $\Delta m_{15}(B) < 1.7$ mag. This excludes the eCL SNe Ia, most of which are in the low-reddening group,²⁴ with the exception of SN 2006bd, which has $\Delta m_{15}(B) = 1.65 \pm 0.02$ mag and is also significantly bluer than the rest of the eCL objects. Note that eCL SNe have no measurements of $pW2(\text{Si II 4130})$. Table 11 summarizes the fit results for all eight pW parameters. Most features show a positive dependence of intrinsic color on pW , except $pW5(\text{S II W})$. Figure 23 shows the relations for that feature along with those that yielded the strongest dependence. The slopes in these cases are different from zero at the 2σ – 3σ level. Nordin et al. (2011b) showed a similar trend in the case of the $\text{Si II } \lambda 4130$ line. Based on a large sample of SNe Ia with measurements of extinction-corrected pseudo-colors at maximum light, Foley et al. (2011) found a correlation between $(B_{\max} - V_{\max})_0$ and $pW7(\text{Si II 6355})$. In our case, we obtain a similar relation, but the fit slope is just 1.7σ from zero. It should be noted that Foley et al. (2011) obtain their intrinsic colors in a different way than the one adopted here. They define

²⁴ The two eCL objects outside the low-reddening sample are SNe 2005bl and 2006mr. While the former may have suffered significant reddening of $E(B - V)_{\text{host}} = 0.17$ mag (Taubenberger et al. 2008), SN 2006mr can be considered to be nearly reddening free (Stritzinger et al. 2010).

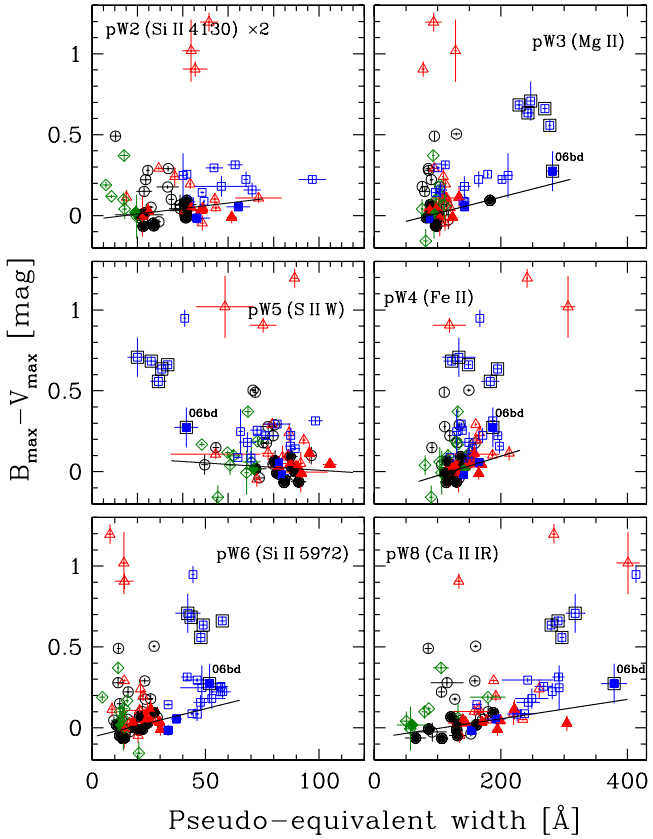


Figure 23. Pseudo-colors at maximum light, $(B_{\max} - V_{\max})$, corrected by the Milky Way reddening, as a function of pW for several spectral features. Filled symbols correspond to SNe with low host-galaxy reddening (see the text) and $\Delta m_{15}(B) < 1.7$ mag. The solid lines show straight-line fits to such data points, as summarized in Table 11. Members of the eCL group are indicated with a black square. They present intrinsically red colors but most of them are excluded from the fits because they have $\Delta m_{15}(B) > 1.7$ mag.

(A color version of this figure is available in the online journal.)

$(B_{\max} - V_{\max})_0$ as the residuals in the color axis of the relation between light-curve shape corrected absolute magnitudes and color. This implies the underlying hypothesis that the relation between peak luminosity and light-curve shape holds exactly for all SNe. In our case, we do not resort to such an assumption but define a low-reddening sample, independently of the luminosity calibration. This procedure has the price of reducing the working sample of SNe. We confirm the lack of dependence of intrinsic color on $pW1$ (Ca II H&K) also shown by Foley et al. (2011).

An interesting case is that of $pW5$ (S II W), which shows a negative slope, although with a low significance. It should be noted, however, that eCL SNe Ia seem to follow the trend found for the rest of the low-reddening sample, with redder colors and lower $pW5$ (S II W), although deviating from the straight-line fit. Something of the same sort can be seen in the case of $pW3$ (Mg II), with eCL SNe showing the largest colors and pseudo-equivalent widths. This is expected since the increase in $pW3$ (Mg II) by the presence of strong Ti II absorption affects the B -band magnitude and is related with a temperature effect. The explanation is not so straightforward for $pW5$ (S II W).

We have also searched for correlations between $(B_{\max} - V_{\max})_0$ and expansion velocities at maximum light based on the same sample of low-reddening SNe. Contrary to what Foley et al. (2011) presented, we find no significant relation for any of the line velocities analyzed here. In order to directly compare with the latter work, we restrict the sample to SNe with

$1.0 \text{ mag} \leq \Delta m_{15}(B) \leq 1.5 \text{ mag}$. For v (Si II 6355) we find a slope of $0.012 \pm 0.016 \text{ mag}/10^3 \text{ km s}^{-1}$, which is lower and less significant than the value of $0.033 \pm 0.004 \text{ mag}/10^3 \text{ km s}^{-1}$ given by Foley et al. (2011). Part of the discrepancy may be due to the different definition of $(B_{\max} - V_{\max})_0$, as was pointed out above. Blondin et al. (2012) find milder relations than Foley et al. (2011), although still with 2σ – 3σ significance (see their Table 6). Our results seem to be in contradiction with the predictions of asymmetric models by Kasen & Plewa (2007) as presented in Figure 8 of Foley & Kasen (2011). Other two-dimensional models by Kasen et al. (2009) agree more with the vanishing slopes of color versus v (Si II 6355), as shown in Figure 18 of Blondin et al. (2011a), although for those models the expansion velocities are all larger than $11,000 \text{ km s}^{-1}$.

6. DISCUSSION AND CONCLUSIONS

In this paper, we have presented optical spectroscopic data of 93 low-redshift SNe Ia observed by the CSP between 2004 and 2009. The data set amounts to 604 previously unpublished spectra obtained on 502 different epochs in the range between -12 and $+155$ days with respect to B -band maximum light. To this we have added 228 published spectra of some of the SNe, obtained from the SUSPECT database and from the CfA sample (Blondin et al. 2012) and the BSNIP sample (Silverman et al. 2012a). Based on spectroscopic parameters such as line velocities and pseudo-equivalent widths we have provided a quantified classification of SN-Ia subtypes following the scheme of Branch et al. (2006). We note, however, that the separation between subclasses is somewhat arbitrary because there is no clear discontinuity in the spectroscopic properties of SNe Ia when we go from one group to another. With a study of spectroscopic parameters at maximum light and their relationship with photometric quantities we have attempted to understand the properties of SNe Ia and their calibration as distance indicators.

Among the Branch subtypes, CN SNe Ia present the largest degree of homogeneity in their optical spectrum at maximum light, as was also found by Blondin et al. (2012) for the CfA sample. For all subtypes, the dispersion increases toward both ends of the optical range. At the blue end, the dispersion among SS and BL objects seems to be dominated by dust reddening. For CL SNe, the dispersion is mostly due to temperature differences in the ejecta, which produces variations in the absorption features due to Ti II between $\approx 4000 \text{ \AA}$ and $\approx 4500 \text{ \AA}$. At the extreme of this class (eCL) we find SN 1991bg-like objects with large $pW3$ (Mg II), intrinsically red color at maximum light, and fast light-curve decline rate. These properties allow us to distinguish eCL SNe from the rest of the CL subclass which as a whole shows no discontinuity in spectral properties from CN SNe. The greater degree of association of SS SNe with star-forming regions as compared with the other subtypes becomes evident through the appearance of host-galaxy lines in the composite spectrum of Figure 7.

At the red of the spectrum, other interesting deviations appear related with the strength of the Ca II IR triplet and O I $\lambda 7774$. The shape of the former feature reveals high-velocity components present in most CN, BL, and SS objects. CL SNe show large Ca II IR absorptions with no evidence of high-velocity components. The strength of this absorption as measured by $pW8$ (Ca II IR) tends to increase with $\Delta m_{15}(B)$, which implies that it increases in the sequence of SS–CN–BL–CL subtypes. At a given $\Delta m_{15}(B)$, however, the dispersion of $pW8$ (Ca II IR) can be large, driven mostly by dominant high-velocity features.

Interestingly, as $pW8$ (Ca II IR) grows along the sequence described above, the other Ca II feature, $pW1$ (Ca II H\&K), does not follow the same behavior but rather stays nearly constant. We speculate that the difference in behavior between both Ca II lines may be due to temperature changes affecting more the Ca II IR triplet than the Ca II H\&K line. In analogy to the mechanism invoked by Hachinger et al. (2008) to explain the dependence of the silicon ratio, $\mathcal{R}(\text{Si II})$, on $\Delta m_{15}(B)$ the Ca II H\&K is likely saturated and thus, as opposed to the Ca II IR triplet, does not grow with an increasing Ca II/Ca III abundance ratio as temperature decreases. The study of high-velocity features and their incidence among SNe Ia deserves further scrutiny. We emphasize that such study requires spectra covering a long wavelength range with high S/N around the Ca II features.

In close agreement with Blondin et al. (2012), we find that 24% of the SNe Ia belong to the HV class—defined as having $v(\text{Si II } \lambda 6355) > 12,000 \text{ km s}^{-1}$. When considering only “normal” SNe Ia—i.e., excluding 1991T- and 1991bg-like objects—the fraction of HV SNe in our sample is 31%. This percentage is close to that of 35% found in the sample of Wang et al. (2009), and the difference is further reduced if we adopt their dividing velocity of $11,800 \text{ km s}^{-1}$. We note that a study of the population of HV SNe in a homogeneous sample, preferably from a “blind” search, is required for determining the actual fraction of these objects. The implications may be important to our knowledge of the explosion physics considering the picture presented by Maeda et al. (2010a), where the differences in expansion velocities at maximum light are explained as a viewing-angle effect of an asymmetric explosion. The fraction of HV SNe would thus determine the average solid angle subtended by the fast-expanding portion of the exploding WD.

As shown by Wang et al. (2009) and Blondin et al. (2012), $v(\text{Si II } \lambda 6355)$ does not correlate strongly with the pseudo-equivalent width of the same line, unless the HV SNe are considered. Indeed, the Pearson correlation coefficient grows from $\rho = 0.50$ for non-HV SNe to $\rho = 0.86$ for HV objects. Most of the HV objects belong to the BL subtype for which the increase in $\text{Si II } \lambda 6355$ and $\text{Si II } \lambda 5972$ velocity is accompanied by an increase in $pW7$ ($\text{Si II } \lambda 6355$) (the correlation coefficients are $\rho = 0.95$ and $\rho = 0.80$ with each velocity, respectively). This behavior is the *opposite* for $pW6$ ($\text{Si II } \lambda 5972$). The strength of this line tends to *decrease* with increasing $v(\text{Si II } \lambda 6355)$ for HV or BL SNe (the correlation coefficient being $\rho = -0.60$). Based on simple SYNOW spectral models, Branch et al. (2009) explained this difference in behavior for the $\text{Si II } \lambda 5972$ and $\lambda 6355$ lines in terms of a difference in the distribution of Si II inside the ejecta. A shallower distribution for BL SNe as compared with normal SNe can produce large $\text{Si II } \lambda 6355$ absorptions while keeping the $\text{Si II } \lambda 5972$ line shallow. However, as the authors point out, several other ions may affect the spectrum at the wavelength range of these features, which may complicate the picture.

The behavior of BL SNe also stands out in the relation between velocity decline, $\Delta v_{20}(\text{Si})$, and light-curve decline rate, $\Delta m_{15}(B)$. By excluding the BL objects, a correlation between both quantities can be recovered with $\rho = 0.79$ (cf. Blondin et al. 2012). As already pointed out by Benetti et al. (2005), this indicates that SNe with fast-declining light curves (their FAINT subtype) also decline faster in the Si II post-maximum velocity evolution, as compared with the CN and SS objects (i.e., most of the LVG class of Benetti et al.). It is worth noting that BL SNe show, on average, larger negative residuals in the absolute peak magnitude calibration versus decline rate and color, as compared

with other subtypes (see Table 8). This drives the dependence found between residuals, ΔM_B , and velocities from S II and Si II (Figure 22).

We have detected two cases that indicate even further diversity in the distribution of elements within the ejecta of SNe Ia. These are SS SN 2005M and CN (but HV) SN 2006is (see Section 4.3). They show extreme Si II velocities at the low end of SS objects (SN 2005M), and at the high end of CN objects (SN 2006is), accompanied by other light species such as O I and S II . However, both objects show normal expansion velocities of $\approx 11,000 \text{ km s}^{-1}$ for the rest of the ions. SN 2006is resembles the case of SN 2009ig that showed a strong, high-velocity component of the $\text{Si II } \lambda 6355$ line before maximum light (Foley et al. 2012).

It is worth investigating whether models with departures from spherical symmetry (e.g., Maeda et al. 2010b) that have been suggested to explain the differences in velocity decline rates (Maeda et al. 2010a) can also provide an explanation to (1) the lack of growth of the $\text{Si II } \lambda 5972$ feature among BL SNe, (2) the relatively higher luminosity (negative residuals) of this subtype after calibration by $\Delta m_{15}(B)$ and color, and (3) the peculiar Si II velocities of cases like SNe 2005M and 2006is. In addition to improving our knowledge of the physical properties of SNe Ia, such studies may help to increase the precision of distance estimations.

Given the correlation of $pW2$ ($\text{Si II } \lambda 4130$) and $pW6$ ($\text{Si II } \lambda 5972$) with light-curve decline rate, we have replaced $\Delta m_{15}(B)$ by these pW parameters in the calibration of peak luminosities for SNe Ia. The resulting fits of peak absolute magnitudes versus pW and color show similar precision as those based on $\Delta m_{15}(B)$. The rms scatter in the calibrated B -band peak absolute magnitude is as low as 0.13 mag, with less than ≈ 0.1 mag of estimated intrinsic scatter. Such dispersion is also similar to the ones found by Bailey et al. (2009) and Blondin et al. (2011b) based on spectral flux ratios. These results suggest that SNe Ia can be calibrated as distance indicators to within 6%–8% with just a measurement of the color and a spectrum at maximum light. Moreover, the required S/N of the spectrum need not be very high since pW measurements integrate over a range of $\gtrsim 100 \text{ \AA}$. The use of $pW2$ ($\text{Si II } \lambda 4130$) in particular has the advantage of being applicable to optical observations up to a redshift of $z \approx 1$.

The fits described above additionally provide information about the nature of extinction in the host galaxies, if the color dependence is interpreted as the effect of reddening by dust. From the slopes of the color dependence we have derived low values of the total-to-selective absorption coefficient of $R_V \approx 2$, although not as low as those found when $\Delta m_{15}(B)$ is used instead of pW (Folatelli et al. 2010). This result holds both when including or excluding intrinsically red SNe (those in the CL group), indicating that the effect of dust reddening on luminosity is similar to that of intrinsic reddening among CL SNe.

This research is supported by the World Premier International Research Center Initiative (WPI Initiative), MEXT, Japan. G.F. acknowledges financial support by Grant-in-Aid for Scientific Research for Young Scientists (23740175). This material is based upon work supported by NSF under grants AST-0306969, AST-0908886, AST-0607438, and AST-1008343. F.F., J.A., and G.P. acknowledge support from FONDECYT through grants 3110042, 3110142, and 11090421.

J.A., F.F., M.H., and G.P. acknowledge support provided by the Millennium Center for Supernova Science through grant P10-064-F (funded by “Programa Bicentenario de Ciencia y Tecnología de CONICYT” and “Programa Iniciativa Científica Milenio de MIDEPLAN”). M.S. acknowledges the generous support provided by the Danish Agency for Science and Technology and Innovation through a Sapere Aude Level 2 grant.

REFERENCES

- Allington-Smith, J., Breare, M., Ellis, R., et al. 1994, *PASP*, **106**, 983
 Altavilla, G., Fiorentino, G., Marconi, M., et al. 2004, *MNRAS*, **349**, 1344
 Altavilla, G., Stehle, M., Ruiz-Lapuente, P., et al. 2007, *A&A*, **475**, 585
 Amanullah, R., Lidman, C., Rubin, D., et al. 2010, *ApJ*, **716**, 712
 Arsenijevic, V., Fabbro, S., Mourão, A. M., & Rica da Silva, A. J. 2008, *A&A*, **492**, 535
 Bailey, S., Aldering, G., Antilogus, P., et al. 2009, *A&A*, **500**, L17
 Benetti, S., Cappellaro, E., Mazzali, P. A., et al. 2005, *ApJ*, **623**, 1011
 Blondin, S., Dessart, L., Leibundgut, B., et al. 2006, *AJ*, **131**, 1648
 Blondin, S., Kasen, D., Röpke, F. K., Kirshner, R. P., & Mandel, K. S. 2011a, *MNRAS*, **417**, 1280
 Blondin, S., Mandel, K. S., & Kirshner, R. P. 2011b, *A&A*, **526**, 81
 Blondin, S., Matheson, T., Kirshner, R. P., et al. 2012, *AJ*, **143**, 126
 Blondin, S., & Tonry, J. L. 2007, *ApJ*, **666**, 1024
 Bongard, S., Baron, E., Smadja, G., Branch, D., & Hauschildt, P. H. 2006, *ApJ*, **647**, 513
 Branch, D. 1987, *ApJ*, **316**, 81
 Branch, D., Baron, E., Thomas, R. C., et al. 2004, *PASP*, **116**, 903
 Branch, D., Dang, L. C., & Baron, E. 2009, *PASP*, **121**, 238
 Branch, D., Dang, L. C., Hall, N., et al. 2006, *PASP*, **118**, 560
 Brandt, T. D., Tojeiro, R., Aubourg, É., et al. 2011, *AJ*, **140**, 804
 Brorion, T. J., Hook, I. M., Astier, P., et al. 2008, *A&A*, **477**, 717
 Burns, C. R., Stritzinger, M., Phillips, M. M., et al. 2011, *AJ*, **141**, 19
 Buzzoni, B., Delabre, B., Dekker, H., et al. 1984, *ESO Messenger*, **38**, 9
 Cardelli, J. A., Clayton, G. C., & Mathis, J. S. 1989, *ApJ*, **345**, 245
 Contreras, C., Hamuy, M., Phillips, M. M., et al. 2010, *AJ*, **139**, 519
 Dekker, H., Delabre, B., & D’Odorico, S. 1986, *Proc. SPIE*, **627**, 339
 Dressler, A., Bigelow, B., Hare, T., et al. 2011, *PASP*, **123**, 288
 Filippenko, A. V., Richmond, M. W., Branch, D., et al. 1992a, *AJ*, **104**, 1543
 Filippenko, A. V., Richmond, M. W., Matheson, T., et al. 1992b, *ApJ*, **384**, 15
 Fisher, A. K. 2000, PhD thesis, The Univ. Oklahoma
 Folatelli, G. 2004, *NewAR*, **48**, 623
 Folatelli, G., Phillips, M. M., Burns, C. R., et al. 2010, *AJ*, **139**, 120
 Folatelli, G., Phillips, M. M., Morrell, N., et al. 2012, *ApJ*, **745**, 74
 Foley, R. J., Challis, P. J., Filippenko, A. V., et al. 2012, *ApJ*, **744**, 38
 Foley, R. J., & Kasen, D. 2011, *ApJ*, **729**, 55
 Foley, R. J., Sanders, N. E., & Kirshner, R. P. 2011, *ApJ*, **742**, 89
 Freedman, W. L., Burns, C. R., Phillips, M. M., et al. 2009, *ApJ*, **704**, 1036
 Frieman, J. A., Bassett, B., Becker, A., et al. 2008, *AJ*, **135**, 338
 Gallagher, J. S., Garnavich, P. M., Caldwell, N., et al. 2008, *ApJ*, **685**, 752
 Garavini, G., Folatelli, G., Nobili, S., et al. 2007, *A&A*, **470**, 411
 Hachinger, S., Mazzali, P. A., & Benetti, S. 2006, *MNRAS*, **370**, 299
 Hachinger, S., Mazzali, P. A., Tanaka, M., Hillebrandt, W., & Benetti, S. 2008, *MNRAS*, **389**, 1087
 Hamuy, M., Folatelli, G., Morrell, N. I., et al. 2006, *PASP*, **118**, 2
 Hamuy, M., Phillips, M. M., Suntzeff, N. B., et al. 1996, *AJ*, **112**, 2438
 Hatano, K., Branch, D., Lentz, E. J., et al. 2000, *ApJ*, **543**, 49
 Hicken, M., Wood-Vasey, W. M., Blondin, S., et al. 2009, *ApJ*, **700**, 1097
 Höflich, P., & Khokhlov, A. M. 1996, *ApJ*, **457**, 500
 Hook, I. M., Jørgensen, I., Allington-Smith, J. R., et al. 2004, *PASP*, **116**, 425
 Howell, D. A. 2001, *ApJ*, **554**, 193
 Hsiao, E. Y., Conley, A., Howell, D. A., et al. 2007, *ApJ*, **663**, 1187
 Kasen, D., & Plewa, T. 2007, *ApJ*, **662**, 459
 Kasen, D., Röpke, F. K., & Woosley, S. E. 2009, *Natur*, **460**, 869
 Kasen, D., & Woosley, S. E. 2007, *ApJ*, **656**, 661
 Leibundgut, B., Kirshner, R. P., Phillips, M. M., et al. 1993, *AJ*, **105**, 301
 Li, W., Filippenko, A. V., Chornock, R., et al. 2003, *PASP*, **115**, 453
 Li, W., Filippenko, A. V., Trefters, R. R., et al. 2001, *ApJ*, **546**, 734
 Li, W., Leaman, J., Chornock, R., et al. 2010, *MNRAS*, **412**, 1441
 Maeda, K., Benetti, S., Stritzinger, M., et al. 2010a, *Natur*, **466**, 82
 Maeda, K., Röpke, F. K., Fink, M., et al. 2010b, *ApJ*, **712**, 624
 Mandel, K. S., Narayan, G., & Kirshner, R. P. 2011, *ApJ*, **731**, 120
 Marshall, J. L., Burles, S., Thompson, I. B., et al. 2008, *Proc. SPIE*, **7014**, 169
 Mazzali, P. A., Benetti, S., Altavilla, G., et al. 2005, *ApJ*, **623**, 37
 Nordin, J., Östman, L., Goobar, A., et al. 2011a, *A&A*, **526**, 119
 Nordin, J., Östman, L., Goobar, A., et al. 2011b, *ApJ*, **734**, 42
 Nugent, P., Phillips, M., Baron, E., Branch, D., & Hauschildt, P. 1995, *ApJ*, **455**, 147
 O’Donnell, J. E. 1994, *ApJ*, **422**, 158
 Oke, J. B., & Gunn, J. E. 1982, *PASP*, **94**, 586
 Parrent, J. T., Thomas, R. C., Fesen, R. A., et al. 2011, *ApJ*, **732**, 30
 Pastorello, A., Mazzali, P. A., Pignata, G., et al. 2007, *MNRAS*, **377**, 1531
 Perlmutter, S., Aldering, G., Goldhaber, G., et al. 1999, *ApJ*, **517**, 565
 Phillips, M. M. 1993, *ApJ*, **413**, 105
 Phillips, M. M., Li, W., Frieman, J. A., et al. 2007, *PASP*, **119**, 360
 Phillips, M. M., Lira, P., Suntzeff, N. B., et al. 1999, *AJ*, **118**, 1766
 Phillips, M. M., Phillips, A. C., Heathcote, S. R., et al. 1987, *PASP*, **99**, 592
 Phillips, M. M., Wells, L. A., Suntzeff, N. B., et al. 1992, *AJ*, **103**, 1632
 Pinto, P. A., & Eastman, R. G. 2000, *ApJ*, **530**, 757
 Quimby, R., Höflich, P., & Wheeler, J. C. 2007, *ApJ*, **666**, 1083
 Riess, A. G., Challis, P., Clocchiatti, A., et al. 1998, *AJ*, **116**, 1009
 Riess, A. G., Strolger, L.-G., Casertano, S., et al. 2007, *ApJ*, **659**, 98
 Silverman, J. M., & Filippenko, A. V. 2012, *MNRAS*, **425**, 1917
 Silverman, J. M., Foley, R. J., Filippenko, A. V., et al. 2012a, *MNRAS*, **425**, 1789
 Silverman, J. M., Ganeshalingam, M., Li, W., & Filippenko, A. V. 2012b, *MNRAS*, **425**, 1889
 Silverman, J. M., Kong, J. J., & Filippenko, A. V. 2012c, *MNRAS*, **425**, 1819
 Spergel, D. N., Bean, R., Doré, O., et al. 2007, *ApJS*, **170**, 377
 Stritzinger, M., Burns, C. R., Phillips, M. M., et al. 2010, *AJ*, **140**, 2036
 Stritzinger, M., Phillips, M. M., Boldt, L. N., et al. 2011, *AJ*, **142**, 156
 Sullivan, M., Conley, A., Howell, D. A., et al. 2010, *MNRAS*, **406**, 782
 Sullivan, M., Guy, J., Conley, A., et al. 2011, *ApJ*, **737**, 102
 Suzuki, N., Rubin, D., Lidman, C., et al. 2012, *ApJ*, **746**, 85
 Tanaka, M., Mazzali, P. A., Benetti, S., et al. 2008, *ApJ*, **677**, 448
 Taubenberger, S., Hachinger, S., Pignata, G., et al. 2008, *MNRAS*, **385**, 75
 Thomas, R. C., Aldering, G., Antilogus, P., et al. 2011a, *ApJ*, **743**, 27
 Thomas, R. C., Nugent, P. E., & Meza, J. C. 2011b, *PASP*, **123**, 237
 Tripp, R. 1998, *A&A*, **331**, 815
 Wagers, A., Wang, L., & Asztalos, S. 2010, *ApJ*, **711**, 711
 Walker, E. S., Hook, I. M., Sullivan, M., et al. 2011, *MNRAS*, **410**, 1262
 Wang, X., Filippenko, A. V., Ganeshalingam, M., et al. 2009, *ApJ*, **699**, 139
 Wang, X., Li, W., Filippenko, A. V., et al. 2008, *ApJ*, **675**, 626
 Yamanaka, M., Naito, H., Kinugasa, K., et al. 2009, *PASJ*, **61**, 713